Towards a theory of phase transitions in quantum control landscapes

Nicolò Beato, 1, * Pranay Patil, 2, † and Marin Bukov 1, ‡

¹Max Planck Institute for the Physics of Complex Systems, Nöthnitzer Str. 38, 01187 Dresden, Germany

²Theory of Quantum Matter Unit, Okinawa Institute of Science and

Technology Graduate University, Onna-son, Okinawa 904-0412, Japan

(Dated: August 22, 2024)

Control landscape phase transitions (CLPTs) occur as abrupt changes in the cost function landscape upon varying a control parameter, and can be revealed by non-analytic points in statistical order parameters. A prime example are quantum speed limits (QSL) which mark the onset of controllability as the protocol duration is increased. Here we lay the foundations of an analytical theory for CLPTs by developing Dyson, Magnus, and cumulant expansions for the cost function that capture the behavior of CLPTs with a controlled precision. Using linear and quadratic stability analysis, we reveal that CLPTs can be associated with different types of instabilities of the optimal protocol. This allows us to explicitly relate CLPTs to critical structural rearrangements in the extrema of the control landscape: utilizing path integral methods from statistical field theory, we trace back the critical scaling of the order parameter at the QSL to the topological and geometric properties of the set of optimal protocols, such as the number of connected components and its dimensionality. We verify our predictions by introducing a numerical sampling algorithm designed to explore this optimal set via a homotopic stochastic update rule. We apply this new toolbox explicitly to analyze CLPTs in the single- and two-qubit control problems whose landscapes are analytically tractable, and compare the landscapes for bang-bang and continuous protocols. Our work provides the first steps towards a systematic theory of CLPTs and paves the way for utilizing statistical field theory techniques for generic complex control landscapes.

I. INTRODUCTION

Ever since quantum systems have become an object of investigation, the question of how to manipulate them optimally has been central to both verifying and understanding the theory behind quantum mechanics, as well as to developing new experimental techniques. Nowadays, control theory has become an indispensable tool in emerging quantum technologies [1-3]: efficient quantum state manipulation is an essential prerequisite for the experimental realization of simulations on modern intermediate-noise-scale quantum devices [4–6], for the improvements of performance in quantum measurement devices [7–11] or quantum information processing [12– 16. In general, quantum control theory aims to find protocols that optimize the values of physical quantities of interest: e.g., in a state or gate preparation problem one is typically interested in minimizing the infidelity or the expectation values of a certain physical observable such as the energy or the total magnetization [17, 18].

However, the problem of finding optimal control protocols poses the formidable challenge of searching through high- or infinite-dimensional protocol spaces. The difficulty in finding analytical solutions arises from the lack of explicit expressions for the solution of the timedependent Schrödinger equation, even for the simplest of quantum systems [3, 4]. This motivated the development of an array of numerical optimal control algorithms. Among them, two classes can be distinguished, namely gradient-based methods (e.g., GRAPE [19] and Krotov [20]) and gradient-free algorithms (e.g., CRAB [21, 22]). The former class uses the differentiability of the cost function; the latter relies on a clever sampling of the search space and identifies an optimal protocol through direct search methods [23, 24]. Nonetheless, these algorithms face notable limitations for many-body systems, where an efficient and reliable simulation of the dynamics depends on entanglement remaining low, which is not guaranteed away from the adiabatic regime or in the absence of spectral a gap [4, 22, 25, 26].

In addition, the optimization dynamics depends strongly on the structure of the underlying quantum control landscape; the latter is defined by an objective that measures the performance of solving the optimization task, and is a functional of the protocol configuration [27]. Structural properties of the landscape, such as the number of local minima or saddle-points, highly depend on both the quantum system and the control parameter space [28, 29]. For instance, the landscape associated with ground state preparation in a strongly correlated chain of qubits was shown to possess an exponential number of almost-optimal control protocols as local landscape minima, and a connection between quantum control landscapes and glassy systems was established [30]. In general, despite the large amount of work, surprisingly little is known about properties of quantum control landscapes associated to (non-integrable) interacting quantum systems [28, 31–35].

The bridge between quantum control landscapes and the physics of glassy-systems is clear once the cost function (defining the landscape) is interpreted as an

^{*} nbeato@pks.mpg.de

[†] pranay.patil@oist.jp

[‡] mgbukov@pks.mpg.de

effective-energy function, with control parameters playing the role of classical degrees of freedom [36–39]: from this point of view, optimal protocols correspond to ground states of the effective-energy function. In particular, once the cost function is expanded in terms of the control variables, the nth-order expansion coefficient specifies the strength of the n-body effectiveinteraction between control variables. So far, the calculation of different terms in the expansion has required the (brute-force) exhaustive exploration of the entire control space [30], a procedure computationally feasible only for a small number of control parameters. Nonetheless. this approach captures two important properties of effective interactions between control variables, long-range and multi-body interactions, naturally reflecting the nonlocality and nonlinearity of the underlying quantum control problem.

Curiously, the quantum control landscapes associated with few- and multi-qubit state-preparation have been shown to exhibit critical structural changes, called "Control Landscape Phase Transitions" (CLPTs), as the protocol duration is increased [30, 40, 41]. The name derives from sharp non-analytic behavior arising at the transition point in an order parameter that quantifies the correlations between minima in the optimization landscape. In light of the connection mentioned above between optimization problems and classical statistical physics, CLPTs are naturally associated with phase transitions occurring in the classical effective model. Moreover, since CLPTs are related to structural changes in the optimization landscape, they may affect the complexity of the underlying control problem. Therefore, an accurate analysis of CLPTs is an important step towards developing a better understanding of quantum control landscapes, and shall provide new insights for improving existing optimization algorithms. Despite the clear numerical evidence for their existence, no analytical characterization of CLPTs has been developed.

In this work, we combine analytical and numerical methods to investigate different CLPTs occurring in two prototypical quantum control setups: the single- and two-qubit state preparation problem. First, we propose different controlled approximations for the quantum control landscape and we study to which extent they reproduce the CLPTs present in the exact landscape. In particular, the central object is the evolution operator, which we expand using different analytical expansions (Dyson, Magnus, and cumulants); the cost function landscape (i.e., the infidelity in the case of state-preparation or a physical observable in the case of observable optimization) is then obtained by projection onto the initial and target quantum states. Remarkably, the analytical expansions decouple the controlled quantum degrees of freedom from the control fields so that the general framework remains valid for arbitrary quantum systems. From this result, we conjecture that CLPTs are ubiquitous in optimal control, and should be found for both quantum or classical dynamical systems. Finally, our method treats

piecewise-continuous and bang-bang protocols on equal footing: the coefficients in the landscape expansions do not depend on the family of control protocols, but the landscapes do.

Second, we use the analytical expansion of the land-scape to characterize CLPTs in single- and two-qubit setups. By working in the continuous protocol space, we make a precise connection between non-analytic behaviors of order parameters and structural rearrangements in the landscape. In particular, we keep track of optimal protocols while increasing adiabatically the duration of the quantum evolution; this reveals CLPTs to be associated with different kinds of instabilities of the optimal protocols present in the landscape. This method is independent of the controlled quantum system and is an additional method to detect and characterize CLPTs.

Third, the landscape expansions allow us to estimate analytically the critical scalings of order parameters at the quantum speed limit phase transition. To this end, we first frame the problem in the context of statistical field theory by defining an appropriate partition function. Then, we evaluate the partition function, defined via path integral, within a Gaussian approximation.

Our work is a first attempt to apply methods from statistical field theory, designed to investigate generic complex optimization landscape [39, 42–47], to study quantum control landscapes [4, 28, 29]. The framework developed here is largely independent of the underlying control problem and provides a solid starting point for analyzing more complex systems.

This paper is organized as follows. In Sec. II we introduce the control problems we later use to benchmark our theory and discuss the corresponding control phase diagrams. In Sec. III we derive the analytical expansions for the quantum control landscape and discuss their interpretation from the point of view of classical spin-models in statistical physics. In Sec. IV we discuss how CLPTs are connected to structural changes in the optimal level set, i.e. the set of control protocols that minimize the cost function. In particular, using linear and quadratic stability analysis we detect and classify different CLPTs. In Sec. V we introduce a sampling algorithm based on the Metropolis-adjusted Langevin dynamics, revisit the QSL phase transition for continuous protocols, and study the properties of the optimal level set beyond the QSL. Finally, in Sec. VI we estimate the critical scaling of the order parameters at the QSL phase transition, in both cases of continuous and bang-bang protocols.

II. TOY MODELS FOR QUANTUM CONTROL LANDSCAPE PHASE TRANSITIONS (CLPTS)

Consider the generic control problem

$$\hat{H}(t) = \hat{H}_0 + s(t)\hat{H}_1,\tag{1}$$

where the Hamiltonian is divided between a constant "drift" term \hat{H}_0 and a time-varying "control" term

 $s(t)\hat{H}_1$. The control parameter s, regarded as a function of time t, is called control "protocol" (or "schedule"). In the qubit systems we consider below, the protocol modulates the external magnetic field in time, but more generic controls are also frequently used in experiments. To stay away from the trivial adiabatic limit, we consider a fixed protocol duration T of the order of the inverse energy scale in the drift term, $i.e., T \sim ||\hat{H}_0^{-1}||$, and track evolution times $t \in [0,T]$. Consistently with typical limitations in present-day experiments [48], we assume a bounded control term \hat{H}_1 and restrict the problem to the class of bounded functions $|s(t)| \leq 1$, $\forall t \in [0,T]$.

We are interested in CLPTs emerging in state-preparation problems. Let us denote the initial state of the system by $|\psi_0\rangle$, and the target state (*i.e.*, the state we want to prepare) – by $|\psi_*\rangle$. Notice that the control term $s(t)\hat{H}_1$ modifies the bare drift evolution of the system. The optimal control problem then consists in finding those protocols $s_*(t)$ that achieve a maximum overlap between the target $|\psi_*\rangle$ and the time-evolved state $|\psi(t)\rangle = \hat{U}_s(t,0) |\psi_0\rangle$ at the final time t=T; in other words, given T we want to find (all) the protocols s(t) that minimize the so-called "infidelity",

$$I_T[s] = 1 - \left| \langle \psi_* | \hat{U}_s(T, 0) | \psi_0 \rangle \right|^2,$$
 (2)

where $\hat{U}_s(T,0) = \mathcal{T}e^{-i\int_0^T dt \hat{H}(t)}$ is the time-ordered evolution operator, dependent on the time-varying protocol s.

The infidelity defines a functional over protocol space (i.e., the space of all control functions), $s\mapsto I_T[s]$, henceforth referred to as the "quantum control landscape"; the latter depends both on the specifics of the Hamiltonian $\hat{H}(t)$ and the details of the controlled system. Each point s of the infidelity landscape corresponds to a unique protocol s(t); optimal protocols by definition reside in the (possibly many) global infidelity minima. By introducing both analytical and numerical techniques, we will analyze changes in the structure of minima in the control landscape in few-qubit systems, as we vary the protocol duration T.

The quantum state preparation problem associated with few-qubit Hamiltonians of the form (1) was first studied in Refs. [41] and [30]. In particular, the search for optimal protocols was restricted to the so-called 'bangbang' class, where |s(t)| takes its maximum allowed value. This restriction is formally motivated within the framework of Pontryagin's Maximum Principle which, under certain conditions, guarantees the existence of at least one optimal protocol within the bang-bang class [49]; that said, some control problems have optimal protocols mixing bang-bang and continuous parts [50]. Concretely, the time axis [0, T] is divided in N equidistant time steps $\{t_1,\ldots,t_N\}$ and hence $s(t_i)=s_i=\pm 1$ at each time step t_i . Optimal control algorithms, such as Stochastic Descent, can then be used to collect a set of M (locally) optimal protocols, $S = \{s^{(1)}, \dots, s^{(M)}\}$ as a probe for the structure of minima in the quantum control landscape.

The piecewise-constant bang-bang protocol $s=\{s_i\}$ can be regarded as classical Ising spin degrees of freedom while the infidelity landscape, $I_T[s]$, defines an effective Ising energy function. The corresponding spin model

$$I_T[s] = c(T) + \frac{1}{N} \sum_{j=1}^{N} b_j(T) s_j + \frac{1}{2N^2} \sum_{i,j}^{N} J_{ij}(T) s_i s_j + \cdots$$

can exhibit CLPTs, numerically investigated in Ref. [40]. Note that, despite the discretization of time, there is no underlying regular lattice structure, *i.e.*, the control landscape is effectively an infinite-dimensional system (although discretized time induces a natural ordering of the lattice sites).

CLPTs can be detected using the order parameter

$$q(T) = \frac{1}{N} \sum_{i=1}^{N} \left[\left\langle s_i^2 \right\rangle_{\mathcal{S}} - \left\langle s_i \right\rangle_{\mathcal{S}}^2 \right], \tag{4}$$

which is closely related to the Edwards-Anderson order parameter used to measure spin-glass order [39, 47]. Here, $\langle s_i \rangle_{\mathcal{S}}$, $\langle s_i^2 \rangle_{\mathcal{S}}$ represent the average on site i over the set of (locally) optimal protocols \mathcal{S} . By definition, q(T) quantifies fluctuations among the set \mathcal{S} with respect to the average protocol $\langle s \rangle_{\mathcal{S}}$. Within the bang-bang family, we can further simplify q(T) to

$$q_{\rm BB}(T) = 1 - \frac{1}{N} \sum_{i=1}^{N} \langle s_i \rangle_{\mathcal{S}}^2.$$
 (5)

For convex landscapes, the set S contains a single protocol, and we have $q_{\rm BB}(T)\equiv 0$. On the other hand, whenever protocols in S are uncorrelated, we have $\langle s_i \rangle_S^2 = 0$, and $q_{\rm BB}(T)\equiv 1$. Intermediate values of q(T) correspond to correlations between protocols in S.

Little is known about the nature and origin of control phase transitions in general. Despite their formal resemblance to k-SAT problems and spin glasses [39], their analytical study is hampered by the lack of techniques to determine the form of the coupling constants c, b_i, J_{ij} in the energy function $I_T[s]$. A primary reason for this is the infinite character of the energy function in Eq. (3), comprising both long-range and multi-body terms, which pose a daunting challenge for analytical studies. In turn, although numerical methods allow us to sample the control landscape and map out the corresponding phase diagram, they prove insufficient when it comes to determining and understanding the detailed mechanisms that drive these phenomena. In this paper we focus on two few-qubit toy models, which allow us to make progress analytically. Before diving into the details, we first briefly revisit their control phase diagrams and summarize the properties of the existing control phases.

A. Single-qubit control landscape

Consider the single-qubit system

$$\hat{H}(t) = h_z \hat{S}^z + s(t) h_x \hat{S}^x, \tag{6}$$

where \hat{S}^{α} , $\alpha = x, y, z$ are the spin-1/2 operators. The control problem we investigate aims to prepare the target state $|\psi_*\rangle = |\mathrm{GS}(h_x/h_z = -2)\rangle$, starting from the initial state $|\psi_0\rangle = |\mathrm{GS}(h_x/h_z = 2)\rangle$; $|\mathrm{GS}(h_x/h_z)\rangle$ denotes the ground state of the Hamiltonian specified by the ratio h_x/h_z (with s=1). In addition, we fix the protocol duration T and set, throughout the evolution, $h_z = -1, h_x = -\sqrt{5}$ (i.e. s(t) is the only time-dependent parameter). Even though precise values of the control problem parameters affect the CLPTs' locations, the qualitative picture remains unaffected.

In Fig. 1a we show the corresponding bang-bang control phase diagram as a function of the parameter T. For $T < T_c$, the order parameter vanishes $(q_{BB}=0)$ and hence there exists a single optimal protocol. At $T=T_c$ the bang-bang infidelity landscape suddenly acquires additional local minima, associated with a cusp in $q_{\rm BB}$. While a simple physical picture shows that at the critical duration T_c a singular arc appears in the optimal protocol [3, 40], little is known about how the underlying microscopic spin model $I_T[s]$ determines the properties of $q_{\rm BB}(T)$, including the critical exponent at the transition. For $T_c \leq T \leq T_{QSL}$, the bang-bang infidelity landscape exhibits, in addition to a unique global minimum, multiple almost-optimal local minima; the correlations among these minima give rise to a finite value $0 < q_{\rm BB} < 1$. At the quantum speed limit, $T=T_{OSL}$, the landscape undergoes a second phase transition where the number of global minima proliferates; a second non-analytic point in $q_{\rm BB}(T)$ emerges. It is currently unclear how the presence of a finite quantum speed limit modifies the structure of the energy function $I_T[s]$, nor how these changes affect the behavior of the order parameter $q_{BB}(T)$.

B. Two-qubit control landscape

While the control landscape of the single-qubit problem in Eq. (6) is not fully understood, finding the optimal protocol is rather straightforward due to the simplicity of the qubit system [51]. Therefore, we also investigate a two-qubit model

$$\hat{H}(t) = J\hat{S}_1^z\hat{S}_2^z + h_z(\hat{S}_1^z + \hat{S}_2^z) + s(t)h_x(\hat{S}_1^x + \hat{S}_2^x)$$
 (7)

with h_z, h_x as in the single-qubit problem and J=-2. The two qubits are coupled via an Ising interaction J, and are exposed to a constant global z-field, and a time-varying global x-field. The initial and target states read as $|\psi_0\rangle = |\mathrm{GS}(h_x/h_z=2,J/h_z=1)\rangle$ and $|\psi_*\rangle = |\mathrm{GS}(h_x/h_z=-2,J/h_z=1)\rangle$. To the best of our knowledge, the exact solution to the corresponding constrained optimal control problem in Eq. (7) is unknown.

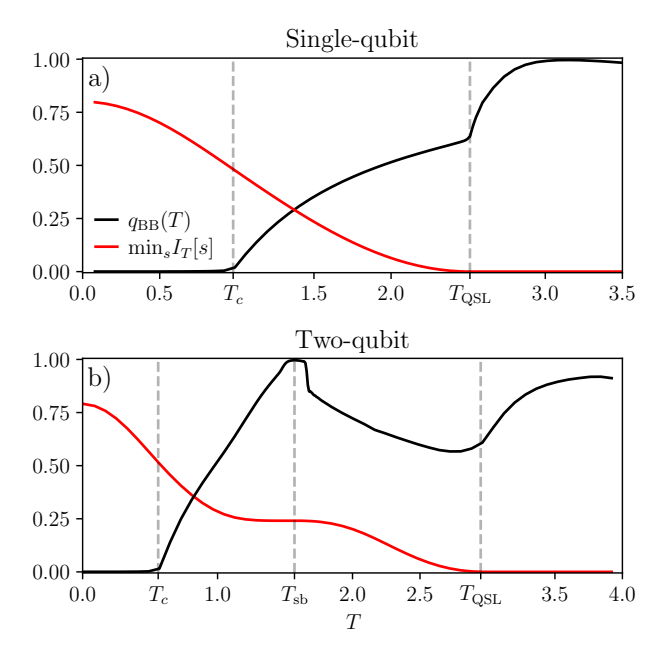


FIG. 1. Control Landscape Phase Transitions (CLPTs) in the single- (a) and two-qubit (b) control problems. The curves shown are obtained from Stochastic Descent (SD) algorithm in the exact infidelity landscape, searching in the space of bang-bang protocols. The minimum infidelity $\min_s I_T[s]$ and the order parameter $q_{BB}(T)$ (cf. Eq. (5)) are shown as a function of the protocol duration T for a fixed number of bang-bang steps. Non-analytic points in the order parameter $q_{BB}(T)$ mark control landscape phase transitions (dashed vertical lines). Similar transitions appear in both control problems: at $T=T_c$, and at $T=T_{QSL}$ (where the infidelity vanishes). The two-qubit problem possesses an additional symmetry-breaking transition at $T=T_{\rm sb}$ related to the separation of the set of optimal protocols into two separated subsets which break the $s(t) \leftrightarrow -s(T-t)$ symmetry of the control problem [41].

This two-qubit model will allow us to study the wider applicability of the techniques we develop.

For $J{=}0$, we recover the single-qubit problem discussed above; in particular, the control phase diagram exhibits an overconstrained phase $(T{<}T_c)$, and a fully controllable phase $T{>}T_{\rm QSL}$, separated by a correlated phase $T_c{\le}T{\le}T_{\rm QSL}$ (cf. Fig. 1b and Ref. [41]). However, for finite values of J, additional phases appear in the control landscape.

In Ref. [41] it was shown that the infidelity function features an Ising \mathbb{Z}_2 symmetry:

$$I_T[s(t)] = I_T[-s(T-t)],$$
 (8)

corresponding to the simultaneous application of a protocol time-reversal symmetry $s(t) \rightarrow s(T-t)$ and global flip of the x/y-projection $\hat{S}_j^{x/y} \rightarrow -\hat{S}_j^{x/y}$. On the level of the effective classical spin model, the same \mathbb{Z}_2 symmetry manifests itself as a global spin flip, combined with a reflection about the center of the lattice: $s_j \rightarrow -s_{N-j}$. The

presence of this symmetry hinges on the choice of initial and target states.

Interestingly, symmetry breaking occurs within the correlated phase of the two-qubit bang-bang control phase diagram (cf. Fig. 1(b)), at a critical protocol duration $T_{\rm sb}$. This leads to a doubly degenerate optimal level set that features two global minima, whose protocols can be transformed to one another by the symmetry operation. Moreover, the order parameter $q_{\rm BB}$ exhibits a discontinuity at the symmetry-breaking transition $T_{\rm sb}$. The same \mathbb{Z}_2 symmetry is present in the singlequbit control problem (6), as well as in the corresponding multi-qubit generalization [40]; nevertheless, rather mysteriously, the corresponding landscapes do not feature a symmetry-broken phase [30]. While this phenomenon was discovered and studied numerically, at present, it is not known what the necessary and sufficient conditions for it to occur are; it is also unclear what its relation to the other control phase transitions is.

In the following, we develop and discuss techniques to derive analytical expressions for the quantum control landscape. This allows us to go beyond bang-bang protocols and investigate the corresponding landscapes defined over the piecewise-continuous protocol space.

III. PERTURBATIVE EXPANSIONS FOR THE CONTROL LANDSCAPE

We now proceed to present a systematic derivation of the analytical expansion for the infidelity landscape, cf. Eq. (3), using three different controlled techniques: the Dyson, Magnus, and cumulant expansion. We test their accuracy, when truncated to the leading few orders, and compare and contrast their ability to capture the transitions in the control phase diagrams of the single-and two-qubit toy models.

A. Analytical expansions for the infidelity

Consider the general case of continuous protocols s(t). We can write down a general expansion of the infidelity $I_T[s]$ functional as

$$I_T[s] = c(T) + \int_0^T dt \, b_t(T) s_t + \frac{1}{2} \int_0^T d^2t \, J_{t_1 t_2}(T) s_{t_1} s_{t_2} + \cdots$$
(9)

with some a priori unknown coefficients c(T), $b_t(T)$, $J_{t_1t_2}(T)$,... that depend parametrically on the protocol duration T. At the level of the underlying effective spin model, as the notation suggests, they play the role of a constant shift, an external field, and a two-body interaction strength, respectively.

To determine these unknown coefficients, we rewrite Eq. (2) in terms of the density matrix associated with the quantum state $\hat{U}_s(T,0)|\psi\rangle$. In an N-qubit system, a generic density matrix can be expanded as

 $\rho = |\psi\rangle\langle\psi| = d^{-1} + \hat{\vec{S}} \cdot \vec{n} \text{ where } d = 2^N \text{ is the Hilbert space dimension and the vector } \hat{\vec{S}} \text{ contains all traceless spin operators acting on the Hilbert space (e.g., Pauli or Gell-Mann matrices for a qubit or qutrit system, respectively; Pauli strings for a qubit chain) and we choose the normalization convention <math>\text{Tr}\left\{\hat{S}^i\,\hat{S}^j\right\} = \delta_{ij}/2$ with $i,j=1,\ldots,d^2-1$. Notice that to each quantum state $|\psi\rangle\in\mathbb{C}^d$ corresponds a real "dual" vector $\vec{n}\in\mathbb{R}^{d^2-1}$; in terms of the dual vector \vec{n} , the infidelity becomes

$$I_{T}[s] = 1 - \left| \langle \psi_{*} | \hat{U}_{s}(T,0) | \psi_{0} \rangle \right|^{2}$$

$$= 1 - \langle \psi_{*} | \hat{U}_{s}(T,0) \rho_{0} \hat{U}_{s}(T,0)^{\dagger} | \psi_{*} \rangle$$

$$= 1 - \langle \psi_{*} | \left(d^{-1} + \hat{U}_{s}(T,0) \, \hat{\vec{S}} \, \hat{U}_{s}(T,0)^{\dagger} \cdot \vec{n}_{0} \right) | \psi_{*} \rangle$$

$$= 1 - d^{-1} - \langle \psi_{*} | \, \hat{\vec{S}} | \psi_{*} \rangle \, M_{s}(T,0) \, \vec{n}_{0}$$

$$= 1 - d^{-1} - (1/2) (\vec{n}_{*} \cdot M_{s}(T,0) \, \vec{n}_{0}). \tag{10}$$

The rotation matrix $M_s(T,0)$, which we refer to as control propagator, defines the representation of the unitary evolution group on the dual space \mathbb{R}^{d^2-1} ; in other words, the quantum evolution operator is replaced by the orthogonal evolution operator over the space of real (d^2-1) -dimensional vectors \vec{n} . Explicitly, $(M_s(T,0))_{ij}=2\operatorname{Tr}(\hat{S}^i\hat{U}_s(T,0)\hat{S}^j\hat{U}_s(T,0)^{\dagger})$.

A few remarks are in order: (i), note that by going to the dual description, we manage to swap the original quantum expectation values for an "expectation" in the vectors \vec{n}_{0*} ; in a sense, the quantum nature of the original problem is now hidden in the dual space dimension which grows faster than the qubit Hilbert space size. This indicates that any transitions in the control landscape are not quantum by nature, but merely classical: (ii), on a technical level, the above procedure allows us to eliminate the absolute value square in the definition of the infidelity; this is useful since it will allow us to more easily find the expression for the landscape from Eq. (9); (iii), notice that this procedure is generic and applies to control problems where the cost function is defined in terms of observables (e.g., energy minimization) that possess easy-to-identify expansions in operator space: one simply has to replace ρ_0 by the corresponding observable. Last but not least, (iv), we have managed to reduce the problem of computing the infidelity landscape to the problem of expanding the control propagator $M_s(T,0)$ in terms of the protocol s(t).

To make further progress analytically, let us write the control propagator $M_s(T,0)$ as

$$M_s(T,0) = \mathcal{T}e^{\int_0^T m_s(t)dt}, \qquad (11)$$

where $m_s(t)$ is the anti-symmetric matrix generating the rotation $M_s(T)$; assuming the relation $[\hat{S}^i, \hat{S}^j] = i f_{ijk} \hat{S}^k$ with structure constants f_{ijk} , $m_s(t)$ can be computed directly from the Hamiltonian as $(m(t))_{ij} = \sum_k f_{ijk} 2 \operatorname{Tr} (\hat{S}^k \hat{H}(t))$.

For a general Hamiltonian of the form in Eq. (1), we can separate the time dependence in the generator as $m_s(t)=m_0+s(t)m_1$. However, this additive structure of the generator does not yet allow for a straightforward expansion in terms of the protocol s (see App. A). To circumvent this problem, we now perform a change-of-frame transformation, which leads to an effective re-summation of all relevant subseries [52]. To this end, we use a rotating frame transformation on the level of the generator, resulting in

$$m_s(t) \mapsto m_s'(t) = M_0(t,0)^{t} [m_s(t) - \partial_t] M_0(t,0), \quad (12)$$

with $M_0(t,0) = \exp(tm_0)$ and $(\cdot)^t$ denotes the matrix transpose. Note that physical quantities, such as the infidelity, remain invariant. Thus, in the primed reference frame, the infidelity can be written as

$$I_s(T) = 1 - d^{-1} - (1/2) \left(\vec{n}_* \cdot M_0(T, 0) M_s'(T, 0) \, \vec{n}_0 \right), \tag{13}$$

where $M_s'(T,0)$ is the transformed evolution operator associated with the generator $m_s'(t)$ in the new reference frame. We can also absorb the s-independent rotation in the target state: $\vec{n}_*'(T) = \vec{n}_* M_0(T,0)$, to simplify notation. The only remaining protocol-dependent quantity is now the control propagator $M_s'(T,0)$; hence, in the following, we seek a matrix-valued expansion in powers of

Dyson expansion. The Dyson series associated with $M_s'(T,0)$ reads as

$$M'_s(T,0) = \mathbb{1} + \int_0^T dt \, \partial_s m'_s(t)s(t)$$

$$+ \frac{1}{2} \int_0^T d^2t \, \mathcal{T}[\partial_s m'_s(t_1)\partial_s m'_s(t_2)]s(t_1)s(t_2)$$

$$+ \dots \qquad (14)$$

We can now easily read off the infidelity expansion coefficients in Eq. (9):

$$c(T) = 1 - d^{-1} - (1/2) (\vec{n}'_*(T) \cdot \vec{n}_0)$$

$$b_t(T) = -(1/2) (\vec{n}'_*(T) \cdot \partial_s m'_s(t) \vec{n}_0)$$

$$J_{t_1t_2}(T) = -(1/2) (\vec{n}'_*(T) \cdot \mathcal{T}[\partial_s m'_s(t_1) \partial_s m'_s(t_2)] \vec{n}_0)$$
(15)

and similarly for higher-order terms. We have thus obtained explicit closed-form expressions for all coefficients in the infidelity expansion, which define the control land-scape. Remarkably, the whole series expansion can be explicitly written once the quantity $\partial_s m_s'(t)$ is known.

As a side note, notice that when restricted to bangbang-protocols, a second-order truncation of the series expansion yields an effective classical spin model that bears resemblance to the well-known Hopfield network [39].

It now becomes clear that the (matrix-valued) control propagator $M'_s(T,0)$ generates the control landscape. In particular, sandwiching it between \vec{n}'_* and \vec{n}_0 projects

to a specific landscape for any choice of initial and target states, and ultimately produces the corresponding infidelity expansion coefficients in Eq. (9). Moreover, by choosing \vec{n}'_* appropriately, we can obtain the corresponding control landscape also for observables, e.g., when minimizing the energy, or maximizing the expectation of some spin component, etc. Therefore, the control propagator is a fundamental object of control landscape theory.

As we will see below, the Dyson series is one example of a functional expansion for the infidelity. In particular, Eq. (15) corresponds to the infidelity functional-Taylor expansion centered around the protocol s=0 (written in terms of the orthogonal generator $m'_s(t)$). In App. A we generalize this result to an arbitrary center $s\neq 0$ and a generic reference frame; moreover, we derive the expansion for both unitary and orthogonal evolution operators. In Sec. IV we use these these general expressions to study the near-optimal region of the control landscape.

A well-known deficiency of the *truncated* Dyson series for the evolution operator is the violation of orthogonality of the resulting approximate operator; as a result, the corresponding Dyson-expanded infidelity landscape may not be restricted to the interval [0,1].

Magnus expansion. A possible remedy to the unitarity/orthogonality loss is given by the Magnus expansion [53–55] for control propagator $M'_s(T,0)$:

$$M_s'(T,0) = \exp\left[\sum_{n=1}^{\infty} \Omega_{n,s}(T,0)\right]$$
(16)

where the first few terms read as [56]

$$\begin{split} \Omega_{1,s}(T,0) &= \int_0^T \mathrm{d}t \, \partial_s m_t' s_t, \\ \Omega_{2,s}(T,0) &= \frac{1}{2} \int_0^T \int_0^{t_1} \mathrm{d}^2 \, t \, [\partial_s m_{t_1}', \partial_s m_{t_2}'] s_{t_1} s_{t_2}, \\ \Omega_{3,s}(T,0) &= \frac{1}{6} \int_0^T \int_0^{t_1} \int_0^{t_2} \mathrm{d}^3 t \, \Big([\partial_s m_{t_1}', [\partial_s m_{t_2}', \partial_s m_{t_3}']] \\ &+ [[\partial_s m_{t_1}', \partial_s m_{t_2}'], \partial_s m_{t_3}']] s_{t_1} s_{t_2} s_{t_3} \Big). \end{split}$$

Owing to its structure, truncating the Magnus series at finite order yields an orthogonal operator and the resulting fidelity respects the [0,1] interval bound. Notice that the exponential map acting on the truncated expansion generates infinitely many terms that are absent in the Dyson expansion. However, the Magnus expansion does not allow for a direct scalar effective-energy interpretation since its terms are matrix-valued (i.e. generators of the rotation group $SO(N^2-1)$).

Cumulant expansion. Substituting the Magnus expansion in Eq. (10), we find

$$I_T[s] = 1 - d^{-1} - (1/2)\vec{n}'_* \cdot \exp(\Sigma)\vec{n}_0$$

where Σ compactly denotes the Magnus expansion.

Rewriting $I_T[s]=1-e^{\log(1-I_T[s])}$ we can expand the logarithm using the so-called cumulant expansion as

$$\log(1 - I_T[s]) = \log \frac{2d^{-1} + \vec{n}'_* \cdot \exp(\Sigma)\vec{n}_0}{2} = \sum_{m=0}^{\infty} \frac{\kappa_m}{m!}.$$
(17)

This expansion is common in statistical mechanics, where the free energy F, linked to the partition function Z through the identity $-\beta F = \log Z$, is typically expanded in cumulants. In the present case, the fidelity $1-I_T[s]$ plays the role of the partition function. The first few terms of the cumulants expansion read as

$$\begin{split} \kappa_0 &= \log \frac{2d^{-1} + \vec{n}_*' \cdot \vec{n}_0}{2} \\ \kappa_1 &= \frac{\vec{n}_*' \cdot \Sigma \vec{n}_0}{2d^{-1} + \vec{n}_*' \cdot \vec{n}_0} \\ \kappa_2 &= \frac{\vec{n}_*' \cdot \Sigma^2 \vec{n}_0}{2d^{-1} + \vec{n}_*' \cdot \vec{n}_0} - \left(\frac{\vec{n}_*' \cdot \Sigma \vec{n}_0}{2d^{-1} + \vec{n}_*' \cdot \vec{n}_0}\right)^2. \end{split}$$

We now turn to the quality of the three infidelity expansions presented. Since we want to develop a technique to better understand the near-optimal region of the quantum control landscape, it is important to quantify the extent to which the infidelity expansions reproduce the behavior of already known quantities, such as the non-analytic points in the order parameter $q_{\rm BB}(T)$ across control phase transitions. For this reason, in the following, we compare the three expansions using the two toy models introduced in Sec. II.

B. Single-qubit problem

So far the discussion was carried out for a generic quantum system. In the case of Hamiltonian (6) one obtains

$$m'_{s}(t) = h_{x}s(t)[T_{x}\cos(h_{z}t) + T_{y}\sin(h_{z}t)],$$
 (18)

where $\{T_i\}_{1}^{3}$ are the generators of the group SO(3) defined by $(T_i)_{jk} = \epsilon_{ijk}$, with ϵ_{ijk} the SO(3) structure constants. We emphasize that having a closed-form expression for $m'_s(t)$ is sufficient to generate any (multi-body) coupling term in the Dyson expansion for the infidelity landscape.

In Fig. 2 we evaluate the performance of the three infidelity expansions using Stochastic Descent (see App. B). Since our motivation to introduce the expansions is the study of the quantum landscape transitions, we benchmark the three methods using the order parameter $q_{\rm BB}(T)$, introduced in Eq. (5).

In our simulations, we truncate Dyson and Magnus expansions up to third order. The computational cost of a single infidelity evaluation grows polynomially, $\mathcal{O}(N^{\alpha})$, where N is the number of time steps and α is the order of truncation of the expansion which sets the dimensions of the multidimensional integral appearing in the highest term of the expansion [57]. The cumulant expansion is

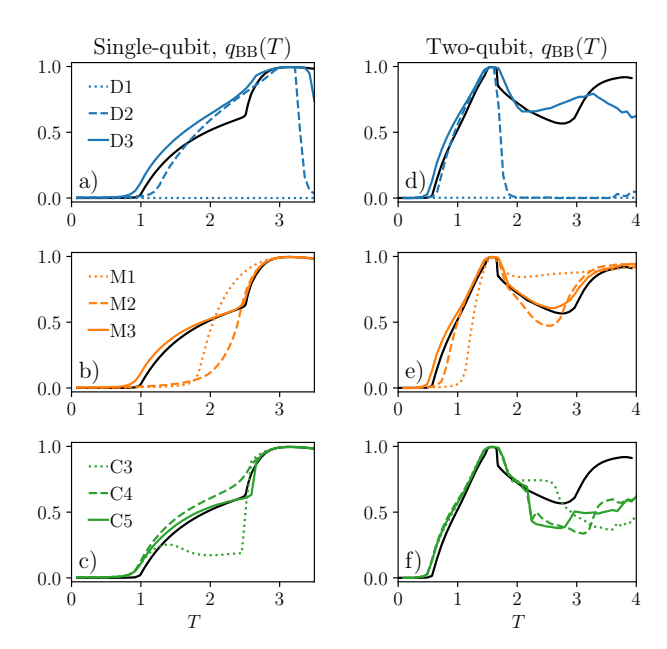


FIG. 2. Comparison of the order parameter $q_{BB}(T)$ (cf. Eq. (5)) obtained from Stochastic Descent (SD) in the landscape defined by the infidelity expansions introduced in Sec. III, in the single- and two-qubit control problem. The black curve refers to the exact infidelity landscape in Eq. (2). The letters D, M, and C in the legend stand for Dyson, Magnus, and Cumulant expansion while the adjacent integer specifies the order of truncation. Single-qubit: The $T=T_c\simeq 0.98$ transition is approximately captured by all three methods. The second transition at $T=T_{QSL}\simeq 2.51$ is only visible in the Magnus and Cumulants results. Two-qubit: The $T=T_c\simeq 0.56$ and $T=T_{\rm sb}\simeq 1.57$ transitions are approximately captured by all three methods. The non-analytic point at $T=T_{\rm QSL}\simeq 2.95$ is less sharp than the corresponding point in the single-qubit problem and only the Magnus expansion truncated at third order is able to reproduce the qualitative behavior of the exact curve.

obtained from the Magnus expansion and its computational cost depends on the truncation order of the Magnus expansion.

The first transition around T_c is clearly visible in all the three expansions within the truncation orders considered. While the Dyson expansion is not able to capture the $T_{\rm QSL}$ transition at third-order, the Magnus and cumulants expansions results follow remarkably well the exact curve $q_{\rm BB}(T)$ (at third- and fifth-order, respectively). Thus, we conclude that higher than third-order terms, generated in the Magnus expansion from the exponential map but completely absent in the other two expansions, are essential to reproduce CLPTs in the exact infidelity landscape.

C. Two-qubit problem

Let us apply our theory to the two-qubit problem from Eq. (7). The rotating frame is defined by removing the drift term \hat{H}_0 from the Hamiltonian. In this case, the drift term has two contributions $\hat{H}_0 = \hat{H}_{0,1} + \hat{H}_{0,2}$,

$$\hat{H}_{0,1} = h_z \hat{S}_{\text{tot}}^z, \qquad \hat{H}_{0,2} = J S_1^z S_2^z.$$

Since $[\hat{H}_{0,1}, \hat{H}_{0,2}] = 0$, the reference frame transformation factorizes as $\hat{U}_0 = \hat{U}_{0,1}\hat{U}_{0,2}$. A straightforward calculation shows that

$$\hat{H}'(t) = s(t)h_x \hat{U}_{0,2}^{\dagger} \left[\cos(h_z t) \hat{S}_{\rm tot}^x - \sin(h_z t) \hat{S}_{\rm tot}^y \right] \hat{U}_{0,2}$$

where $\hat{U}_{0,2}$ is a diagonal operator in the computational z-basis.

In this case, the two-qubit quantum control problem allows for an orthogonal decomposition of the Hamiltonian operator into the triplet and singlet subspaces; moreover, the quantum states $|\psi_{0,*}\rangle$ have no component in the singlet subspace. Hence, we may restrict $\vec{S} = \vec{\lambda}/2$ to the SU(3) basis defined by Gell-mann matrices $\vec{\lambda}$. Explicitly, in the dual description we have:

$$m'_{s}(t) = s(t)\sqrt{2}h_{x}(T_{1}\cos(h_{z}t + Jt/2) + -T_{2}\sin(h_{z}t + Jt/2) + +T_{6}\cos(h_{z}t - Jt/2) + -T_{7}\sin(h_{z}t - Jt/2))$$
(19)

where the generators $\{T_i\}_{1}^{8}$ are given by $(T_i)_{jk} = f_{ijk}$ with f_{ijk} the SU(3) structure constants.

Stochastic Descent results for the two-qubit problem are reported in Fig. 2. Both the T_c and $T_{\rm sb}$ transitions are captured by the three expansions. In the latter case, the jump discontinuity of $q_{\rm BB}(T)$ is smoothened out by the approximated landscape. On the contrary, the $T_{\rm QSL}$ transition is partially captured only by the Magnus expansion truncated at third order.

A final remark is in order. In this section, we used the infidelity expansions, centered around s_0 =0, to detect CLPTs of the exact control landscape. The choice of the center s_0 =0 is convenient since it allows us to make no extra assumption regarding the shape of the optimal protocol(s) of the landscape. Nonetheless, as we will see in the next section, better results can be achieved by centering the expansion around carefully chosen protocols $(s_0 \neq 0)$. This can be done whenever additional information regarding the properties of the optimal protocol(s) is known.

IV. STABILITY ANALYSIS AND CONTROL PHASE TRANSITIONS

In the previous section, we introduced three different analytical expansions, for the control landscape, centered around the protocol $s{=}0$. In App. A we discuss the relation with the functional Taylor expansion. This section uses the infidelity Taylor expansion to analyze CLPTs in the single- and two-qubit control problem introduced in Sec. II. Our purpose is two-fold. On the one hand, critical points in the control phase diagram are identified with different types of instability relative to the minimum of the quantum control landscape. On the other, we consider the Taylor expansion as a function of the parameter T to identify and follow the landscape minimum. In particular, we first use the $T{\to}0$ limit to analyze the landscape in a linear approximation, and to identify the structure of the optimal protocol in this limiting case. Subsequently, we track how the optimal protocol changes as we increase T by enforcing "linear stability".

The idea can be understood by using a one-dimensional analogy (see Fig. 3). Let $I = [-1, 1] \subset \mathbb{R}$ and $f: I \to \mathbb{R}$ be a convex function with minimum $x_0 \in I$. The Taylor expansion centered in $x = x_0$ and truncated at second order reads $f(x) = f(x_0) + \frac{\mathrm{d}f}{\mathrm{d}x}\big|_{x_0}(x-x_0) + \frac{1}{2!}\frac{\mathrm{d}^2f}{\mathrm{d}x^2}\big|_{x_0}(x-x_0)^2$. If x_0 does not belong to the boundary $\{-1,1\}$, then the linear term vanishes $\frac{\mathrm{d}f}{\mathrm{d}x} = 0$ and the second order term is positive $\frac{\mathrm{d}^2f}{\mathrm{d}x^2}(x_0) > 0$. Otherwise, if x_0 belongs to the boundary $\{-1,1\}$, the linear term may be finite but then, either f'(x) > 0 if $x_0 = -1$ or f'(x) < 0 if $x_0 = 1$; notice that the two cases are summarized by the condition $\mathrm{sgn}(f'(x_0)) = -\mathrm{sgn}(x_0)$, with sgn the sign function. Finally, if we let $f(x) = f_T(x)$ to also continuously depend on a parameter T, we may then study the behavior of its minimum x_0 as a function of T.

The control landscape (represented by the function $f_T(x)$ in the above analogy) is a functional of the protocol s that depends on the duration of the quantum evolution $T \in [0, \infty)$. Our strategy is based on the continuous dependence of infidelity on the parameter T, and relies on two ideas. First, we use the infidelity expansion around a given protocol s to study its stability under generic perturbations $s+\delta s$. In this case, the stability (instability) of the protocol s depends on whether the infidelity increases (decreases) after the perturbation $s+\delta s$ is applied. Second, by adopting the effective energy interpretation for the infidelity expansion at the onset of instability, we study how the instability affects the optimal protocol. We demonstrate that this procedure is sufficient to map out the control phase diagram up to $T_{\rm QSL}$ and $T_{\rm sb}$ in the one- and two-qubit cases, respectively (cf. Fig. 1).

Notice that the control phase diagram was originally analyzed by searching for optimal configurations in the space of bang-bang protocols [40, 41]. Here, we go beyond this restriction and study the landscape over the continuous protocol space. Interestingly, over continuous protocols, the phenomenology observed in the bang-bang case is preserved. In Sec. VI C we comment on the relation between the control problem defined over bang-bang and continuous protocol spaces.

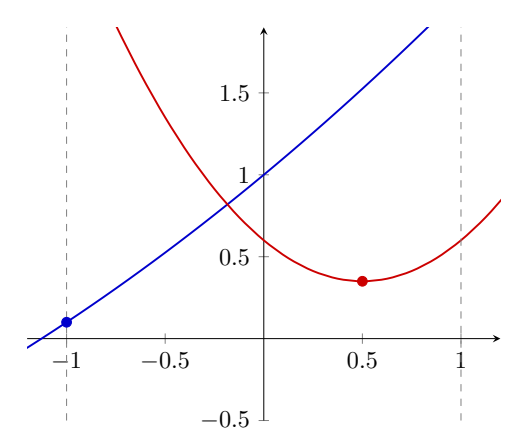


FIG. 3. Two different one-dimensional functions (blue and red curves) illustrating the stability conditions for optimal points in Eq. (20). The minimum of the red curve at x=+0.5 (red dot), lying inside the allowed domain [-1,1], satisfies f'(x)=0, f''(x)>0. The minimum of the blue curve at x=-1 (blue dot), lying at the edge of the allowed domain [-1,1], satisfies f'(x)>0.

A. Breakdown of adiabatic tracing of optimal protocols at the control critical points

Observe that, when expanding the infidelity around a generic protocol $s_0(t)$, the coefficients c(T), $b_t(T)$, $J_{t_1t_2}(T)$ in Eq. (9) depend on s_0 itself: in this section we make this dependence explicit but also keep track of the parametric dependence on the protocol duration T:

$$c[s](T), b_t[s](T), J_{t_1t_2}[s](T),$$
 etc.

We define the linear stability of the protocol s_0 with respect to the infidelity landscape I[s](T) analogously to the one-dimensional example $f_T(x)$ discussed above. The protocol s_0 is "linearly unstable" if

$$b_t[s_0](T) \neq 0$$
 $|s_{0,t}| < 1$
 $-\operatorname{sgn}(b_t[s_0](T)) \neq \operatorname{sgn}(s_{0,t})$ $|s_{0,t}| = 1$ (20)

for some $t \in [0, T]$. The two cases distinguish the situations where s(t) is inside [-1, 1] or at its boundary (see Fig. 3).

As in the one-dimensional example for non-convex functions, one needs in general to define also the quadratic stability of the protocol s_0 . In this case, the second-order coefficient $J_{t_1t_2}[s_0](T)$ plays the role of the Hessian matrix (i.e. the second-order term in the Taylor expansion) for multi-dimensional functions. In particular, the stability of s_0 depends on the set of eigenvalues $\{\lambda_n\}$, defined by [58]

$$\frac{1}{T} \int_{0}^{T} dt' J_{tt'} f_{t'}^{(n)} = \lambda_n f_t^{(n)}, \tag{21}$$

with $\{f_t^{(n)}\}_n$ the eigenfunctions (the dependence on s_0 and T is omitted for simplicity). Then, the protocol s_0 is

"quadratically unstable" if there are negative eigenvalues in the spectrum of the "Hessian operator" $J_{t_1t_2}[s_0](T)$. In practice, we can perform the diagonalization numerically: discretizing the time axis in L equal-size intervals we find the matrix eigenvalue equation:

$$\frac{1}{L} \sum_{j=1}^{L} J_{ij} f_j^{(n)} = \lambda_n f_i^{(n)}, \quad n = 1, 2, \dots, L.$$

In this case, the number of eigenvalues is controlled by the number of discrete segments L we divide our protocol into, and is not strictly physical. We report in App. C the finite-L scaling analysis.

We are now equipped and in a position to introduce each step of the method and discuss the corresponding results for the single- and two-qubit control problems. As a starting point, we consider the limit $T\rightarrow 0^+$ where the infidelity landscape can be approximated by a Taylor series truncated to first order (throughout our work we use the +,- superscripts to distinguish the right- or left-limit, respectively). Expanding around the protocol s=0,

$$I_T[s] \approx I_T[0] + \int_0^T dt \, b_t[0](T)s(t)$$

one obtains the infidelity minimum $s_0(t) \equiv -\operatorname{sgn}[b_t[0](T)]$. In fact, the above infidelity expansion can be interpreted as an effective classical energy $E(s) \equiv I_T[s]$ of the field s(t) in which $b_t[0](T)$ plays the role of an external field applied to the variable s(t). Since this is a non-interacting problem, energy is trivially minimized when s(t) has maximum absolute value and is anti-aligned with $b_t[0](T)$ [59]. In this way, in both the one- and two-qubit problems in Eq. (6) and (7), for $T \rightarrow 0$ we find the optimal protocol

$$s_0(t) \equiv \begin{cases} +1 & t < T/2 \\ -1 & t > T/2, \end{cases}$$
 (22)

B. Single-qubit problem

The starting point for our analysis is the protocol s_0 defined in Eq. (22). As a first step, we check its linear stability. In Fig. 4 we show the first order term $b_t[s_0](T)$ of the infidelity Taylor series centered at s_0 , for T=0.25 and $T=T_c$. In particular, we observe that s_0 is linearly stable for $T\in[0,T_c]$. Exactly at $T=T_c$, $b_t[s_0](T)$ (regarded as a function of the variable t) inverts its sign around the point t=T/2: s_0 has a linear instability for $T>T_c$ around the point t=T/2. In this way, we associate the T_c control landscape phase transition with linear instability of the protocol s_0 , optimal for $T\in[0,T_c]$.

Since the instability only affects a local neighborhood of t=T/2, it is suggestive to look for the new infidelity minimum in the region $T=T_c^+$ by locally (i.e., around t=T/2) modifying the previous optimal protocol $s_0(t)$.

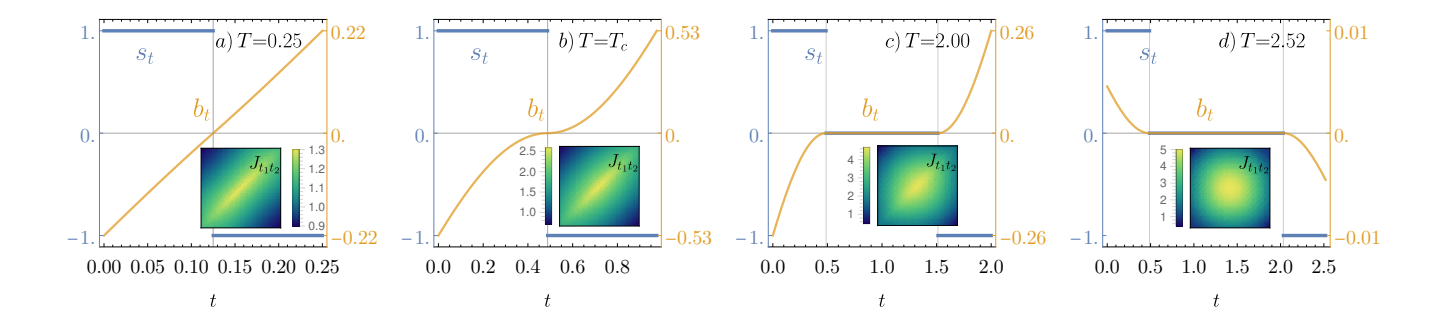


FIG. 4. Stability analysis in the single-qubit control problem. The plots show the linear $(b_t$, orange curve) and quadratic terms $(J_{t_1t_2}$, colormap insets) of the infidelity Taylor expansion centered around optimal piecewise-continuous protocols $(s_t, blue curve)$ found by the adiabatic tracing procedure (cf. Sec. IV), for different value of the duration T of the quantum evolution (CLPTs in $T_c \simeq 0.98$, $T_{\rm QSL} \simeq 2.51$). Linear term: b_t . For $T \in [0, T_c]$ the optimal protocol is s_0 in Eq. (22). (a) At T = 0.25, s_0 is anti-aligned with b_t and is linearly stable. (b) For $T = T_c$, s_0 becomes linearly unstable around t = T/2 as shown by the horizontal inflection of b_t around t = T/2. (c) For $T \in [T_c, T_{\rm QSL}]$ the optimal protocol is $s_{\Delta_0(T)}$ in Eq. (23). At T = 2.0, s_Δ is stable provided Δ is chosen as Eq. (23) (cf. Fig. 5a). (d) At $T = T_{\rm QSL}$, the first-order term is exactly zero and it flips sign for $T = T_{\rm QSL}^+$: $s_{\Delta_0(T)}$ becomes linearly unstable. Quadratic term: $J_{t_1t_2}$. In the language of statistical mechanics, the quadratic term represents the effective two-body interactions of the field s_t . In this case, interactions are antiferromagnetic (AFM) and long-range: the system is frustrated. For $T = T_c$ (panel (b)), the protocol s_0 becomes linearly unstable around t = T/2 and the local AFM interactions around the instability point dictate the new optimal protocol structure $s_{\Delta(T)}$ (cf. Eq. (23)).

For $T=T_c$, in the neighborhood of t=T/2, the first-order term $b_t[s_0](T)$ has a negligible contribution to the infidelity compared to the second-order term $J_{t_1t_2}[s_0](T)$. Moreover, using the language of statistical physics, we can interpret $J_{\frac{T_c}{2},\frac{T_c}{2}}[s_0](T_c)>0$ as an antiferromagnetic interaction (cf. $T=T_c$ case in Fig. 4b). This observation allows us to make an educated guess for the optimal protocol in the parameter region $T>T_c$:

$$s_{\Delta}(t) \equiv \begin{cases} 0 & t \in \left[\frac{T}{2} - \Delta, \frac{T}{2} + \Delta\right] \\ s_{0}(t) & \text{elsewhere,} \end{cases}$$
 (23)

where $\Delta \in [0, T/2]$ is a free parameter in the ansatz that may depend on the protocol duration T itself [60].

Past the critical point T_c , the family of protocols s_{Δ} parametrized by $\Delta \in [0, T/2]$, contains the optimal protocol. Searching for linearly stable protocols within the family s_{Δ} fixes Δ for each T. In fact, this constraint defines the curves $\Delta_0(T), \Delta_{\pm}(T)$, shown in Fig. 5a and selects the stable protocols among the family s_{Δ} . For $T \in [T_c, T_{\text{QSL}}]$, we find only one linearly stable protocol within this family. On the other hand, a bifurcation in the curve $\Delta(T)$ occurs which coincides exactly with the critical point at $T_{\text{QSL}} \simeq 2.51$, marking the end of the single-valued regime. More precisely, we find perfect agreement with the analytical behavior

$$\Delta(T) = \begin{cases} 0 & T \in [0, T_c] \\ \frac{1}{2}(T - T_c) & T \in [T_c, T_{QSL}] \\ \frac{1}{2}(T - T_c) + \delta_{\pm}(T) & T \gtrsim T_{QSL} \end{cases}$$
(24)

where $\delta_{\pm}(T) \sim \pm (T - T_{\rm QSL})^{1/2}$ as $T \rightarrow T_{\rm QSL}^+$. Hence, for later convenience, let us define

$$\Delta_0(T) = (T - T_c)/2, \quad \Delta_+(T) = \Delta_0(T) + \delta_+(T).$$
 (25)

The presence of the bifurcation at $T_{\rm QSL}$ implies that the infidelity landscape possesses two distinct linearly stable protocols $s_{\Delta_{\pm}}$. For $T{\geq}T_{\rm QSL}$ the infidelity associated with $s_{\Delta_{\pm}}$ vanishes (i.e. they are global optimal protocols) as it is visible in the inset of Fig. 5a. Consistent with the global optimality condition, we also find $b_t[s_{\Delta_{\pm}}](T){=}0$, $\forall t{\in}[0,T]$. Therefore, for $T{>}T_{\rm QSL}$ the infidelity landscape possesses at least two (and possibly more) globally optimal protocols $s_{\Delta_{\pm}}$. This indicates a non-trivial structure emerging in the near-optimal region in the control landscape.

A better understanding of the $T_{\rm QSL}$ control phase transition is provided by the quadratic stability analysis, and in particular by the eigenvalues of the Hessian operator. The results for the optimal protocol discussed so far $\{s_0, s_{\Delta_0}, s_{\Delta_\pm}\}$ are reported in Fig. 5b (see also App. C) and can be summarized as follows: (i) s_0 and s_{Δ_0} are quadratically stable in $[0, T_{\rm QSL}]$. (ii) For s_{Δ_0} , all except two eigenvalues of $J_{t_1t_2}[s_{\Delta_0}](T)$ change sign from positive to negative exactly at the quantum speed limit $T_{\rm QSL}$. (iii) For s_{Δ_\pm} , all except two eigenvalues of $J_{t_1t_2}[s_{\Delta_\pm}](T)$ vanish as $T \to T_{\rm QSL}^-$ and they remain zero for $T > T_{\rm QSL}$; the remaining two non-vanishing eigenvalues are positive. Thus, the control phase transition at $T_{\rm QSL}$ is associated with linear and quadratic instability.

It is interesting to notice that the presence of infinitely many zero eigenvalues is associated with infinitely many deformations of the protocols $s_{\Delta_{\pm}}$ preserving zero infidelity. This fact has important implications. First, we deduce that at $T_{\rm QSL}$ the number of optimal protocols may grow from one to infinite. Second, quadratic stability analysis relative to the optimal protocols $s_{\Delta_{\pm}}$ suggests the existence of an infinite-dimensional "optimal level set", defined implicitly by the equation $I_T[s]=0$, contain-

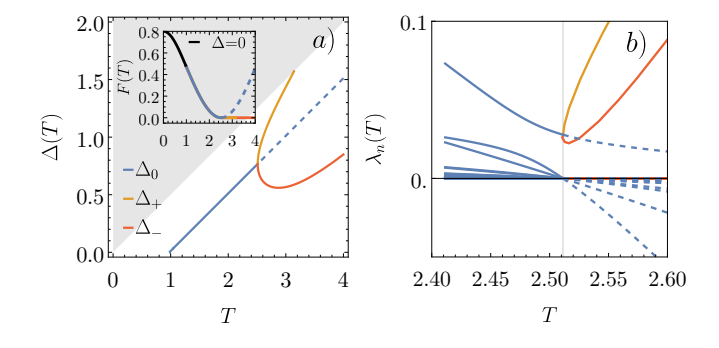


FIG. 5. Stability analysis in the single-qubit control problem. (a) Δ parametrizes the family of protocols s_{Δ} in Eq. (23). $\Delta(T)$ is defined by linear stability of the corresponding protocol. For $T \in [0, T_{QSL}], \Delta_0(T)$ is single-valued: within the family s_{Δ} there is a single optimal protocol. The bifurcation $\Delta(T) = \Delta_{\pm}(T)$ occurs at $T = T_{QSL}$ so that for $T > T_{QSL}$ $\Delta(T)$ is double-valued: within the family s_{Δ} there are two optimal protocols. The gray area corresponds to $\Delta > T/2$ and is inaccessible by definition. (b) Eigenvalues of the quadratic operator $J_{t_1t_2}$ from the infidelity Taylor expansion centered around the optimal protocol $s_{\Delta(T)}$. For $T \rightarrow T_{QSL}$, L-2 eigenvalues (blue solid curves) vanish: the protocol $s_{\Delta_0(T)}$ becomes quadratically unstable. The largest positive eigenvalue, approximately constant and with magnitude ~ 1 , is shown in App. C. For $T \ge T_{\text{QSL}}$, the two protocols $s_{\Delta_{+}(T)}$ are optimal $(I_T=0)$; the associated quadratic operator has L-2 vanishing and 2 positive eigenvalues. We deduce the existence of L-2orthogonal deformations of the optimal protocols $s_{\Delta_+(T)}$ that preserve the vanishing infidelity.

ing optimal and homotopically equivalent protocols; in this case, different optimal protocols (in the same connected component) could be continuously deformed into one another while preserving optimality. Such a property can be valuable in experimental applications: one can select a subset of optimal protocols based on desired criteria, such as robustness against experimental noise [29].

The local character of the linear and quadratic stability analysis does not allow for a direct study of the global properties of the optimal level set. Moreover, the constraint $|s(t)| \le 1$, ignored in this section, limits the allowed deformations around the two protocols $s_{\Delta_{\pm}}$, possibly preventing movements within the optimal level set. Hence, motivated by the quadratic stability analysis and acknowledging the limitations of our analytical approach, in Sec. V we investigate the existence of a level set of continuously connected optimal protocols using the Metropolis-adjusted Langevin dynamics.

C. Two-qubit problem

The two-qubit control problem follows the same qualitative behavior of the single-qubit case up to $T=T_{\rm sb}$. Following the same steps as in Sec. IV A, we correctly identify the optimal protocol s_0 for $T{\to}0$ and we detect,

by linear stability analysis, the critical point $T_c \simeq 1.57$. For $T \geq T_c$, only one protocol satisfies linear stability condition among the family (23) parametrized by $\Delta \in [0, T/2]$ (see Fig. 6).

The $T_{\rm sb}$ control phase transition presents new features. (i) As $T{\to}T_{\rm sb}$, $\Delta(T){\to}T/2$, so that $\Delta(T)$ reaches the boundary of its domain [0,T/2] and $s_{\Delta(T)}{\to}0$. (ii) For $T{=}T_{\rm sb}$, the linear-order term $b_t[s_{\Delta(T)}](T)$ vanishes: $s{=}0$ is a saddle point at $T{=}T_{\rm sb}$. (iii) For $T{=}T_{\rm sb}$, the lowest eigenvalue of the Hessian operator $J_{t_1t_2}[s_{\Delta(T)}](T)$ vanishes (cf. Fig. 6). These properties are reminiscent of the behavior of control phase transitions in the one-qubit problem $T_{\rm QSL}$, where the vanishing eigenvalues in the Hessian operator mark the presence of a branching phenomenon in the low-infidelity region of the landscape. However, for the two-qubit problem at $T{=}T_{\rm sb}$ there is only one vanishing eigenvalue.

In Ref. [41] the $T_{\rm sb}$ control phase transition was related to a bifurcation process. It was shown that the unique optimal protocol (valid in $T \le T_{\rm sb}$) bifurcates into two optimal protocols (valid in $T \ge T_{\rm sb}$) individually violating the symmetry $s(t) \leftrightarrow -s(T-t)$ of the quantum control problem. Interestingly, in the quadratic stability analysis the eigenfunction associated with the vanishing eigenvalue has even parity, namely it respects f(t)=f(T-t)(cf. Fig. 6). It is tempting to relate this latter property with the breaking of the quantum control symmetry occurring at $T=T_{\rm sb}$. In particular, one may try to guess the structure of the optimal protocol in the region $T \ge T_{\rm sb}$ by linearly combining the optimal protocol $s_{\Lambda(T)}$ in $T=T_{\rm sb}$ with the (symmetry-violating) eigenfunction associated to the quadratic instability in $T=T_{\rm sb}$, finally obtaining candidates as symmetry-violating optimal protocols. However, this procedure fails to reproduce the correct pair of optimal protocols for $T \ge T_{\rm sb}$. Therefore, in the two-qubit problem the adiabatic tracing of the optimal protocol of the landscape terminates at $T=T_{\rm sb}$.

For $T>T_{\rm sb}$, piecewise-continuous optimal protocols can be found using numerical optimization algorithms (for example, the LMC algorithm introduced in Sec. V). In App. C, we report the quadratic stability analysis at $T=T_{\rm QSL}$ for the two-qubit problem, where the infidelity is expanded around optimal protocols found by the LMC algorithm. The results are analogous to the single-qubit case, except that there are now L-4 vanishing eigenvalues, for $T\to T_{\rm QSL}$.

V. STOCHASTIC DYNAMICS WITHIN THE OPTIMAL LEVEL SET BEYOND THE QUANTUM SPEED LIMIT

In Sec. IV, the control phase transition occurring at $T_{\rm QSL}$ has been associated with the formation of infinitely many global minima in the quantum control landscape, branching out from isolated optimal protocols. Past $T_{\rm QSL}$, stability analysis suggests that the quantum control landscape possesses a level set of distinct protocols

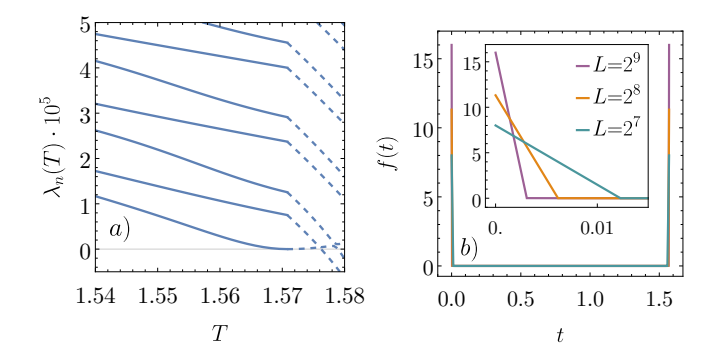


FIG. 6. Stability analysis in the two-qubit control problem. (a) Eigenvalues of the quadratic operator $J_{t_1t_2}$ from the infidelity Taylor expansion centered around the protocol $s_{\Delta(T)}$, optimal for $T \leq T_{\rm sb}$. In the plot, we discretize the [0,T] interval in L=64 steps; as L grows, the smallest eigenvalue decreases but remains positive for $T < T_{\rm sb} \simeq 1.57$. The CLPT in $T_{\rm sb}$ is associated with a single vanishing eigenvalue in the quadratic term. (b) Eigenfunction f(t) associated with the vanishing eigenvalue, plotted for $T \simeq T_{\rm sb}$. As L grows, f(t) approximates a sum of two delta distributions peaked at the interval boundary, t=0,T. Notice the even parity f(t)=f(T-t): this property is associated with the breaking of the symmetry of the quantum control problem, $s(t) \leftrightarrow -s(T-t)$, occurring at $T=T_{\rm sb}$.

satisfying I[s]=0 (i.e. "optimal") and that can be transformed into each other via continuous deformations. In this section, we introduce a simple stochastic dynamics algorithm to explore the low-infidelity region of the landscape and probe the properties of the optimal level set $\{s(t): I_T[s]=0\}$. Despite its simplicity, this approach can uncover important properties of the level set, such as connectivity, the local structure, and bulk size.

Let us introduce the algorithm we use to explore the optimal level set. First, we discretize the time domain [0,T] in L steps (t_1,\ldots,t_L) and approximate the piecewise-continuous protocol s(t) with a piecewise-constant protocol $\mathbf{s}=(s(t_1),\ldots,s(t_L))$ where $s(t_i)\in[-1,1]$. Then, we introduce a stochastic map $\mathbf{s}_n\mapsto\mathbf{s}_{n+1}$ by combining the gradient-free Langevin update rule,

$$s_{n+1}(t_i) = s_n(t_i) + \xi(t_i)$$

$$\langle \xi(t_i) \rangle = 0, \quad \langle \xi(t_i) \xi(t_i) \rangle = \sigma^2 \delta_{ij},$$
(26)

with the standard Metropolis acceptance rule,

$$P_{\text{acc}}(s(t_i)_{n+1}) = \min(1, \exp(-\beta L \Delta I_{n+1}))$$

$$\Delta I_{n+1} = I_T[s_{n+1}] - I_T[s_n].$$
(27)

Here, the subscript n labels the iteration of the stochastic dynamics, $\xi(t_i)$ is a Gaussian random variable of zero mean and variance σ^2 , and β has the intuitive meaning of (dimensionless) inverse-temperature. This dynamics is a gradient-free version of the standard Langevin-Monte Carlo algorithm (also known as Metropolis-adjusted Langevin algorithm [61]); we thus refer to this algorithm

as "LMC". The reasons behind such a simple algorithm are two-fold. On the one hand, we neglect the gradient term contribution (typically present in Langevin dynamics) because we use the algorithm to explore the optimal level set, characterized by a vanishing gradient term. On the other, we do not exploit information from the Hessian analysis in order to have an unbiased exploration algorithm.

LMC possesses two free parameters: $\beta, \sigma > 0$. In principle, they are independent of one another and need to be tuned carefully for the dynamics to explore efficiently the space of low-infidelity protocols. On one side, the dynamics is confined to a volume around the $I_T[s]=0$ hypersurface that shrinks as $\beta \to \infty$ and $\sigma \to 0$. On the other, as $\sigma \to 0$ the LMC dynamics slows down, and more time is needed for the optimal level set exploration. In what follows, we explore the optimal level set at $\beta=10^4, 10^5, 10^6$ and choose the value of σ maximizing the acceptance ratio for each β . In these cases, the LMC dynamics possesses three distinct stages:

- 1. Thermal relaxation stage: \mathbf{s}_n descends the infidelity landscape, from the initial random configuration to the low-infidelity region, reaching the bottom of one (of possibly many) landscape "valley" (Fig. 7a);
- 2. Diffusion stage: \mathbf{s}_n moves stochastically along the bottom of the valley since the Metropolis acceptance rule constrains the size of infidelity fluctuations $\Delta I \sim L\beta$ (Fig. 7b);
- 3. Equilibrium sampling stage: s_n explores the landscape valley and samples a statistically representative set of optimal protocols (Fig. 7c). This happens on a time scale that is much larger than that of the diffusion stage, and thus ensures that individual samples are uncorrelated.

Although the main motivation for the LMC algorithm is the study of the optimal level set, we find that the control phase transition at $T_{\rm QSL}$ affects each of the three stages. As a consequence, next we separately present the main results from the three stages of LMC dynamics.

A. Thermal relaxation stage

Upon initialization of the LMC algorithm, each component of the initial protocol \mathbf{s}_0 is drawn randomly from a uniform distribution in the interval [-1,1]. Subsequently, the stochastic dynamics evolves the protocol \mathbf{s}_n decreasing the corresponding infidelity $I[\mathbf{s}_n]$, thus "descending" the landscape. By studying how the infidelity changes as the protocol evolves from the initial random configuration, we obtain information about the structure of the quantum control landscape above the low-infidelity region.

For $\beta \gtrsim 10^3$ the behavior of the algorithm during thermal relaxation is largely independent of $\sigma \lesssim 10^{3/2}$. In

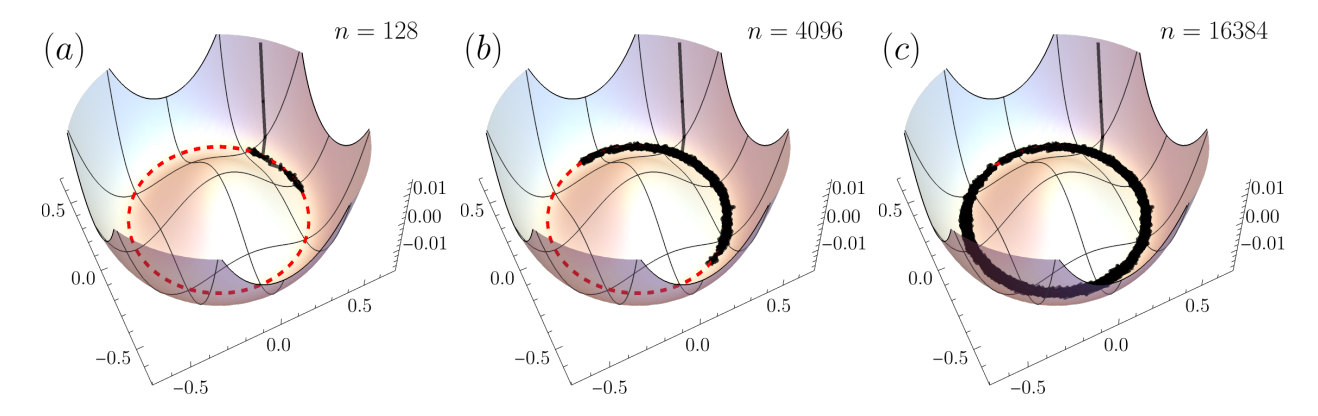


FIG. 7. Illustration of LMC dynamics in a two-dimensional toy-model system $\mathbf{s}_n = (x_n, y_n) \in \mathbb{R}^2$ subject to the landscape $V(\mathbf{s}_n) = -(1/8)x_n^2 + (1/4)x_n^4$, ("Mexican-hat") with $\beta = 10^4$, $\sigma = 10^{-3/2}$ (cf. Eq. (26)). The trajectory of \mathbf{s}_n in a single LMC run is plotted up to three different iterations. The stochastic motion along the optimal level set (the landscape valley denoted by the red-dashed curve) becomes visible. In general, LMC dynamics can be separated into three consecutive stages. (a) Thermal relaxation stage. The system \mathbf{s}_n starts from the random configuration \mathbf{s}_0 and reaches the region surrounding the optimal level set $I_T = 0$. (b) Diffusion stage. By stochastic moves, \mathbf{s}_n diffuses in the optimal level set; this motion cannot be suppressed by increasing β (provided the system has enough time to diffuse). (c) Equilibrium sampling stage. Asymptotically, \mathbf{s}_n explores the optimal level set. Using LMC dynamics, we sample different configurations from the optimal level set and study their statistical properties.

general, during this stage the non-equilibrium dynamics can be divided into two substages: one characterizes the motion at the beginning of thermal relaxation while the other appears subsequently and persists until the system thermalizes. Interestingly, the whole behavior can be captured by an effective one-dimensional model that admits a closed-form solution and provides a better intuition on the structural changes occurring in the landscape across the different control phase transitions (cf. App. D1). In particular, the CLPT affects the nonequilibrium dynamics in the thermal relaxation stage of LMC and one may then detect the presence of the CLPT without sampling optimal protocols. We remark that so far CLPTs have been characterized exclusively in terms of statistical properties of the locally optimal protocols, whereas here we provide a dynamical characterization.

B. Diffusion stage

Once the protocol \mathbf{s}_n reaches the bottom of a valley in the infidelity landscape, it moves stochastically along the flat directions of the landscape. If the infidelity minimum is unique (or the infidelity minima are isolated from each other), fluctuations of \mathbf{s}_n are suppressed by the effective inverse temperature β , cf. Eq. (27). Otherwise, if different infidelity minima are continuously connected with each other, protocol fluctuations within the flat directions are not suppressed by taking $\beta \rightarrow \infty$. Therefore, if the T_{QSL} control phase transition is associated with the creation of infinitely many flat directions in the infidelity valley, then the LMC dynamics after thermal relaxation should be strongly affected by this control phase transition.

For a quantitative description, it is useful to fix the parameter β (in the Metropolis acceptance rule) and vary the size of the stochastic jumps $\sigma \ll \sqrt{\beta}$. In this limit, we approximate the LMC dynamics with an L-dimensional diffusive motion subject to a constraining potential given by the infidelity. For short times, LMC explores the neighborhood of the initial point, and its motion can be decomposed in an approximately free motion along the valley (the tangent space) and fluctuations along the orthogonal directions (cf. Fig. 7b). At long times the LMC dynamics diffuses around the optimal level set, ideally exploring this set in a relatively dense way (*i.e.* such that the mean values of the observables we sample using LMC dynamics converge to constant values).

In more concrete terms, during the diffusive stage, we consider the covariance matrix related to the protocol fluctuations \mathbf{s}_n . Using this quantity, for each β we estimate the minimum time required to diffuse through the optimal level set (cf. App. D 2). In addition, eigenvalues and eigenvectors of the covariance matrix can be used to study the local structure (during early-diffusion time) or the bulk size (for asymptotic diffusion time) of the optimal level set.

C. Equilibrium sampling stage

Ultimately, the $T_{\rm QSL}$ control phase transition affects the statistical properties of protocols lying in the low-infidelity region of the landscape. Accordingly, we primarily use LMC to sample protocols continuously connected with each other through sufficiently small stochastic jumps, cf. Eq. (26). In particular, we use LMC's diffusive motion to move along the infidelity valleys and

store the protocol configuration \mathbf{s}_n every $\Delta n = 2^{14}$ iterations (see App. D 2) such that, between two samples, LMC explores a global portion of the optimal level set. For each set of LMC parameters, we collect R LMC runs acquiring M optimal protocols each. Notice that, in each run, LMC starts from a different random protocol \mathbf{s}_0 and the system first relaxes to the global optimal level set before the sampling of the M optimal protocols begins.

As a first observable, consider the order parameter q(T) defined in Eq. (4) which measures the size of fluctuations around the mean protocol (the average $\langle \cdot \rangle$ is here performed over each LMC run separately). The existence of an optimal level set composed of isolated points is related to a vanishing q(T) in the limit $\beta \to \infty$. In Fig. 8 we show q(T) for different values of the inverse-temperature β and the system size L, for the single- and two-qubit problems. In the single-qubit case, as β grows we find $q(T) \rightarrow 0$ for $T \in [0, T_{QSL}]$: this confirms that for $T < T_{QSL}$ the infidelity minimum is unique for piecewise-constant protocols. By contrast, for $T > T_{QSL}$ the minimum is not unique since q(T) is independent of β . Remarkably, the scaling analysis with L reveals the $T_{\rm OSL}$ transition as a first-order transition: namely, q(T) has a jump discontinuity in $T=T_{QSL}$. In the two-qubit case, similarly we find $q(T) \rightarrow 0$ (as β is increased) for $T \in [0, T_{QSL}]$. Notice that this does not contradict the presence of two isolated optimal protocols in the interval $[T_{\rm sb}, T_{\rm QSL}]$: each LMC run is confined to one of the two valleys which are not continuously connected to each other. Therefore, the protocol fluctuations still depend on the inverse-temperature β . For $T=T_{\mathrm{QSL}},\ q(T)$ acquires a finite value with a jumpdiscontinuity (as in the single-qubit case). Interestingly, for $T \gtrsim 3.3$ in the two-qubit case the presence of multiple connected components in the optimal level set gives rise to a larger standard deviation of the mean value q(T) for the same number of LMC samples (error-bar in Fig. 8c,d)

The number of connected components in the optimal level set can be estimated by computing the distance between pairs of LMC runs. The M protocols sampled within each LMC run are connected with each other by the LMC dynamics (see, e.g., Fig. 7 for a schematic cartoon). Assuming that LMC approximates homotopic transformations between optimal protocols, we regard the M protocols collected during each LMC run as continuously connected to one another. On the contrary, protocols in different runs may belong to different connected components of the optimal level set since LMC thermalizes to different protocols in different runs. Therefore, by computing the distance between pairs of protocols belonging to different LMC runs, we can estimate the number of connected components in the optimal level set. In Fig. 9 we show a schematic representation of the idea behind the distance analysis, involving protocols within and across runs and we discuss details in App. D3. In the single-qubit control landscape, our results suggest the presence of a single connected component for all $T \in [T_{QSL}, 3.5]$: as the number of protocols per

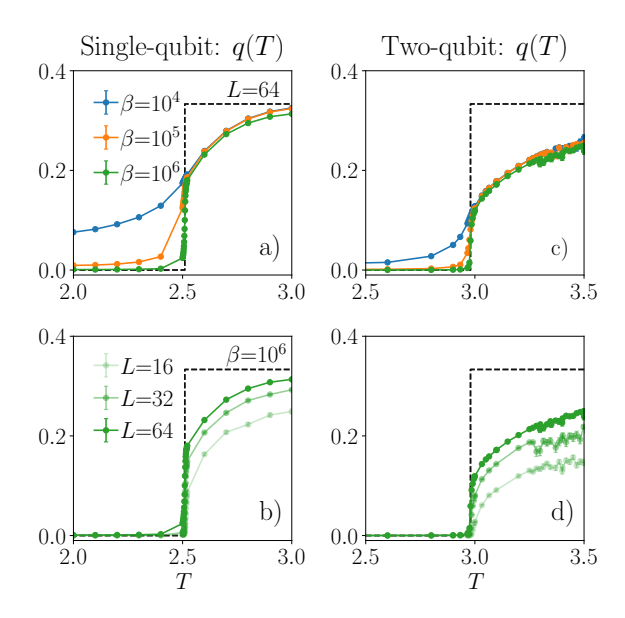


FIG. 8. Single- and two-qubit control problems. Jump-discontinuity of the order parameter q(T) in Eq. (4) at the quantum speed limit; q(T) quantifies fluctuations of the piecewise-continuous protocol as it explores the optimal level set under LMC dynamics. A non-vanishing value of q(T) (as $\beta \rightarrow \infty$) implies that the optimal level set possesses a family of optimal protocols connected to each other via continuous transformations (homotopy). The black dashed curve shows the analytical prediction discussed in Sec. VIB. In the two-qubit case, the errors associated with the mean value of q(T) are relatively small for $T \lesssim 3.3$ but they show a sudden increase for $T \gtrsim 3.3$ for the same number of LMC steps. As discussed in Ref. [62], this is related to the presence of a new disconnected component in the optimal level set arising at $T \simeq 3.3$.

run is increased, the distance steadily decreases to zero following an algebraic decay. In the two-qubit problem, the situation is more complex and is discussed in detail in Ref. [62].

VI. CRITICAL BEHAVIOR AT THE QUANTUM SPEED LIMIT

In Sec. V, we presented numerical evidence supporting the relation between the control landscape phase transition at $T=T_{\rm QSL}$ and the formation of an infinite dimensional optimal level set lying in the zero-infidelity hyperplane. So far this analysis was purely numerical, and little intuition about the general structure of this infinite-dimensional manifold was given. In this section, we complement the numerical study, limited by construction to finite-size $(L<\infty)$ systems, with an analytical characterization of the optimal level set and the associated $T_{\rm QSL}$ transition. In particular, we shed new light on the nature of the non-analytic points in the order parameters $q_{\rm BB}(T)$, q(T) visible in Figs. 2 and 8. Eventually, we

Protocol space

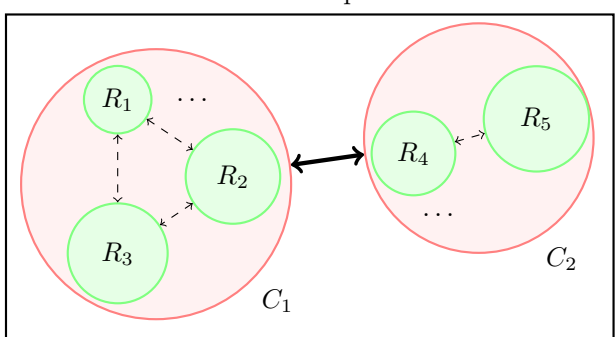


FIG. 9. Schematic visualization of different sets of protocols R_1, R_2, \ldots sampled by independent LMC runs. As $\beta \to \infty$, stochastic jumps between different connected components of the optimal level set, represented by the red sets C_1, C_2 , become ever more unlikely during LMC dynamics. In this limit, the sets R_1, R_2, \ldots are confined in either one of the two components. The distance between two sets, defined in Eq. (D6) and represented by the arrows in the figure, can vanish, as the number of sampled sets increases, only when the two sets are located in the same connected component. Whenever two sets are located in different connected components, the distance reaches asymptotically (in LMC iterations) a non-vanishing value.

explicitly discuss the analytical prediction for the singlequbit problem, where the optimal protocol for $T \leq T_{\text{QSL}}$, $s_{\Delta_0(T)}$, is known exactly.

In general, the following analysis can be applied whenever one is able to "follow", as T is increased, an isolated locally-optimal protocol as its infidelity vanishes (more generally, when the cost-function reaches its minimum value). In this situation, one may center the infidelity expansion around the locally-optimal protocol and consider its coefficients as functions of T.

A. Partition function

The order parameters $q(T), q_{\rm BB}(T)$, introduced in Eqs. (4) and (5), capture statistical properties of local minima in the quantum control landscape; in particular, q(T) and $q_{\rm BB}(T)$ can be explicitly evaluated once a method to compute the expectation values $\langle s(t) \rangle$ and $\langle s(t)^2 \rangle$ is introduced.

Previously, we relied on two different numerical algorithms, SD and LMC, capable of sampling protocols from the low-infidelity region by following the prescribed dynamics: in this way, expectation values are computed as average over the set of sampled states. Now, as a first step towards an analytical approach, we shall specify a rule for the computation of the expectation values in Eqs. (4) and (5).

In general, the expectation values can be analytically evaluated only once a set of states \mathcal{X} together with an associated set of weights w(x), $x \in \mathcal{X}$ are introduced. The

expectation value of a generic observable $f: \mathcal{X} \to \mathbb{R}$ is then computed as the ratio

$$\langle f \rangle_{\mathcal{X}} = \frac{\sum_{x \in \mathcal{X}} [f(x)w(x)]}{\sum_{x \in \mathcal{X}} [w(x)]},$$

where the explicit sum evaluation depends on the nature of the set \mathcal{X} . Introducing the partition function $Z[f] = \sum_{x \in \mathcal{X}} \{f(x)w(x)\}$ we can compactly write $\langle f \rangle_{\mathcal{X}} = Z[f]/Z[1]$. In our problem, \mathcal{X} is the infinite-dimensional space of bounded protocols $\{s(t): |s(t)| \leq 1\}$ and the trace is a functional integration (path integral) formally written as

$$Z[f] = \int_{-1}^{+1} \prod_{t} ds_t f[s] w[s].$$

Since we are interested in the order parameters $q(T), q_{BB}(T)$ and because they are related to a structural change of the low-infidelity region, it is reasonable to choose the Boltzmann-Gibbs weights $w[s] = \exp(-\beta I[s])$, with $I[s]=I_T[s]$ the infidelity and β free parameter [63]. In this way, as $\beta \rightarrow \infty$, the dominant contributions to the partition function have the lowest possible infidelity. More explicitly, as $\beta \to \infty$ the weights $w_{\beta}[s]$ reduce to delta functions $\delta(I[s] - \min_s I[s])$ restricting the path integral to those protocols with the smallest infidelity. Although this is a valid approximation for a finite system size, one must be careful when taking the limit $N, \beta \rightarrow \infty$ as the degeneracy of the excited states may be large enough to contribute to the partition function. A simple example of this is the classical Ising chain, where the degeneracy of domain walls reduces the critical temperature to zero in the $N \rightarrow \infty$ limit.

As a specific example, we consider the single-qubit quantum control problem defined in Eq. (6). As we saw in Sec. (IV), for $T \le T_{\text{QSL}}$ the problem admits only one optimal protocol which we called $s_{\Delta_0(T)}$, cf. Eq. (23). Then, in the limit $\beta \to \infty$, the partition function reduces to

$$Z[f] = f[s_{\Delta_0(T)}], \qquad T \le T_{\text{QSL}}. \tag{28}$$

Using Eqs. (5),(25) we obtain for $T \leq T_{QSL}$,

$$q(T) = 0 (29)$$

$$q_{\rm BB}(T) = 1 - \frac{1}{T} \int_0^T dt \, s_{\Delta_0(T)}(t)^2$$

$$= \max(0, 1 - (T - 2\Delta_0(T))/T)$$

$$= \max(0, 1 - T_c/T) \equiv q_{\rm BB,0}(T), \qquad (30)$$

where the last equality follows from Eqs. (23) and (24). In Figs. 8, 10 we see that the two results agree with LMC and SD simulations, respectively.

For $T>T_{\rm QSL}$, the optimal level set contains infinitely many protocols with vanishing infidelity. In this case, the partition function is

$$Z[f] = \int_{-1}^{+1} \prod_{t} ds_t f[s] \delta(I[s]), \qquad T > T_{QSL}.$$
 (31)

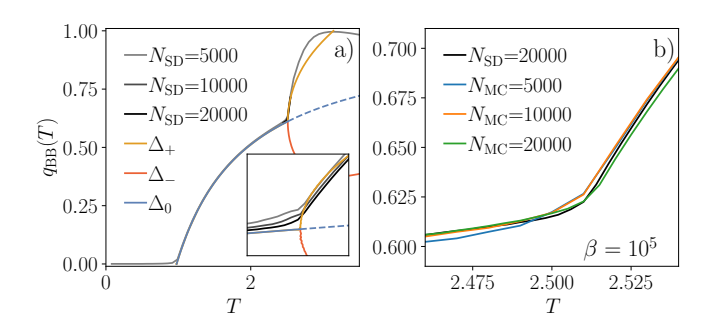


FIG. 10. Single qubit-problem. (a) $q_{BB}(T)$ curves obtained from SD and adiabatic tracing (cf. Secs. I and IV, respectively). By increasing the number of bang-bang steps N, we observe that SD's $q_{BB}(T)$ curve exhibits a linear critical scaling for $T \rightarrow T_{\text{QSL}}^+$ (black curves). On the contrary, $q_{\rm BB}(T)$ curves obtained from adiabatic tracing (orange and red curves) do not possess a linear critical scaling. (b) Comparison between $q_{\rm BB}(T)$ curves obtained from SD and Monte Carlo simulations with acceptance probability $p = \exp(-\beta N_{\text{MC}} \Delta I)$ of a single-site spin-flip $s_i \mapsto -s_i$ (ΔI : infidelity increment after spin-flip). The plot shows good agreement between the two distinct numerical algorithms, suggesting that the linear critical scaling observed for $T \rightarrow T_{QSL}^+$ is independent of the specific numerical dynamics.

In the next sections, we will explicitly evaluate the path integral in the partition function to extract an analytical estimate of q(T) and $q_{BB}(T)$ for $T > T_{QSL}$.

Optimal level set parametrization

The single-qubit problem possesses an isolated optimal protocol for $T \leq T_{QSL}$, $s_{\Delta_0(T)}$. Since we are interested in the critical behavior of the order parameters q(T) and $q_{\rm BB}(T)$ as $T \rightarrow T_{\rm QSL}^+$, we use the infidelity expansion centered around $s_{\Delta_0(T)}$ to obtain a convenient parametrization of the optimal level set.

The infidelity expansions around $s_{\Delta_0(T)}$ reads

$$I_T[\delta s] = c + \int dt \, b_t \delta s_t + \frac{1}{2} \int d^2t \, J_{t_1 t_2} \delta s_{t_1} \delta s_{t_2} + \dots$$

where δs_t represents deviations from the protocol $s_{\Delta_0(T)}$. Notice that we omit the T and $s_{\Delta_0(T)}$ dependence in the expansion coefficients $c, b_t, J_{t_1t_2}$ for simplicity.

Then, we expand δs_t in the eigenbasis $\{f_t^{(n)}\}_n$ of the Hessian operator $J_{t_1t_2}$ as

$$\delta s_t = \sum_{n=1}^{\infty} x_n f_t^{(n)}$$

where x_n are the new degrees of freedom. Using the orthonormality of the eigenbasis, $\int_0^T f_t^{(n)} f_t^{(m)} dt/T = \delta_{nm}$,

we obtain

$$I_T[x] = c + T \sum_{n=1}^{\infty} b_n x_n + \frac{T^2}{2} \sum_{n=1}^{\infty} \lambda_n x_n^2 + \dots$$

where $\{\lambda_n\}$ are the eigenvalues of $J_{t_1t_2}$ and we defined

 $b_n = \int_0^T \mathrm{d}t \, f_t^{(n)} b_t / T.$ In Sec. IV we expanded the infidelity around the isolated optimal protocols for $T \leq T_{QSL}$. We found that, for $T=T_{\rm QSL}$, all except n_+ eigenvalues of the second order term, denoted $\{\lambda_n\}$, vanish. The positive integer n_+ depends on the quantum system; for example, in the single-qubit and two-qubit case we introduce in Sec. II we have $n_{+}=2$ and $n_{+}=4$, respectively. Hence, assuming $\lambda_{n < n_+}(T_{\text{QSL}}) > 0$ and $\lambda_{n > n_+}(T_{\text{QSL}}) = 0$, $\lambda_n(T)$ as functions of T have the generic critical scaling

$$\lambda_{n < n_{+}} \sim \text{const}$$
 $\lambda_{n > n_{+}} \sim (T - T_{\text{QSL}}).$ (32)

Now, let us define $\tilde{b}_n = Tb_n$ and $\tilde{\lambda}_n = T^2\lambda_n$ and notice that, in the limit $T \rightarrow T_{\text{QSL}}$, b_n , λ_n have the same critical scaling as b_n, λ_n , respectively. Hence, in the remaining part of this section (as well as in Apps. F, G and H) we drop the "~" symbol for notational convenience.

We can compute an approximate parametrization of the optimal level set by truncating the infidelity expansion to second order: the intersection between the truncated infidelity expansion and the zero-infidelity hyperplane $I_T[s]=0$ reads, after completing the squares:

$$I_T[x] = I + \frac{1}{2} \sum_{n=1}^{\infty} \lambda_n (x_{1n} + x_n)^2 = 0,$$
 (33)

where we define I and x_{1n} as

$$I = c - \frac{1}{2} \sum_{n=0}^{\infty} \frac{b_n}{\lambda_n}, \qquad x_{1n} = \frac{b_n}{\lambda_n}. \tag{34}$$

This equation gives the lowest order approximation for the optimal level set when expanding infidelity around the protocol $s_{\Delta_0(T)}$. Higher-order terms in the infidelity expansion provide corrections to the above result.

In App. E we test the optimal level set parametrization truncated at second order against the exact infidelity landscape in the single-qubit case. In particular, the approximate parametrization is in good quantitative agreement with the exact infidelity when considering deformations x_n with n even (associated to odd parity eigenfunctions $f^{(n)}$). For odd n (associated to even parity eigenfunctions $f^{(n)}$) and in the limit $T \rightarrow T_{QSL}$, the approximate parametrization cannot replicate the behavior observed in the exact landscape: we deduce that, for odd n, higher-order terms contributions to the optimal level set parametrization are comparable with secondorder ones. Nevertheless, we notice that the mismatch is a direct consequence of the (odd parity) symmetry of the quantum control problems we consider: as T is increased, the quantitative agreement between the approximated

parametrization and the exact landscape improves, for even and odd n.

Notice that the structure of the parametrization of the optimal level set in Eq. (33) does not depend on the controlled system associated with the control problem. Moreover, even though the quantities $c, b_n, \lambda_n, \ldots$ depend on the specific quantum system of interest, we expect to observe similar features in generic control problems when expanding the infidelity around isolated suboptimal protocol(s) that reach global optimality (vanishing infidelity) as T is increased. Namely, in this circumstances, we expect (i) a vanishing constant term c(T), (ii) the linear term $b_n(T)$ to be identically zero, and (iii) the spectrum $\{\lambda_n\}$ of the quadratic term $J_{t_1t_2}$ to possess an infinite number of vanishing eigenvalues. These properties are a consequence of the infidelity being bounded in the interval [0, 1].

The results of this section depend on the peculiar behavior of the spectrum of the quadratic-order term of the expansion near the Quantum Speed Limit transition: eigenvalues $\{\lambda_n\}$ divides into a subset that remains positive and a subset that vanishes and change sign. More precisely, the outcome of the following calculation depends on the number of sign-changing eigenvalues and the critical scaling of the terms $c(T), b_n(T), \lambda_n(T), \ldots$ in the infidelity expansion, regarded as functions of $(T-T_{\rm QSL})$.

2. Hard-boundary constraint approximation

The hard-boundary constraint $|s(t)| \le 1$ imposed on the protocol space amounts to a restriction of the integration domain for each coordinate s_t . Unfortunately, this constraint does not allow for an explicit evaluation of the partition function so we need a suitable approximation.

As a first step, we rewrite the constraint as

$$\begin{split} \int_{-1}^{1} \mathrm{d}s_t &= \int_{-1}^{1} \mathrm{d}\lambda_t \int_{\mathbb{R}} \mathrm{d}s_t \delta(s_t - \lambda_t) \\ &= \int_{-1}^{1} \mathrm{d}\lambda_t \int_{\mathbb{R}} \mathrm{d}s_t \int_{\mathbb{R}} \frac{\mathrm{d}\nu_t}{2\pi} \, e^{i\nu_t(s_t - \lambda_t)}, \end{split}$$

where we introduced the Fourier representation of the Dirac-delta distribution $\delta(s_t - \lambda_t)$. Integrating over λ_t gives

$$\begin{split} \int_{-1}^{1} \mathrm{d}\lambda_{t} \, e^{i\nu_{t}(s_{t} - \lambda_{t})} &= e^{i\nu_{t}s_{t}} \, 2\frac{\sin(\nu_{t})}{\nu_{t}} = 2e^{i\nu_{t}s_{t} + \log(\sin\nu_{t}/\nu_{t})} \\ &\approx 2e^{i\nu_{t}s_{t} - \nu_{t}^{2}/6} \end{split}$$

where, in the last line, we expanded the exponent at second-order in ν_t ; effectively, we trade the $\sin(x)/x$ function for a Gaussian displaying the same behavior for $\nu_t \to 0$ (notice that both functions are peaked around $\nu_t = 0$ and vanish for $|\nu_t| \to \infty$). Last, integration over ν_t gives

$$\int_{\mathbb{R}} \frac{\mathrm{d}\nu_t}{2\pi} \, 2e^{i\nu_t s_t - \nu_t^2/6} \approx e^{-(3/2)s_t^2},$$

where the proportionality factor is not essential for the partition function evaluation. In conclusion, we obtain

$$\int_{-1}^{1} \mathrm{d}s_t \approx \int_{\mathbb{R}} \mathrm{d}s_t \, e^{-(3/2)s_t^2}.$$

Notice that, while relaxing the optimal level set restriction, the Gaussian approximation of the hard-boundary constraint does not affect the first two moments $\langle s_t \rangle$, $\langle s_t^2 \rangle$. Namely,

$$\frac{\int_{-1}^{+1} ds_t s_t}{\int_{-1}^{+1} ds_t} = \frac{\int_{\mathbb{R}} ds_t e^{-(3/2)s_t^2} s_t}{\int_{\mathbb{R}} ds_t e^{-(3/2)s_t^2}} = 0$$

$$\frac{\int_{-1}^{+1} ds_t s_t^2}{\int_{-1}^{+1} ds_t} = \frac{\int_{\mathbb{R}} ds_t e^{-(3/2)s_t^2} s_t^2}{\int_{\mathbb{R}} ds_t e^{-(3/2)s_t^2}} = \frac{1}{3}.$$
(35)

However, higher moments will differ as the two distributions are distinct.

B. Relation between q(T) and the partition function

Over the space of continuous protocols, the order parameter q(T), defined in Eq. (4), reads as

$$q(T) = \frac{1}{T} \int_0^T dt \left(\left\langle s_t^2 \right\rangle - \left\langle s_t \right\rangle^2 \right). \tag{36}$$

Neglecting the vanishing infidelity constraint in the partition function (31), we obtain from Eq. (35)

$$q(T) = 1/3. (37)$$

This result represents the highest possible value for q(T), achieved when the protocol space is only subject to $|s(t)| \le 1$. Additional constraints (such as vanishing infidelity) can only decrease this result.

As we saw in Eq. (33), the parametrization of the optimal level set $I_T[s]=0$ is conveniently written in terms of the Hessian eigenbasis $\{f^{(n)}\}$. In this basis, the order parameter becomes

$$q(T) = \sum_{n=1}^{\infty} \left(\left\langle x_n^2 \right\rangle - \left\langle x_n \right\rangle^2 \right). \tag{38}$$

In the finite-dimensional case, we have

$$q(T) = \sum_{n=1}^{L} \left(\left\langle x_n^2 \right\rangle - \left\langle x_n \right\rangle^2 \right). \tag{39}$$

Thus, to estimate q(T) it is necessary to compute $\langle x_n \rangle = Z[x_n]/Z[1]$ and $\langle x_n^2 \rangle = Z[x_n^2]/Z[1]$.

Considering the approximations introduced in the last two sections, the exact partition function in Eq. (31) is

now replaced by

$$Z[f] = \int_{\mathbb{R}} \prod_{t} ds_{t} e^{-(3/2)(L/T) \int_{0}^{T} dt s_{t}^{2}} \delta(I_{T}[s]) f[s]$$
$$= \int_{\mathbb{R}} \prod_{n} dx_{n} e^{-(3/2)L \sum_{n} (x_{0n} + x_{n})^{2}} \delta(I_{T}[x]) f[x]$$

where the effective "system size" L represents the dimensional cutoff in the path integral: namely, $\prod_t \equiv \prod_{t=1}^L$ and $\prod_n \equiv \prod_{n=1}^L$. Notice that the last line was obtained through the change of variables,

$$s_t = s_{\Delta_0, t} + \delta s_t = \sum_{n=1}^{L} (x_{0n} + x_n) f_t^{(n)}$$

where $s_{\Delta_0,t}$ is the unique optimal protocol for $T=T_{\text{QSL}}$ in the single-qubit problem (cf. Sec. IV) and $\{x_{0n}\}$ are defined by

$$s_{\Delta_0,t} = \sum_{n=1}^{L} x_{0n} f_t^{(n)}.$$
 (40)

In what follows, we use the Fourier representation of the Dirac-delta distribution,

$$\delta(I_T[s]) = \int_{\mathbb{R}} \frac{\mathrm{d}\mu}{2\pi} e^{i\mu I_T[s]} \tag{41}$$

with $I_T[s]$ given explicitly by Eq. (33) (quadratic-order approximation).

1. Computing q(T)

The moments $\langle x_n^{\alpha} \rangle$, $\alpha \in \mathbb{N}$ are conveniently computed from the generating functional

$$G[k] = Z[e^{\sum_{n} k_n x_n}] \tag{42}$$

via $\partial_{k_n}^{\alpha}G[k]\big|_{k=0}/G[0]=\langle x_n^{\alpha}\rangle$. More explicitly, we need to evaluate the following quantity

$$G[k] = \int_{\mathbb{R}} \prod_{n} dx_n \int_{\mathbb{R}} \frac{d\mu}{2\pi} \exp\left[-L\frac{\kappa}{2} \sum_{n} (x_{0n} + x_n)^2 + i\mu \left(I + \frac{1}{2} \sum_{n} \lambda_n (x_{1n} + x_n)^2\right) + \sum_{n} k_n x_n\right]$$
(43)

where we introduced the parameter $\kappa \in (0, \infty)$ for later convenience (cf. Sec. VI C). After the change of variables $y_n = x_n + x_{1n}$ and $z = \mu/(\kappa L)$, we integrate over $\{y_n\}$ to obtain [64]

$$G[k] = e^{-\sum k_n x_{1n}} \int_{\mathbb{R}} dz \frac{\exp[L\Omega(z)]}{\prod_n \sqrt{1 - iz\lambda_n}}$$
(44)

$$\Omega(z) = \kappa \left(iIz + \frac{1}{2} \sum_{n} \frac{\Delta x_n(k_n)^2}{1 - iz\lambda_n} \right)$$
 (45)

$$\Delta x_n(k_n) = x_{0n} - x_{1n} - k_n/(\kappa L). \tag{46}$$

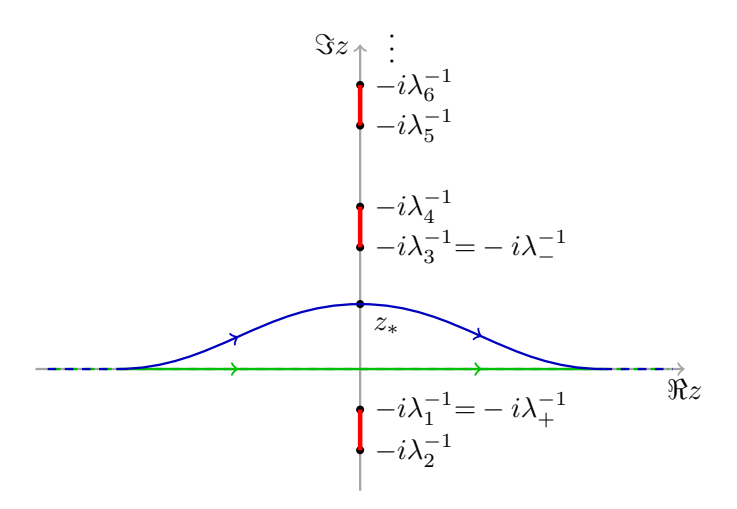


FIG. 11. Schematic representation in the complex plane $z \in \mathbb{C}$ of the simple poles $\{-i\lambda_n^{-1}\}$ and the saddle-point z_* of the complex function $\Omega(z)$ defined in Eq. (45). $\Omega(z)$ appears in the calculation of the generating functional G[k] (cf. Eq. (44)). The spectrum $\{\lambda_n\}$ of the quadratic-order term in the infidelity expansion determines the poles' location. As in the single-qubit problem, here we consider $\lambda_{1,2} > 0$, $\lambda_{n>2} < 0$. The green path represents the initial integration path along the real axis appearing in G[k]. We perform a steepest-descent approximation by deforming the green into the blue path passing through the saddle-point z_* of $\Omega(z)$ in the direction of steepest descent. The red segments represent branch cuts created by the square root appearing in the integrand in Eq. (44).

In the $L\to\infty$ limit, the integral is dominated by saddlepoints z_* of the exponent $\Omega(z)$ satisfying $\partial_z \Omega(z_*) = 0$. For $z \in \mathbb{R}$ the exponent is a complex number so that valid saddle-points must satisfy additional conditions (cf. App. F). Although there is no valid saddle point for $z \in \mathbb{R}$, following the steepest-descent method we deform the integration contour in the complex plane and intersect a complex-valued saddle-point $z_* \in \mathbb{C}$; the deformation is valid provided we do not cross any branch points during the process [65]. Notice that each positive (negative) eigenvalue λ_n corresponds to a branch point (and an essential singularity) located on the lower (upper) imaginary semi-axis, $z=-i\lambda_n^{-1}$. In App. F we show that a saddle point z_* satisfying the required properties can always be found lying on the imaginary axis within the interval

$$\operatorname{Re}(z_*) = 0, \quad \operatorname{Im}(z_*) \in (-i\lambda_{\perp}^{-1}, -i\lambda_{\perp}^{-1})$$
 (47)

for $T \rightarrow T_{\mathrm{QSL}}^+$, where $\lambda_{+/-}^{-1}$ are the positive/negative eigenvalues among $\{\lambda_n\}$ with largest modulus (cf. Fig. 11). Consequently, in the $L \rightarrow \infty$ limit we replace the integration over z with its saddle-point value; the cumulant-generating functional then reads [66]

$$\log G[k] = L\Omega(z_*) - \sum_n k_n x_{1n}$$
(48)

where $z_*=z_*[k]$ is the solution of the saddle-point equation

$$0 = I + \frac{\kappa}{2} \sum_{n} \frac{\Delta x_n(k_n)^2 \lambda_n}{(1 - i\lambda_n z)^2}.$$
 (49)

Ultimately, after repeated differentiation, we arrive at (see App. G)

$$q(T_{\text{QSL}}^{+}) \sim (1/\kappa) \left(\frac{1}{L} \sum_{n=1}^{L} r_0(-i\lambda_n z_*)\right)$$
 (50)

$$r_0(x) = \frac{1+x}{1+x^2}. (51)$$

As a specific example we consider the single-qubit problem of Sec. II. In this case, from the condition (47) and the scaling $\lambda_n \sim n^{-2}$ (cf. App. C), we deduce $-i\lambda_n z_* \rightarrow 0$ as $n \rightarrow \infty$. Consequently, within the quadratic infidelity expansion and in the limit $L\rightarrow\infty$ we obtain $q(T_{\text{OSL}}^+) \rightarrow 1/3$ (after substitution $\kappa=3$). Surprisingly, the optimal level set restriction to the protocol space has no effect on the order parameter q(T): the result converges to the value in Eq. (37) obtained while neglecting the optimal level set restriction. The reason behind this result can be understood as follows. In the $L\to\infty$ limit, the degrees of freedom $\{x_n\}$ associated with large n are unconstrained by the quadratic-order expansion of the infidelity as their prefactors $\{\lambda_n\}$ vanish for $n\to\infty$; hence, $\{x_n\}$ are effectively subject only to the hard-boundary constraint, $|s(t)| \le 1$, for large n.

In App. E we show that the quadratic-order approximation of the infidelity expansion does not completely agree with the exact landscape, for large-n degrees of freedom $\{x_n\}$, in the single-qubit problem. The mismatch is important for directions n associated with evenparity eigenfunctions $f^{(n)}(t)=f^{(n)}(T-t)$, as $T\to T_{\rm QSL}$: for these degrees of freedom, the quadratic-order contribution in the infidelity expansion is negligible with respect to higher-orders (this is related with the control problem symmetry $s(t)\leftrightarrow -s(T-t)$, cf. Sec. II). As a consequence, a first step towards improving the analytical prediction in Eq. (50) is achieved by considering perturbative corrections of higher-order terms in the infidelity expansion (33) (in particular, quartic-order terms).

Interestingly, we may already use numerical evidence from App. $\bf E$ to guess the effects of higher-order corrections on the analytical prediction for q(T). In short, we deduce that higher-order terms in the infidelity expansion suppress protocol fluctuations along even-parity eigenfunctions f(t)=f(T-t), for $T\to T_{\rm QSL}$. On the contrary, the quadratic-order expansion of infidelity does not distinguish between even- and odd-parity eigenfunctions. Therefore, in the $L\to\infty$ limit higher-order terms eliminate exactly half of the directions available for fluctuations within the quadratic approximation. Consequently, including higher-order terms in the infidelity expansion is expected to yield $q(T_{\rm QSL}^+)\to (1/3)/2\simeq 0.17$. This result is in good quantitative agreement with the jump-discontinuity observed in Fig. 8a,b.

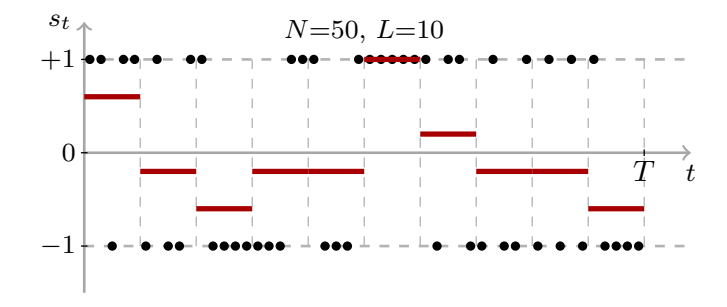


FIG. 12. Schematic representation of the coarse-graining average performed on a bang-bang protocol with N steps, into a piecewise-constant protocol with L time steps. The average value in each bin depends on the number of +1 and -1 that it contains; in the limit $N\rightarrow\infty$, different bang-bang protocols can approximate the same coarse-grained continuous protocol. This redundancy is responsible for the density of state factor $\rho[s]$ appearing in partition function (52) and estimated in (53).

C. Relation between $q_{BB}(T)$ and the partition function

Equation (30) shows that the piecewise-continuous protocol $s_{\Delta_0(T)}$ – the unique global optimal of the single-qubit control landscape for $T < T_{\rm QSL}$ – correctly reproduces the curve $q_{\rm BB}(T)$ in the region $T \in [0,T_{\rm QSL}]$. However, observe that $q_{\rm BB}(T)$ was originally defined as an order parameter computed for optimal protocols sampled within the bang-bang protocol space (cf. Eq. (5)); it is then natural to ask why the optimal protocol over the continuous protocol space correctly reproduces the behavior of an order parameter defined over bang-bang protocols (cf. Fig.12). In this section, we discuss the connection between the bang-bang and continuous protocol spaces. In particular, we show how the partition function (31), defined over the continuous protocol space, can be in general used to obtain results valid in the bang-bang protocol space.

In the bang-bang protocol space, the average $\langle s_i \rangle$ contained in the definition of the order parameter $q_{\rm BB}(T)$ can be explicitly written as

$$\langle s_i \rangle = \sum_{\{s_i\}} w(s)s_i, \qquad T > T_{\text{QSL}},$$

where the sum runs over the bang-bang protocol space and w(s) are generic weights.

In the limit of an infinite number of bang-bang steps $N{\to}\infty,$ a coarse-grain average of bang-bang protocols would give

$$\langle s_i \rangle = \int_{-1}^{+1} \prod_t \mathrm{d}s_t \, w[s] \rho[s] s_{t_i}, \qquad T > T_{\mathrm{QSL}},$$

where the density of states $\rho[s]$ keeps track of how many bang-bang protocols are mapped to the same continuous protocol by the coarse-grain average procedure (cf. Fig.12).

Therefore, we consider the partition function

$$Z_{\rm BB} = \int_{-1}^{+1} \prod_{t} ds_t \, \delta(I[s]) \rho[s], \qquad T > T_{\rm QSL},$$
 (52)

and we estimate $\rho[s]$ in the asymptotic limit $N\to\infty$ by subdividing the bang-bang protocol $\{s_i\}$ in L bins, each containing N/L consecutive bang-bang steps. Assuming the spins $s_i = \pm 1$ in each bin are uncorrelated, the single s_i becomes an independent random variable, and the number of equivalent configurations within each bin only depends on the number density of up or down spins (cf. Fig. 12). In the limit $N, L\to\infty, N/L\to\infty$ we obtain

$$\rho[s] = \prod_{t} \rho(s_t) = e^{\sum_{t} S(s_t)}$$

$$S(s_t) \sim -(N/L) [s_t^+ \log s_t^+ + s_t^- \log s_t^-],$$
(53)

where t labels the bin, $s_t^{\pm} = (1 \pm s_t)/2$ is the density of up and down spins in the bin s_t and $S(s_t)$ is the entropy associated with the variable s_t . Eventually, for a given protocol s we obtain the density of states $\rho[s] = e^{S[s]}$ associated with the Shannon entropy

$$S[s] = -\frac{N}{T} \int_0^T dt \left[s_t^+ \log s_t^+ + s_t^- \log s_t^- \right].$$
 (54)

This result is independent of the particular binning subdivision: changing the number of bang-bang steps s_i contained in each bin s_t yields the same density of states provided that spins in each bin remain decorrelated in the asymptotic limit $N \rightarrow \infty$.

Finally, in the same way as Sec. VIB, it is convenient

to rewrite the order parameter $q_{BB}(T)$ as

$$q_{\rm BB}(T) = 1 - \frac{1}{T} \int_0^T dt \, \langle s_t \rangle^2 = 1 - \sum_n (x_{0n} + \langle x_n \rangle)^2.$$
 (55)

1. Shannon entropy approximation

We would like to explicitly evaluate the partition function in Eq. (52). Unfortunately, the Shannon entropy makes the integral intractable by means of elementary analytical tools. Since we are interested in the simplest possible analytical estimate of the order parameter $q_{\rm BB}(T)$, we search for an approximation of the Shannon entropy which allows the partition function to be evaluated by elementary means. To this end, we substitute the nonlinear Shannon entropy with the quadratic function

$$S[s] \mapsto S_2[s] = \frac{N\alpha}{2} \left(1 - \frac{1}{T} \int_0^T dt \, s_t^2 \right) \tag{56}$$

where α is a positive free parameter. $S_2[s]$ is commonly known as the Tsallis entropy with entropic-index 2 [67]. Notice that α can be fixed by imposing a further constraint (for example, $\alpha=1$ approximates the Shannon entropy density around $s_t=0$ up to quadratic order). Still, its precise value will not affect the critical scaling of $q_{\rm BB}$. Finally, following the Shannon entropy approximation, we extend the integration domain of $\{s_t\}$ from [-1,1] to \mathbb{R} .

2. Computing $q_{BB}(T)$

Following the same steps as in Sec. VIB1, we arrive at the generating functional

$$G_{\rm BB}[k] = \int_{\mathbb{R}} \prod_{n} dx_n \int_{\mathbb{R}} \frac{d\mu}{2\pi} \exp\left[-\frac{N\alpha}{2} \sum_{n=1}^{L} (x_{0n} + x_n)^2 + i\mu \left(I + \frac{1}{2} \sum_{n=1}^{L} \lambda_n (x_{1n} + x_n)^2\right) + \sum_{n=1}^{L} k_n x_n\right], \quad (57)$$

where N represents the number of bang-bang steps of the "microscopic" protocol $\{s_i\}$ while L the number of steps of the "mesoscopic" protocol s obtained through the coarse-graining average.

Notice that $G_{\rm BB}[k]$ has the same structure as G[k]; in this case, $\kappa = \alpha(N/L)$ so that the Tsallis entropy (associated with the coarse-graining average) has the same effect as the hard-boundary constraint approximation in Sec. VIB 1. Therefore, Eq. (48) still holds and eventually

we obtain (see App. H)

$$\Delta q_{\rm BB}(T) = q_{\rm BB}(T) - q_{\rm BB,0}(T) \sim \text{const} + \Delta T, \quad L \to \infty$$
(58)

where $q_{\text{BB},0}(T)$ is defined in Eq. (30) for the single-qubit problem. Notice that this result deviates from the linear critical scaling observed in Fig. 10 by the presence of the constant contribution.

The origin of the constant contribution in $\Delta q_{\rm BB}(T)$ can be traced back to the quadratic-order truncation of the infidelity expansion. To see this, set $T=T_{\rm QSL}$ so that

the infidelity expansion centered in s_{Δ_0} reduces to

$$I[x] = \frac{1}{2} \sum_{n=1,2} \lambda_n x_n^2 + \dots$$

Consequently, within the quadratic expansion of the infidelity the partition function reduces to

$$Z_{\text{BB}} = \int_{\mathbb{R}} \prod_{n} dx_{n} e^{-N(\kappa/2) \sum_{n} (x_{0n} + x_{n})^{2}} \delta(I[x])$$
$$= \int_{\mathbb{R}} \prod_{n \ge 2} dx_{n} e^{-N(\kappa/2) \sum_{n > 2} (x_{0n} + x_{n})^{2}}.$$

From this expression, we observe two important facts valid for $T = T_{\text{QSL}}$. First, the delta-function constraint $\delta(I_T[s])$ enforces $\langle x_n \rangle = 0$ for n = 1, 2. Second, the quadratic-order truncation of the infidelity expansion, having $\lambda_{n>2} = 0$, does not impose any constraint on the variables $x_{n>2}$; in particular, $x_{n>2}$ remain subject to the entropic term, centered at $-x_{0n}$, that ultimately yields a non-vanishing expectation value $\langle x_n \rangle = -x_{0n}$ for n > 2. This is the origin of the constant contribute displayed by $\Delta q_{\text{BB}}(T)$ as $T \to T_{\text{QSL}}^+$. Finally, we also notice that, due to the finite expectation value $\langle x_n \rangle$, it follows that $\langle s_t \rangle$ is discontinuous at the T_{QSL} CLPT, namely

$$\langle s_t \rangle = \begin{cases} \sum_{n=1}^{\infty} x_{0n} f_t^{(n)}, & T = T_{\text{QSL}}^-\\ \sum_{n=1}^2 x_{0n} f_t^{(n)}, & T = T_{\text{QSL}}^+ \end{cases}.$$

This again shows the limitations of the quadratic-order truncation in the infidelity expansion.

We obtained the analytical scaling of the order parameter $q_{\rm BB}(T)$ predicted by the quadratic expansion of the infidelity for $T \rightarrow T_{\rm QSL}^+$. This result differs from the numerical critical scaling in Fig. 10 by the presence of a constant contribution. We showed that the constant contribution is an artifact of the quadratic-order expansion and is eliminated by higher-order terms (in particular, quartic-order). In this way, we understand the importance of higher-order terms in the infidelity expansion, for a correct estimate of the analytical critical scaling of $q_{\rm BB}(T)$ at the quantum speed limit CLPT. Computing $\langle x_n \rangle$ while including quartic-order contributions in the infidelity expansion can be done within the framework of perturbation theory and we leave this for future work.

VII. CONCLUSION

A. Summary of the main results

In this work, we combined different analytical and numerical techniques that shed new light on quantum control phase transitions. Essentially, our contribution is four-fold.

First, we derive three different analytical expansions that approximate the infidelity functional (or similar objective functions) of the single- and two-qubit control problems and capture the underlying control phase transitions. In particular, the Dyson and cumulant expansions admit an effective energy interpretation where the protocol configuration plays the role of a spin- or fieldconfiguration (depending on the constraints imposed on the protocol; cf. bang-bang vs. piecewise-continuous protocol space). The control phase transitions are captured by the approximate landscape provided the order of truncation is large enough. As we saw in Sec. IV, changing the center of the expansion allows one to reduce the order of truncation. In general, the main limitation of this method remains the curse of dimensionality: the matrices appearing in the infidelity expansion depend on the quantum evolution operator (control propagator) and their dimension grows exponentially with the size of the quantum system. For large quantum systems, one can introduce approximate methods for the evolution operator for an efficient explicit evaluation of the infidelity expansions.

Second, we analyze the near-optimal region of the control landscape by changing the parameter T, controlling the duration of the quantum evolution. By starting with infinitesimal T, we reduce the problem to a simple linear optimization problem. Incrementing the parameter T, we relate control phase transitions, previously observed exclusively via optimal search algorithms, to critical changes in the structure of the landscape around the optimal protocol(s) via stability analysis. We notice that this analysis can be performed provided one has already found the optimal protocol(s) of the landscape. In our case, the dimensionality and the symmetry of the problem allowed us to recover the optimal protocol for $T \le T_{\mathrm{QSL}}$ and $T \le T_{\mathrm{sb}}$ in the single- and two-qubit problem, respectively. For generic quantum system and control problems, finding optimal protocols is a non-trivial operation and one may use the available tools in quantum optimal control to find and trace optimal protocols as the duration of the quantum evolution T is varied.

Third, we use a gradient-free version of the Langevin-Monte Carlo algorithm (LMC) to explore the optimal level set, defined in the infinite-dimensional protocol space by the equation $I_T[s]=0$. Using LMC, we characterize some of its topological/geometrical properties (such as connectedness and bulk sizes) and we obtain a numerical estimate of the statistical observable q(T). Notice that LMC attempts to explore the optimal level set by considering stochastic fluctuations at finite inverse-temperature β , in the space of piecewise-constant functions with L steps. To overcome these numerical limitations, we explicitly check for finite-size effects by studying the results of the simulations while varying L and β by at least three orders of magnitudes.

Fourth, using path integrals, a well-known tool in statistical field theory, we estimate the critical behavior of order parameters q(T) and $q_{\rm BB}(T)$ for $T \rightarrow T_{\rm QSL}$ and compare with the numerical results obtained from Stochastic Descent and Langevin-Monte Carlo. This approach establishes a direct connection between the critical scaling

of the order parameters at the quantum speed limit with (i) the structural change occurring in the optimal level set of the control landscape and (ii) the constraint imposed on the protocol space. An important example is the jump-discontinuity in q(T), directly related to the infinite dimensions of the optimal level set. In this work, we approximate at the quadratic-order both the hard-boundary $(|s(t)| \le 1)$ and infidelity $(I_T[s] = 0)$ constraints a priori present in the partition function. We observe that higher-order corrections are mostly important for the infidelity expansion (cf. App. E). For q(T), these contributions are needed to obtain a precise numerical estimate of the jump-discontinuity in $T_{\rm QSL}$. In the case of $q_{\rm BB}(T)$, quartic-order contributions are important to reproduce the correct critical scaling.

B. Discussion and Outlook

By proposing a general framework for an analytical theory of quantum control landscapes, our work sheds new light on the theory of optimal control, which allows one to go beyond purely numerical studies. The perturbative expansions we develop for the effective landscape models reveal the control propagator as a central object in control landscape theory: indeed, the landscape of any specific control problem can be obtained by projecting this propagator onto the initial and target states, emphasizing its fundamental importance. Crucially, these expansions provide means to analytically derive controlled approximations for the quantum control landscape.

A key insight brought in by our theory is the reconciliation of seemingly disparate control problems under a unified analytical framework: e.g., the landscapes of fidelity maximization, energy minimization, and observable extremization, all admit a natural analytical description within the same formalism. Another interesting feature is the natural separation of quantum (i.e., physical) and control degrees of freedom, which makes the classical nature of control phase transitions evident. Whether these transitions are of equilibrium (i.e., thermodynamic) or nonequilibrium (i.e., spin-glass-like) character, remains an open question for many-body control problems; nevertheless, in the single- or two-qubit problem we show that (i) CLPTs are associated with critical changes in the optimal level set and (ii) local traps are absent or can be easily avoided; therefore, in these two cases, the landscape does not possess glassy complexity. In addition, our theory allows us to handle on equal footing continuous and discrete (e.g., bang-bang) control protocols: while the latter result in theoretically appealing \mathbb{Z}_2 Ising models, the former are often more relevant for experiments. Importantly the coupling constants in these classical landscape models do not depend on the family of control protocols used.

To analyze the critical behavior of the control landscape in the vicinity of the quantum speed limit (T_{QSL}) , we develop new techniques based on statistical field theory. For bang-bang protocols of duration less than $T_{\rm QSL}$, we show that multiple local minima can appear in the landscape as a result of the entropy associated with the number of different bang-bang approximations to a single continuous optimal protocol; hence, the bang-bang control landscape may be sensitive to the details of the time discretization, and exhibits features not necessarily representative of the behavior of the controlled physical system. Our theory circumvents this issue by providing a uniform description for bang-bang and continuous drives. This is expected to shed new light on the performance of state-of-the-art algorithms, such as QAOA [34, 68–70].

Beyond $T_{\rm QSL}$, we overcome the difficulty of taking into account boundary constraints (e.g., boundedness, bangbang, etc.) analytically by developing a novel path integral approach, inspired by techniques used to study spin glass physics. This allows us to obtain an analytical estimate of the critical scaling behavior of the protocol order parameter in the vicinity of $T_{\rm QSL}$. Our results pave the way for future applications of statistical field theory methods in the characterization of quantum control land-scapes and their phase transitions.

While we focused on two toy models where we computed the coefficients of the control landscape exactly, we expect our methodology to be broadly applicable. The formalism suggests straightforward extensions with littleto-no modifications to optimally control open few-qubit systems subject to dissipation or decoherence (Lindblad control), or exactly solvable many-body systems, such as the transverse-field Ising model, which admit a mapping to a collection of independent two-level systems. Moreover, by considering quantum models in which $H_{0,1}$ are random matrices drawn from a Gaussian unitary ensemble, the ensemble average of the effective landscape model may give rise to a classical spin-glass system already for a single-qubit control problem (cf. Sec. III). When it comes to investigating the properties of optimal control landscapes in nonintegrable quantum many-body systems, we believe one can develop suitable low-rank approximations to the control propagator [71], and then apply our techniques. Hence, our work lays the foundations for a comprehensive theory of control phase transitions.

ACKNOWLEDGMENTS

We would like to thank S. Cacciatori, M. Ciarchi, L. Piroli, M. Radice, M. Serbyn and X. Turkeshi for insightful discussions and F. Balducci for providing valuable comments on the draft of this paper. Funded by the European Union (ERC, QuSimCtrl, 101113633). Views and opinions expressed are however those of the authors only and do not necessarily reflect those of the European Union or the European Research Council Executive Agency. Neither the European Union nor the granting authority can be held responsible for them. M.B. was supported by the Marie Skłodowska-Curie grant agreement No 890711 (until 01.09.2022). Numerical simula-

26

tions were performed on the MPIPKS HPC cluster.

CONTENTS

I.	Introduction	1
II.	Toy models for quantum control landscape phase transitions (CLPTs) A. Single-qubit control landscape B. Two-qubit control landscape	2 4 4
III.	Perturbative expansions for the control landscape A. Analytical expansions for the infidelity B. Single-qubit problem C. Two-qubit problem	5 5 7 8
IV.	Stability analysis and control phase transitions A. Breakdown of adiabatic tracing of optimal protocols at the control critical points B. Single-qubit problem C. Two-qubit problem	8 9 9 11
V.	Stochastic dynamics within the optimal level set beyond the quantum speed limit A. Thermal relaxation stage B. Diffusion stage C. Equilibrium sampling stage	11 12 13 13
VI.	Critical behavior at the quantum speed limit A. Partition function 1. Optimal level set parametrization 2. Hard-boundary constraint approximation B. Relation between $q(T)$ and the partition function 1. Computing $q(T)$ C. Relation between $q_{\rm BB}(T)$ and the partition function 1. Shannon entropy approximation 2. Computing $q_{\rm BB}(T)$	14 15 16 17 17 18 19 20 20
/II.	Conclusion A. Summary of the main results B. Discussion and Outlook	21 21 22
	Acknowledgments	22
A.	Infidelity expansions 1. Taylor expansions centered around the	23

arbitrary protocol $s_0(t)$

B. Stochastic Descent (SD) simulations

expansions

expansion

2. Connection between Taylor and Dyson

3. Convergence of the Dyson and Magnus

C. (Quadratic	stability	analysis	
------	-----------	-----------	----------	--

D.	Gradient-free Langevin-Monte Carlo (LMC) simulations 1. Thermal relaxation stage 2. Diffusion stage 3. Equilibrium sampling stage	28 28 30 32
E.	Optimal level set parametrization	32
F.	Steepest-descent method	34
G.	Computing $q(T)$	35
Η.	Computing $q_{\rm BB}(T)$	35
	References	36

Appendix A: Infidelity expansions

In this appendix, we discuss in more detail the analytical expansions introduced in Sec. III. In the first two subsections, we introduce the infidelity Taylor expansion and show how it connects with the Dyson expansion. In the last subsection, we comment on the radius of convergence of the Dyson and Magnus expansions.

We assume a generic Hamiltonian with the form in Eq. (1). The procedure can be generalized to the case with multiple control parameters.

1. Taylor expansions centered around the arbitrary protocol $s_0(t)$

In what follows, we adopt the round and square brackets convention to distinguish between, respectively, the parametric dependence on the quantum duration T and the functional dependence on the control protocol s. Consider the Taylor expansion for the infidelity functional I[s](T):

$$I[s](T) = I[s_0](T) + \int_0^T dt_1 \frac{\delta I}{\delta s(t_1)} \bigg|_{s_0} \delta s(t_1) + \frac{1}{2!} \int_0^T d^2 t \frac{\delta I}{\delta s(t_1) \delta s(t_2)} \bigg|_{s_0} \delta s(t_1) \delta s(t_2) + \dots$$

$$= \sum_{i=0}^\infty \frac{1}{n!} \int_0^T d^n t \frac{\delta^n I}{\delta s(t_1) \cdots \delta s(t_n)} \bigg|_{s_0} \delta s(t_1) \cdots \delta s(t_n)$$
(A1)

where $\delta s(t) = s(t) - s_0(t)$ denotes deviation from protocol $s_0(t)$ at time t. The generic variational derivative

23

24

25

25

$$\frac{\delta^n I}{\delta s(t_1) \dots \delta s(t_n)} \bigg|_{s_0}$$

can be obtained explicitly from Eq. (2). The evolution operator $\hat{U}[s](T,0) = \mathcal{T}e^{-i\int_0^T \hat{H}(t)dt}$, acting on the left,

evolves quantum states from time t=0 to time t=T. Notice that \mathcal{T} represents the time-ordering operator. From the definition we obtain

$$\frac{\delta^{n} \langle \psi_{*} | \hat{U}[s](T,0) | \psi_{0} \rangle}{\delta s(t_{1}) \cdots \delta s(t_{n})} \bigg|_{s_{0}} =$$

$$(-i)^{n} \langle \psi_{*} | \mathcal{T} \hat{U}[s_{0}](T,t_{1}) \partial_{s} \hat{H}(t_{1}) \hat{U}[s_{0}](t_{1},t_{2}) \cdots \times$$

$$\hat{U}[s_{0}](t_{n-1},t_{n}) \partial_{s} \hat{H}(t_{n}) \hat{U}[s_{0}](t_{n},0) | \psi_{0} \rangle, \qquad (A2)$$

where $\partial_s \hat{H}$ denotes the partial derivative of \hat{H} with respect to the control parameter s. The time-ordering operator \mathcal{T} contained in the evolution operator ensures the correct time-ordering of the time labels $\{t_n\}$. As a consequence, the functional derivative of the unitary operator is symmetric under permutations of the time labels. For example, for n=1 we have

$$\frac{\delta \langle \psi_* | \hat{U}[s](T,0) | \psi_0 \rangle}{\delta s(t_1)} \bigg|_{s_0} = \tag{A3}$$

$$= (-i) \langle \psi_* | \hat{U}[s_0](T, t_1) \partial_s \hat{H}(t_1) \hat{U}[s_0](t_1, 0) | \psi_0 \rangle. \quad (A4)$$

For n=2,

$$\frac{\delta^2 \langle \psi_* | \hat{U}[s](T,0) | \psi_0 \rangle}{\delta s(t_1) \delta s(t_2)} \bigg|_{s_0} =$$

$$(-i)^2 \langle \psi_* | \hat{U}[s_0](T,t_1) \partial_s \hat{H}(t_1) \times$$

$$\hat{U}[s_0](t_1,t_2) \partial_s \hat{H}(t_2) \hat{U}[s_0](t_2,0) | \psi_0 \rangle \tag{A5}$$

where we assumed $t_1>t_2$ (if $t_2>t_1$ one exchanges $t_1\leftrightarrow t_2$ in the right-hand side to preserve the correct timeordering). The infidelity Taylor expansion can be easily written in terms of the variational derivative of the unitary operator $\hat{U}[s](T)$ given above. Introducing the variable $z=\langle \psi_*|\hat{U}[s](T,0)|\psi_0\rangle$ and its complex conjugated \bar{z} as shorthand notation, we have $I[s](T)=1-\bar{z}z$ and

$$\frac{\delta I}{\delta s(t_1)} \Big|_{s_0} = -2 \operatorname{Re} \left[\bar{z} \frac{\delta z}{\delta s(t_1)} \Big|_{s_0} \right] \tag{A6}$$

$$\frac{\delta^2 I}{\delta s(t_2) \delta s(t_1)} \Big|_{s_0} = -2 \operatorname{Re} \left[\bar{z} \frac{\delta^2 z}{\delta s(t_2) \delta s(t_1)} \Big|_{s_0} + \frac{\delta \bar{z}}{\delta s(t_2)} \Big|_{s_0} \frac{\delta z}{\delta s(t_1)} \Big|_{s_0} \right]. \tag{A7}$$

where Re indicates the real part. Notice that in $t_1=t_2$ (or in $t_i=t_j$ when n>2) the variational derivative has a removable discontinuity. Our analysis is not affected by these discontinuities: in the functional expansions the derivatives appear under integration and the discontinuities involve a zero-measure set.

In Sec. III we conveniently rewrite the infidelity in terms of the orthogonal evolution operator (cf. Eq. (10)). Let us now consider the Taylor expansion in the orthogonal operator space. Repeating the same steps as above

we obtain

$$\frac{\delta^{n} I[s](T)}{\delta s(t_{1}) \dots \delta s(t_{n})} \bigg|_{s_{0}} = \\
-(1/2)\vec{n}_{*} \cdot \mathcal{T} M[s_{0}](T, t_{1}) \,\partial_{s} m \,M[s_{0}](t_{1}, t_{2}) \dots \times \\
M[s_{0}](t_{n-1}, t_{n}) \,\partial_{s} m \,M[s_{0}](t_{n}, 0) \,\vec{n}_{0}. \tag{A8}$$

where m(t) is the generator of the orthogonal evolution operator associated with the Hamiltonian $\hat{H}(t)$. By comparison with the same expansion in the unitary operator space, we see that the orthogonal operator space allows a considerable simplification of each term in the series: the n-th order coefficients of the infidelity expansion simply corresponds to the n-th functional derivative of the infidelity. In particular, in the orthogonal operator space each term is simply given by an alternating product of evolution operators $M[s_0](t_i, t_{i+1})$ and generators $\partial_s m(t_i)$. For example, for n=1

$$\frac{\delta I[s](T)}{\delta s(t_1)} \bigg|_{s_0} = -(1/2)\vec{n}_* \cdot M[s_0](T, t_1) \times \\ \partial_s m(t_1) M[s_0](t_1, 0) \vec{n}_0 \tag{A9}$$

and for n=2,

$$\frac{\delta^2 I[s](T)}{\delta s(t_1)\delta s(t_2)} \bigg|_{s_0} = \\ -(1/2)\vec{n}_* \cdot M[s_0](T, t_1) \,\partial_s m(t_1) \times \\ M[s_0](t_1, t_2) \partial_s m(t_2) M[s_0](t_2, 0) \,\vec{n}_0$$
(A10)

when $t_1 > t_2$.

2. Connection between Taylor and Dyson expansions

As in Sec. $\overline{\text{III}}$, let us now perform the reference-frame transformation

$$\hat{H}(t) \mapsto \hat{H}'(t) = \hat{U}_0^{\dagger}(t,0)[\hat{H}(t) - i\partial_t]\hat{U}_0(t,0)$$
$$\hat{U}[s](T,0) \mapsto \hat{U}_0(T,0)\hat{U}'[s](T,0)$$

where

$$\hat{U}_0(T,0) = \exp\left(-iT\hat{H}_0\right)$$
$$\hat{U}'[s](T,0) = \mathcal{T}e^{-i\int_0^T dt \hat{H}'(t)}.$$

We obtain $\hat{H}'(t) = U_0^{\dagger}(t,0)\hat{H}_1(t)\hat{U}_0(t,0)$ so that the new Hamiltonian $\hat{H}'(t)$ is proportional to the protocol s(t). Consequently, for s=0 the new evolution operator $\hat{U}'[s](T,0)$ reduces to the identity operator: $\hat{U}'[0](T,0) = 1$.

Similarly, in the dual space we perform the referenceframe transformation,

$$m(t) \mapsto m'(t) = M_0(T,0)^{t} [m(t) - \partial_t] M_0(T,0)$$

 $M[s](T,0) \mapsto M_0(T,0) M'[s](T,0)$

where

$$M_0(T,0) = \exp(Tm_0)$$

 $M'[s](T,0) = \mathcal{T}e^{\int_0^T dt \, m'(t)}$

Again, the new generator m'(t) in the orthogonal operator space is proportional to the protocol s(t): $m'(t)=M_0(T,0)^{\rm t}m_1(t)M_0(T,0)$. Hence, for s=0 the evolution operator reduces to the identity operator: $M'[0](T,0)=\mathbb{1}$.

The properties $\hat{U}'[0](T,0)=\mathbb{1}$ and $M'[0](T,0)=\mathbb{1}$ considerably simplify the coefficients appearing in the infidelity expansion. From Eqs. (A2) and (A8) we obtain,

$$\frac{\delta^{n} \langle \psi_{*} | \hat{U}'[s](T,0) | \psi_{0} \rangle}{\delta s(t_{1}) \cdots \delta s(t_{n})} \bigg|_{s_{0}} =$$

$$(-i)^{n} \langle \psi_{*} | \hat{U}_{0}(T,0) \mathcal{T} \partial_{s} \hat{H}'(t_{1}) \cdots \partial_{s} \hat{H}'(t_{n}) | \psi_{0} \rangle \quad (A11)$$

and

$$\frac{\delta^n I[s](T)}{\delta s(t_1) \dots \delta s(t_n)} = -(1/2)\vec{n}_* \cdot M_0(T, 0)\mathcal{T}\partial_s m'(t_1) \dots \partial_s m'(t_n)\vec{n}_0$$

Notice that for n=1,2 this last result corresponds to the "interaction terms" in Eq. (15); this expression generalizes the Dyson expansion terms presented in Sec. III to an arbitrary order $n \in \mathbb{N}$.

3. Convergence of the Dyson and Magnus expansion

The quantum control problems introduced in Sec. II have a finite-dimensional Hilbert space and are defined over the space of bounded control protocols ($|s| \le 1$). The Dyson expansion is absolutely convergent for any fixed $T < \infty$ under these assumptions. To see this, consider the generic evolution operator

$$\hat{U}(T,0) = \mathcal{T}_t \exp\left(-i \int_0^T dt \, \hat{H}(t)\right) \qquad \text{or}$$

$$M(T,0) = \mathcal{T}_t \exp\left(\int_0^T dt \, m(t)\right)$$

and observe that each term in the associated Dyson series is bounded. For example,

$$\left\| \mathcal{T}_t \exp\left(\int_0^T dt \, m(t) \right) \right\| = \left\| \sum_{n=0}^\infty \frac{1}{n!} \int_0^T d^n t \, \prod_{i=0}^n m(t_i) \right\|$$

$$\leq \sum_{n=0}^\infty \left\| \frac{1}{n!} \int_0^T d^n t \, \prod_{i=1}^n m(t_i) \right\|$$

$$\leq \sum_{n=0}^\infty \frac{1}{n!} \int_0^T d^n t \, \prod_{i=1}^n \|m(t_i)\|.$$

where we used the triangular inequality and the sub-multiplicative property of the operator (matrix) norm. From the aforementioned assumptions it follows $C = \max_t \|m(t)\| < \infty$ and the Dyson expansion is then bounded by the numerical series

$$\sum_{n=0}^{\infty} a_n = \sum_{n=0}^{\infty} \frac{(TC)^n}{n!} = e^{TC},$$

for $T<\infty$.

From this result, we have a conservative estimate of the order of truncation P of the Dyson expansion, after which higher-order terms decrease in norm. By setting $a_{P-1}{=}a_P$, this yields $P{=}TC$: P grows linearly with T and $C{=}\max_t\|m(t)\|$. In the single-qubit problem in Eq. (18), we have $C{\simeq}h_x{=}\sqrt{5}$ and $T_{\rm QSL}{\simeq}2.5$ so that $P{\simeq}6$. In the two-qubit case in Eq. (19), $C{\simeq}\sqrt{2}h_x{=}\sqrt{10}$ and $T_{\rm QSL}{\simeq}3.0$ yield $P{\simeq}10$.

Contrary to the Dyson expansion, the Magnus expansion has a finite radius of convergence. The sufficient condition for the convergence of the Magnus expansion reads [54]

$$\int_{0}^{T_{\text{Mag}}} \mathrm{d}t \, \|m(t)\| \le \pi. \tag{A12}$$

In the case of Eq. (16), this yields a relatively short radius of convergence: using the upper bound $||m(t)|| \le C$, in the single- (two-) qubit problem we have $T_{\text{Mag}} \approx 1.4$ ($T_{\text{Mag}} \approx 1.0$) while, for comparison, the quantum speed limit is $T_{\text{QSL}} \approx 2.5$ ($T_{\text{QSL}} \approx 3.0$).

Nevertheless, the sufficient condition in Eq. (A12) depends on the specific protocol s(t) appearing in m(t) so that the Magnus expansion may still converge in a subregion of interest in the protocol space. For example, in the single-qubit problem the optimal protocol $s_{\Delta_0(T)}$ for $T \leq T_{\text{QSL}}$ yields (cf. Sec. IV)

$$\int_0^T \mathrm{d}t \, \big\| m(t)[s_{\Delta_0(T)}] \big\| = T_c h_x < \pi, \quad T \le T_{\mathrm{QSL}}.$$

Finally, notice that the Magnus expansion can be centered around an arbitrary protocol $s\neq 0$ via reference-frame transformation. This property can be used to obtain a convergent Magnus expansion in an arbitrary region of interest in the protocol space.

Appendix B: Stochastic Descent (SD) simulations

In this section we provide additional information on the Stochastic Descent simulations (SD) used in Sec. III to sample locally-optimal bang-bang protocols in the quantum control landscape.

In the Stochastic Descent algorithm, the initial bangbang protocol is drawn from a uniform distribution siteper-site: $s_i = \pm 1$. At each iteration, a spin-flip $s_j \mapsto -s_j$ at random site j is performed; the modified protocol is accepted whenever it leads to decrement in the infidelity; otherwise the spin-flip is undone. The algorithm terminates when a single spin-flip in all sites does not decrease infidelity. For each T we collect 250 locallyoptimal protocols from 250 independent SD runs. From the set of locally-optimal protocols, \mathcal{S} , we estimate the average protocol $\langle s_i \rangle_{\mathcal{S}}$ and compute $q_{\mathrm{BB}}(T)$ (cf. Eq. (5)). Notice that we do not observe any sensible change in the curve $q_{BB}(T)$ by doubling the number of locally-optimal protocols sampled. In the exact infidelity landscape we let SD search in the space of bang-bang protocols with $N_{\rm ex}$ =5000 bang-bang steps. In the case of the approximated infidelity landscape, SD searches in the space of bang-bang protocols with N=500 bang-bang steps. The different numbers $N_{\rm ex}, N$ of bang-bang steps in the two infidelity landscape (exact and approximated, respectivaly) is motivated by the different scalings in the number of bang-bang steps exhibited by the numerical $q_{BB}(T)$ curve. Intuitively, the different scaling behavior is related to the different type of discretization: in the exact infidelity the bang-bang protocol directly enters the unitary operator; instead, the infidelity expansions are derived in the more general space of piecewise-continuous protocols, and the bang-bang constraint is imposed after the expansion is performed.

In Secs. III B, III C we showed the comparison between the curve $q_{BB}(T)$ obtained from SD performed over the exact infidelity landscape and the approximated infidelity landscape. It is also interesting to compare the minimum infidelity obtained. In the single-qubit case, from Fig. 13 (left column) we see that for small T all the expansions at the highest order have minimum infidelity close to the exact landscape result. For $T \gtrsim 3.0$, the Dyson expansion (panel a) breaks the unitarity of the evolution operator and infidelity is not bounded within [0,1]. On contrary, the Magnus and cumulants expansions (panel b and c) approximate the minimum infidelity curve in the whole interval $T \in [0, 3.5]$. In the two-qubit case, the Dyson and cumulant expansions (panel d and e) break down beyond $T \approx 2$ while the Magnus expansion (panel f) reproduces the exact landscape minimum infidelity curve in the whole interval $T \in [0, 4]$.

Let us now show how the number of bang-bang steps N affects the order parameter curve $q_{\rm BB}(T)$. In Fig. 14 the curve $q_{\rm BB}(T)$ is plotted for the Magnus expansion truncated at third order for different numbers of bang-bang steps N. As N increases, the main change in $q_{\rm BB}(T)$ occurs around the critical points: $T_c, T_{\rm QSL}$ for the single-qubit (panel a) and $T_{\rm sb}, T_{\rm QSL}$ for the two-qubit problem (panel b). Notice that in the two-qubit case, convergence of $q_{\rm BB}(T)$ is significantly slower around the critical points $T=T_{\rm QSL}$. Nevertheless, in both cases the qualitative behavior of the curve $q_{\rm BB}(T)$ is already visible for $N \gtrsim 250$.

Finally, in Fig. 15 we directly compare the average protocols $\langle s_i \rangle_{\mathcal{S}}$ extracted from the different SD simulations in the single-qubit problem. Besides the order parameter q(T) and fidelity F(T), which effectively reduce the complexity of the system to a single value, in this plot we

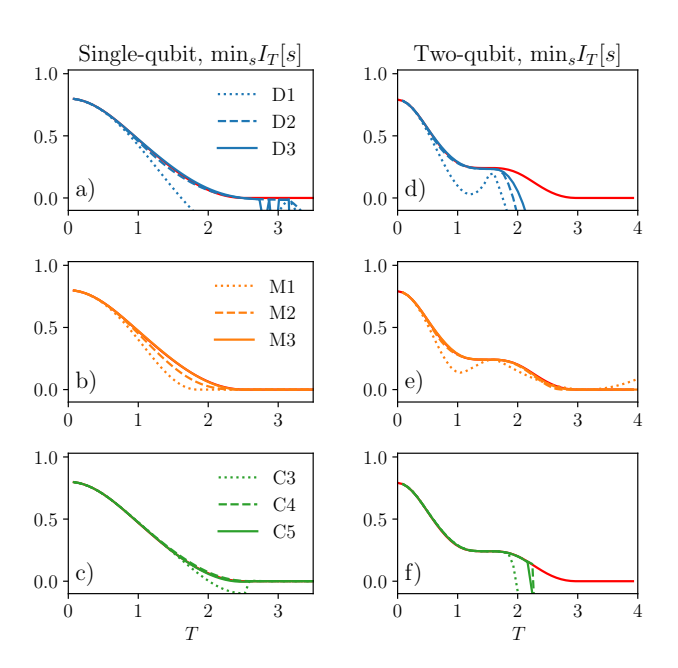


FIG. 13. SD results complementing Fig. 2. In the plot, we compare the minimum infidelity $\min_s I_T[s]$ achieved in the approximated control landscapes with respect to the exact control landscape (showed in red). Magnus is the only expansion preserving infidelity's domain [0,1] and closely following the exact (red) curve. The Dyson and cumulants expansions break by construction the unitarity of the evolution operator and this leads to strong deviations in the corresponding curves (for $T\gtrsim 2.5$ and $T\gtrsim 2.0$ in the single- and two-qubit problem, respectively). The letters D, M, and C in the legend stand for Dyson, Magnus, and Cumulant expansion while the adjacent integer specifies the order of truncation.

observe precisely how much the approximated landscapes reproduce the correct optimal protocol. Even though the Magnus expansion at third order better approximates the order parameter curve $q_{\rm BB}(T)$, the average sampled protocols in Magnus do not always follow the qualitative behavior of the exact result (cf. Fig. 15c). On the contrary, the average protocols sampled by the Dyson and cumulants expansions possesses the qualitative structure of the exact result. From this result, we understand that the quality of the approximation associated with the analytical expansions may sensibly depend on the features one is interested to compare.

Appendix C: Quadratic stability analysis

In this section we provide details about the quadratic stability analysis presented in Sec. IV. The analysis is based on the numerical diagonalization of the Hessian operator $J_{t_1t_2}(T)$ appearing in Eqs. (15) and (21). Numerically, we discretize the operator in an $L \times L$ matrix and account for the scaling prefactor 1/L.

First, we show how the Hessian eigenvalues scale as a

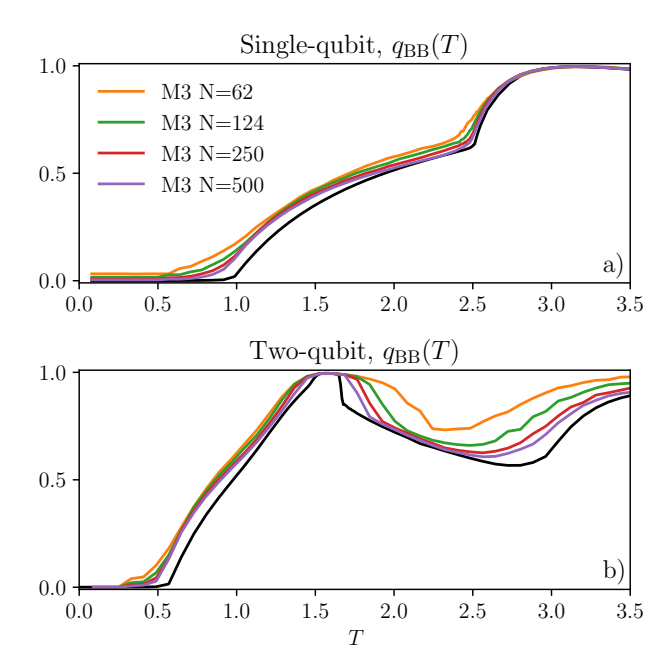


FIG. 14. SD results complementing Fig. 2. Finite-size scaling of the curve $q_{\rm BB}(T)$ obtained via Magnus expansion, as the number of bang-bang steps N is increased. For reference, in black we report the curve $q_{\rm BB}(T)$ obtained in the exact control landscape (with $N_{\rm ex}{=}5000$ bang-bang steps). In the legend, "M3" stands for Magnus expansion truncated at third order.

function of the discretization points. Let us consider explicitly the single-qubit problem and the quadratic operator relative to the protocol $s_{\Delta_0(T)}$, defined in Eq. (24) and optimal in the $[T_c, T_{QSL}]$ interval. In Fig. 16a,b we show how eigenvalues scale as L=16, 32, 64 at T=2.50, 2.52. The convergence in L is relatively fast both for positive and negative eigenvalues. Notice the change in sign happening exactly after T_{QSL} : beyond this critical point, L-2 negative eigenvalues are present. It is also interesting to visualize the eigenfunctions associated to the numerical diagonalization. In Fig. 16c,d we show the first six eigenfunctions of the quadratic operator for L=64, T=2.52. Except for the eigenfunction $f^{(2)}$, the eigenbasis $\{f^{(n)}\}$ appear to be a (relatively small) deformation of the standard Fourier basis on the [0, T] domain. The role of the $f^{(2)}$ eigenfunctions becomes clear when considering deformations of $s_{\Delta_0(T)}$ along the directions of the eigenfunctions (see App. E).

Second, in Fig. 17 we show how eigenvalues of the Hessian operator change around the $T_{\rm QSL}{\simeq}2.95$ in the two-qubit problem. In particular, the infidelity expansion is centered around one of the two isolated optimal protocols found numerically by the LMC algorithm, for each fixed T (cf. App. V). In LMC, the time interval [0,T] is divided in $L{=}64$ uniform points and protocols are then piecewise constant on L steps. To reduce finite size effects in the computation of the spectrum, the Hessian operator is instead discretized in $L'{=}256$ steps: the op-

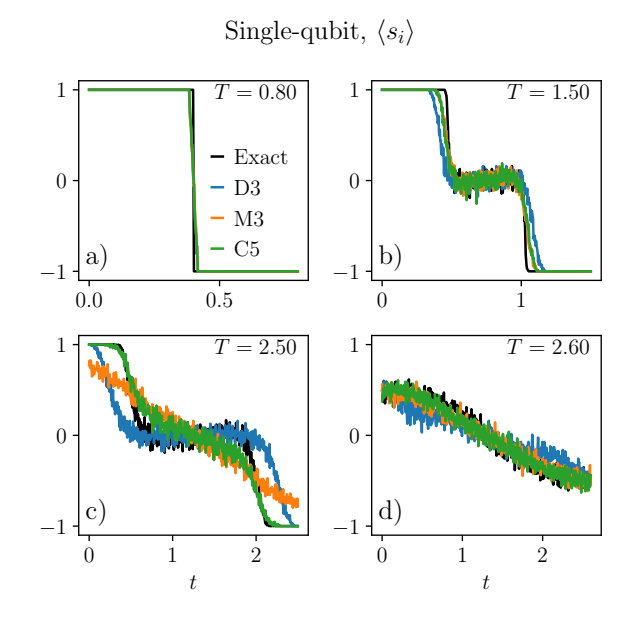


FIG. 15. Single-qubit problem: average protocols $\langle s_i \rangle$ for different quantum durations $T{=}0.80, 1.50, 2.50, 2.60$. The average is performed over 250 bang-bang protocols sampled by SD in the exact and approximated control landscapes – D3: Dyson expansion truncated at third order; M3: Magnus expansion truncated at third order; C5: cumultants expansion truncated at fifth order (cf. Sec. III). Interestingly, from panel (c) we observe that the shape of optimal protocols may qualitatively differ in the approximated and exact landscapes. This suggests some care when using the infidelity expansions to predict the shape of optimal protocols, even when they reproduce quantitatively well the behavior of other observables (such as $q_{\rm BB}(T)$ in Fig. 2).

timal protocol with L' steps is obtained by interpolating the optimal protocol with L steps found by LMC (using function interp from Python's package NumPy). Notice that, for $T_{\rm sb} \leq T \leq T_{\rm QSL}$, the two isolated optimal protocols present in the landscape are related to each other via the control problem symmetry $s(t) \leftrightarrow -s(T-t)$ [41]. As the infidelity is invariant under this symmetry transformation, the Hessian operators relative to the two optimal protocols possess the same spectrum. The Hessian spectrum shows qualitatively similar behavior to the single-qubit case (cf. Fig. 5a) except for the number of non-vanishing eigenvalues: four for the two-qubit, two for the single-qubit. Notice that, in the two-qubit case, the L-4 eigenvalues are not exactly zero for $T \ge T_{OSL}$, since the protocol chosen as the center of the infidelity expansion (at each fixed T) is optimal within numerical error; in this case, the error depends on the finite number of discretization steps, L, L', and the finite value of the parameter β appearing in the LMC update rule (27).

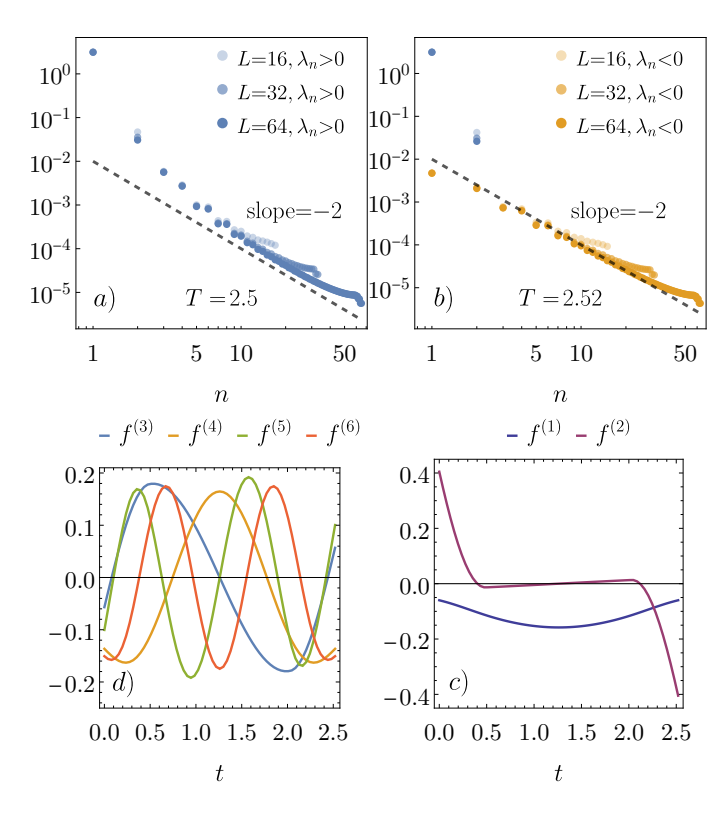


FIG. 16. Single qubit-problem. (a),(b) Spectrum of the discretized second-order operator in Eq. (9) relative to the protocol $s_{\Delta_0(T)}$ (cf. Eq. (23)), optimal for $T \rightarrow T_{\mathrm{QSL}}^- \simeq 2.51$. We observe the characteristic scaling of eigenvalues $\lambda_n \sim n^{-2}$ in the $L \rightarrow \infty$ limit. (c),(d) Eigenfunctions associated with the two positive and the first four negative eigenvalues at T=2.52. Notice the close similarity to the Fourier basis.

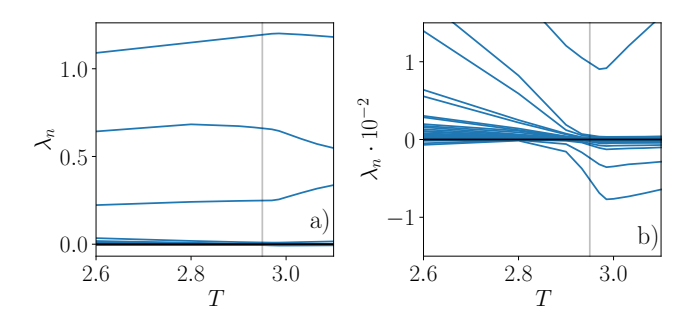


FIG. 17. Two-qubit problem: spectrum of the Hessian operator around $T_{\rm QSL}{\simeq}2.95$ (vertical gray line). The infidelity expansion is centered around one of the two optimal protocols found by the LMC algorithm introduced in Sec. V (the spectrum is identical for the two optimal protocols as discussed in App. C). From the plot, we see L-4 eigenvalues vanishing for $T{\to}T_{\rm QSL}$, up to deviations due to numerical errors. The result is analogous to the single-qubit case, shown in Fig. 5.

Appendix D: Gradient-free Langevin-Monte Carlo (LMC) simulations

In this appendix we present in more detail results from the LMC dynamics. We divide the discussion into three sections, respecting the three consecutive stages of LMC dynamics: thermal relaxation, diffusion along the optimal level set valleys and equilibrium sampling, as each one of the three stages is affected by CLPTs.

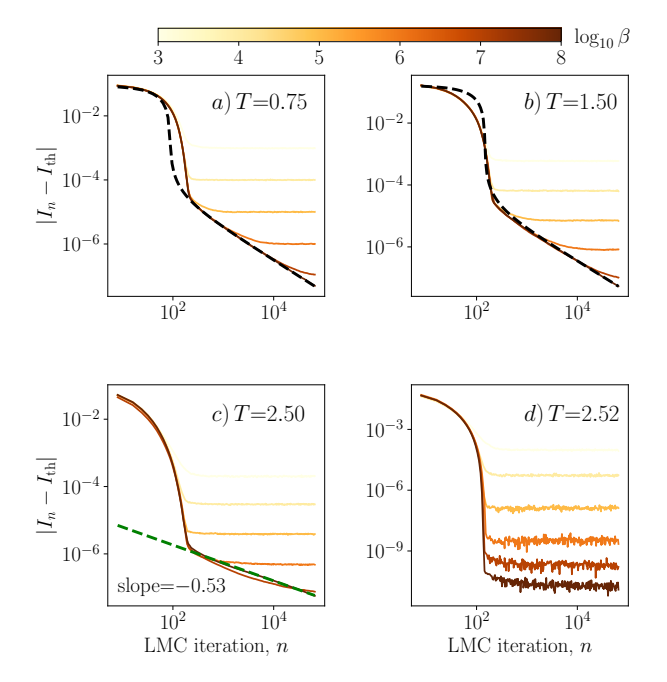
First, let us clarify the reason behind the simple dynamics of the algorithm. We discarded the gradient term, normally present in the Langevin update rule, because we are interested in exploring the optimal $(I_T[s]=0)$ level set, where the gradient term (as well as $L-n_+$ eigenvalues of the Hessian operator, with the positive integer n_+ dependent on the quantum control problem) are expected to vanish (cf. Sec. IV). Reinstating it results in a faster convergence to the optimal level set in the first part of the LMC simulations. However, its contribution during the level set exploration is expected to be less relevant.

Second, this algorithm uses purely stochastic moves to explore the optimal level set. Note that the update rule above is likely not the most efficient one: for example, one may exploit the Hessian analysis and restrict the stochastic move to the Hessian eigenspace associated with vanishing eigenvalues. This modification would probably result in a higher acceptance rate during the Metropolis rule (since in the update rule the infidelity would be preserved up to second order corrections), albeit at the cost of requiring more computational time due to implementing an update in a rotated basis. Nevertheless, as a first approach, we prefer to avoid any bias in the numerical exploration of the optimal level set at the cost of a less efficient algorithm.

We tested LMC dynamics varying parameters in the following intervals: $T \in [0,3]$, $\sigma \in [10^{-4}, 10^{-3/2}]$ and $\beta \in [10^2, 10^8]$. At the beginning of each LMC run, the initial protocol configuration $s_0 = (s_{0,1}, \ldots, s_{0,L})$ is chosen randomly by drawing each component $s_{0,i}$ from the uniform distribution in [-1,1]. We define a single LMC iteration as L local attempted moves.

1. Thermal relaxation stage

In Fig. 18 and 19 we show how infidelity changes as the LMC dynamics evolves the protocol for $\beta = 10^3, 10^4, \dots, 10^8, \sigma = 10^{-3/2}$, in the single- and two-qubit problem, respectively. In the single qubit case, we plot the infidelity difference between the LMC and the theoretical optimal value computed from the exact solution of the problem [40]. In the two-qubit case, the exact solution is not known and we plot the discrete derivative of the infidelity as a function of the LMC iteration. In both cases, we average over a set of ten independent LMC runs. When the Monte Carlo inverse-temperature β is large enough, the average motion in the thermal relaxation stage does not depend sensibly on it. In this



Single-qubit problem. The plots show the infidelity during thermal relaxation, averaged over ten independent LMC runs. The parameter T, different in the four panels, is changed to investigate the effects of CLPTs (cf. $T_c \simeq 0.98, T_{\text{QSL}} \simeq 2.51$). Each curve refers to a different Monte Carlo inverse-temperature β while $\sigma=10^{-3/2}$, L=512are fixed. In particular, we plot the absolute value of the difference between the infidelity and the exact optimal infidelity, analytically known in the single-qubit case (but not in the two-qubit case, cf. Fig. 19). Interestingly, in each panel, the six curves lie on top of each other until thermalization occurs. A simple effective one-dimensional toy model (blackdashed line in panels (a) and (b), cf. (D2)) reproduces the typical scaling observed in the numerical data when T is sufficiently different from the critical value $T_{\rm OSL} \simeq 2.51$. At T=2.50(panel (c); just before T_{QSL}), the $\simeq 1/2$ slope differs from the =1 slope characteristic of the late-time scaling of the onedimensional model in Eq. (D4). On the contrary, at T=2.52(panel (d); just beyond T_{QSL}), LMC dynamics thermalizes much faster.

case, the infidelity (derivative) curve displays in general two consecutive transient behaviors: the first one characterizes the dynamics at early iterations whereas the second one originates with a sudden transition (occurring around LMC iteration $n=10^2$ for $\sigma=10^{-3/2}$) and terminates once the system reaches the thermal equilibrium in the low-infidelity region. As visible from the plots, these two sub-stages possess distinct characteristic scaling behaviors independent of β .

The characteristic scaling behaviors observed during the LMC thermal relaxation stage for $\beta \gtrsim 10^3$ are captured to some extent by an effective one-dimensional toy model. Consider a one-dimensional system $x_n \in \mathbb{R}$ evolving according to LMC dynamics in Eq. (26) in the landscape $I(x)=\alpha|x-x_{\min}|$ from a random initial position $x_0 \neq x_{\min}$. The transition probability for a single iteration is then

$$P(x_{n+1}|x_n) = \mathcal{N}_{x_{n+1}}(x_n, \sigma) p_{\text{acc}}(\Delta I_n).$$
 (D1)

where $\mathcal{N}_x(x_n, \sigma)$ is a Gaussian distribution centered at x_n with variance σ^2 , $p_{\rm acc}(\Delta I_n) = \max(1, e^{-\beta \Delta I_n})$ is the Metropolis acceptance probability and $\Delta I_n = I(x_{n+1})$ – $I(x_n)$ is the change in infidelity during the iteration. On average, the final state is then

$$\mathbb{E}(x_{n+1}|x_n) = \int_{\mathbb{R}} dx_{n+1} \, x_{n+1} P(x_{n+1}|x_n).$$

For $\beta \rightarrow \infty$, thermal effects play no role since $p_{\rm acc}(\Delta I_n) \rightarrow {\rm sgn}(\Delta I_n)$. In this case, the dynamics only depends on σ and the relative distance $\ell_n = |x_n - x_{\min}|$ between x_n and the minimum of the infidelity at x_{\min} . Through a change of coordinate we fix $x_n=0$ and $x_{\min}>0$. Then, in the limit $\beta \rightarrow \infty$ we obtain

$$\mathbb{E}(x_{n+1}|x_n=0) = \int_{\mathbb{R}} dx_{n+1} \, x_{n+1} \mathcal{N}_{x_n+1}(0,\sigma) \operatorname{sgn}(\Delta I_n)$$
$$= \int_0^{2\ell_n} dx_{n+1} \, x_{n+1} \mathcal{N}_{x_n+1}(0,\sigma)$$
$$= \sqrt{\frac{\sigma^2}{2\pi}} (1 - e^{-(1/2)(2\ell_n)^2/\sigma^2}).$$

Thus, while averaging over different LMC realizations, we obtain the differential equation for ℓ_n

$$\frac{\mathrm{d}\ell_n}{\mathrm{d}n} \approx -\mathbb{E}(x_{n+1}|x_n=0),\tag{D2}$$

where we promoted n to a continuous variable assuming sufficiently small changes in ℓ_n over single LMC iterations. This equation admits simple closed-form solutions in the two limiting cases

$$\ell_n/\sigma \gg 1$$
: $\ell_n \sim -\alpha_1 n$ (D3)

$$\ell_n/\sigma \gg 1$$
: $\ell_n \sim -\alpha_1 n$ (D3)
 $\ell_n/\sigma \ll 1$: $\ell_n \sim \alpha_2 n^{-1}$ (D4)

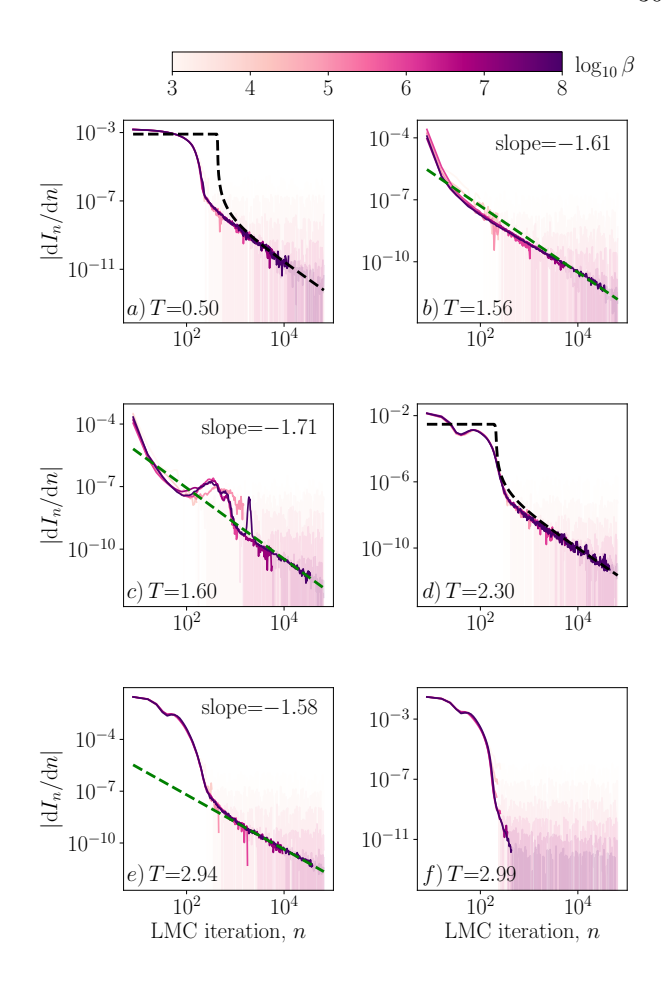
where the two prefactors $\alpha_{1,2}$ depends on σ . These two analytical limiting cases are related with the two characteristic scaling behaviors visible in Figs. 18 and 19. In the single-qubit system, the prediction in Eq. (D2) fits qualitatively well the whole numerical curves away from the $T_{\rm OSL} \simeq 2.51$ transition (black dashed curve in Fig. 18a,b); in the two-qubit problem, the same is true away from the $T_{\rm sb}{\simeq}1.57$ transition and again before the $T_{\rm QSL}{\simeq}2.95$ transition (black dashed curve in Fig. 19a,d). In this way, we gain intuition about the two characteristic scaling behaviors visible during LMC thermal relaxation stage: the first (second) transient behavior characterizes the motion when the protocol \mathbf{s}_n is sufficiently far away from (close to) the low-infidelity region with respect to the average jump-size σ of the Langevin update rule.

Interestingly, the scaling behavior changes across the CLPT at the quantum speed limit. For example, in the single-qubit system compare T=2.50 with T=2.52

(cf. $T_{QSL} \simeq 2.51$) or in the two-qubit system T=2.94 with T=2.97 (cf. $T_{\rm OSL}\simeq 2.95$). We observe that the early-time characteristic behavior remains qualitatively unaffected by the $T_{\rm QSL}$ transition: we deduce that there are no significant changes around $T_{\rm OSL}$ in the infidelity landscape in the high-infidelity region. On the contrary, the $T_{\rm QSL}$ transition heavily affects the scaling behavior in the latetime thermal relaxation stage. Observe that the latetime characteristic scaling at the two sides of the T_{QSL} transition has opposite behavior: it slows down when $T \rightarrow T_{\mathrm{QSL}}^-$ and it becomes fast when $T \rightarrow T_{\mathrm{QSL}}^+$. On a qualitative level, the different behavior at the two sides of the $T_{\rm QSL}$ transition can be understood as follows. In the limit $T \rightarrow T_{\mathrm{QSL}}^-$, the stochastic search for the unique optimal protocols is complicated by an increasing number of sub-optimal protocols having similar infidelity as the true optimal protocol. In the other case, for $T \rightarrow T_{\text{OSL}}^+$, there is an extensive number of optimal protocols and the stochastic dynamics easily converges to one of the many possible minima. More in detail, at $T = T_{QSL}^-$, the latetime characteristic scaling is $n^{-1/2}$ (notice the scaling n^{-1} observed away from the $T_{\rm QSL}$ transition). This different scaling behavior is phenomenologically explained by the one-dimensional effective model by assuming an effective potential $V(|x|) \propto |x|^{1/2}$ in the $\ell_n \ll \sigma$ case. On the other side, at $T = T_{\text{QSL}}^+$, the second transient is not visible at all: all curves converge approximately simultaneously to the low-infidelity region shortly after the end of the first transient. This other behavior is due to the presence of many optimal protocols and is effectively described in the one-dimensional model by an extended flat valley V=0 with a length greater than the σ .

The two-qubit problem presents additional features not observed in the single-qubit case. Around the $T_{\rm sb} \simeq 1.57$ transition, the early-time scaling behavior is different than what is observed for other values of T. In particular, for T=1.56 the scaling during the thermal relaxation phase is approximately algebraic (with a slightly different slope in the early- and late-time thermal relaxation substages). For T=1.60, the same scaling persists but an additional "bump" in the infidelity curve is now separating the two sub-stages. Although a more detailed analysis is needed to better understand this other behavior, intuitively the "bump" may be related to a saddle-point present in the landscape, slowing down the thermal relaxation dynamics. Finally, the characteristic late-time scaling, $n^{1/2}$, observed in the single-qubit problem just before the $T_{\rm QSL}$ transition, appears also in the two-qubit problem not only before its T_{QSL} transition but also around the $T_{\rm sb}$ transition.

Last, let us point out that in all our simulations in the single-qubit landscape, LMC always thermalizes around a global optimal protocol without getting trapped in any local minimum. On the contrary, in the two-qubit problem for $L{=}16,32,64$ we sometimes found the LMC dynamics trapped in a local minimum of the landscape for $T{\in}[2.0,3.3]$, approximately. In this case, a Simulated Annealing protocol combined with a post-selection among a



Two-qubit problem. The plots show the dis-FIG. 19. crete derivative of infidelity, dI_n/dn during thermal relaxation, averaged over ten independent LMC runs. The parameter T, different in the four panels, is changed to investigate the effects of CLPTs (cf. $T_{\rm sb} \simeq 1.57, T_{\rm QSL} \simeq 2.95$). Each curve refers to a different Monte Carlo inverse-temperature β while $\sigma{=}10^{-3/2},\,L{=}512$ are fixed. As in the single-qubit system, a simple effective one-dimensional toy model (black-dashed line in panels (a) and (d); cf. (D2)) can approximate the typical scaling observed in data away from the critical values. The change in slope (from $\simeq 1$ to $\simeq 1/2$) observed just before $T_{\rm OSL}$ in the single-qubit case (cf. Fig. 18) is also visible here around $T_{\rm sb}$ (panels (b) and (c)) and just before $T_{\rm QSL}$ (panel (e)). The discrete numerical derivative is computed with the function gradient from Python's package NumPy. We decreased the opacity of each curve to 10% after thermalization occurred.

set of five thermal relaxation runs is enough to guarantee the convergence of LMC to the optimal level set in all of our simulations.

2. Diffusion stage

In order to develop some intuition about the diffusion stage, it is convenient to consider the theoretical limit $\sigma \to 0$ at fixed $\beta \gg \sigma^2$. In this limit, the acceptance probability $P_{\rm acc}$ approaches unity and the dynamics becomes

effectively a free random walk in L dimensions. In practice, we consider a small but finite σ so that $P_{\rm acc} \simeq 1$ only during the very early diffusion stage. As ${\bf s}_n$ moves, $P_{\rm acc}$ suppresses the motion in the directions associated with increasing infidelity. As long as the dynamics involves a neighborhood of the starting point, the motion of ${\bf s}_n$ can be decomposed along the local flat directions (tangent directions) and the local infidelity increasing directions (orthogonal directions): the tangential motion is approximately free whereas the motion along orthogonal directions is suppressed by $P_{\rm acc}$. Hence, LMC becomes effectively a random walk in L dimensions restricted by the infidelity landscape to move along the valley's flat directions. Asymptotically, ${\bf s}_n$ diffuses through the valleys and explores a global portion of the optimal level set.

Using the random walk as a theoretical limiting behavior, we characterize the diffusive motion along the optimal level set by considering the covariance matrix associated with a protocol's fluctuations. More precisely, we sample protocols at different iterations $\mathcal{D}_M = \{\mathbf{s}_{n_1} \dots \mathbf{s}_{n_M}\}$ and compute the covariance-matrix

$$\sigma_{M,ij} = \langle s(t_i)s'(t_j)\rangle_M - \langle s(t_i)\rangle_M \langle s'(t_i)\rangle_M$$
 (D5)

where the average is performed over the set \mathcal{D}_M . As we discussed above, the diffusion stage is expected to have three different time scales, each associated with some properties in the covariance matrix (D5).

- 1. Microscopic time-scale. At early iterations the dynamics can be approximated by a free random walk in L-dimension. In this regime, the growth of covariance matrix eigenvalues λ_i have a diffusive scaling behavior $\lambda_i \sim t$.
- 2. Mesoscopic time-scale. When the motion involves a neighborhood of the starting point the dynamics can be decomposed into a free random walk along the tangent directions and a bounded fluctuating motion in the orthogonal directions. Upon diagonalization of the covariance matrix, we expect the tangent/orthogonal (\parallel/\perp) subspace decomposition $\sigma_n \cong D_{\parallel,n} \oplus D_{\perp}$ where D_{\perp} is a diagonal matrix (approximately) independent from n and $D_{\parallel,n}$ is a diagonal matrix whose eigenvalues exhibits diffusive scaling behavior.
- 3. Macroscopic time-scale. Asymptotically the dynamics involves the whole optimal level set. In this regime, covariance matrix eigenvectors specify the principle axis decomposition (of the Gaussian approximation) of the distribution of optimal protocols while the eigenvalues specify the lengths of each semi-axis.

Global properties of the optimal level set can be extracted by letting LMC run on a macroscopic time scale. LMC works at finite L and β so we eventually need to study how results scale as $L,\beta{\to}\infty$. To this end, we run LMC at fixed L and β and let the covariance matrix eigenvalues stabilize to constant values. In Fig. 20

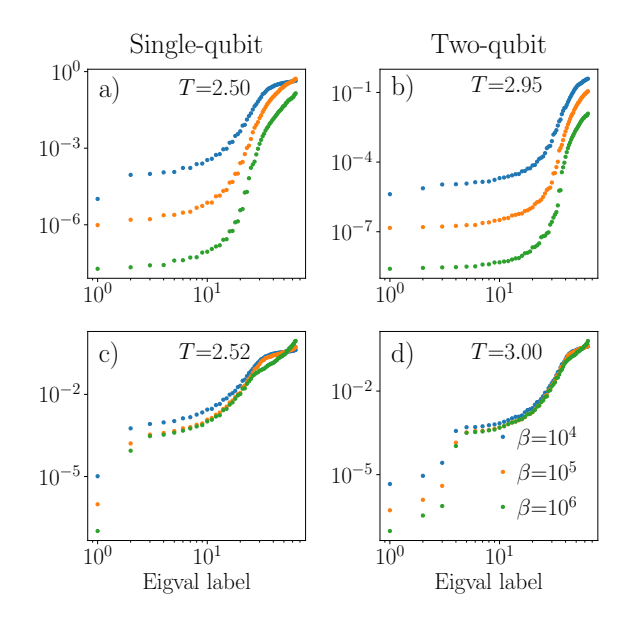


FIG. 20. LMC diffusion stage, covariance-matrix asymptotic eigenvalues for a single LMC run. The eigenvalues capture fluctuations in the protocol dynamics and depend in general on β , the Monte Carlo effective inverse-temperature in Eq. (27). For $T>T_{\rm QSL}$ (panels (c) and (d)), protocol fluctuations along the optimal level set become independent from β ($T_{\rm QSL}\simeq 2.51$, 2.98 in single- and two-qubit problem, respectively). Notice the different number n_+ of β -dependent eigenvalues for $T>T_{\rm QSL}$ in the two problems: the optimal level set expands in L-2 (L-4) directions of the L dimensional protocol space in the single-qubit (two-qubit) problem.

the asymptotic eigenvalues of the covariance-matrix are shown for $\beta=10^4, 10^5, 10^6$. The asymptotic independence of $(L-n_+)>0$ eigenvalues from β for $T>T_{QSL}$ gives a direct numerical confirmation of the presence of an optimal level set of continuously connected optimal protocols. In particular, we see that $n_{+}=2,4$ in the single- and twoqubit case, respectively. We notice that the eigenvalue λ_2 (λ_4) in the single- (two-) qubit case shows a weak dependence with β (cf. Figs. 20c,d): this is compatible with the observed magnitude of the smallest positive eigenvalue of the Hessian, visible in Figs. 5b and 17b. Notice that the presence of n_{+} β -dependent eigenvalues means that along these directions (in the L-dimensional space) the protocol fluctuations still depend on β . Geometrically, this implies that the optimal level set lies in a n_{\perp} -dimensional hyperplane of the L dimensional space.

From the LMC diffusive stage analysis, we estimate the number of LMC iterations $\Delta n_{\rm dec}$ required during diffusion to explore a global portion of the optimal level set. In particular, we define $\Delta n_{\rm dec}$ as the number of iterations required for half of covariance matrix eigenvalues to stabilize to a constant value. Hence, the set of protocols $\mathcal{E}{=}\{\mathbf{s}_{n_1}\dots\mathbf{s}_{n_M}\}$ sampled during the LMC equilibrium sampling stage are separated by $\Delta n_{\rm dec}$ iterations (namely, $n_{i+1}{-}n_i{=}\Delta n_{\rm dec}$). Based on our observa-

tions, we set $\Delta n_{\rm dec} = 2^{12}$ in the single-qubit problem and $\Delta n_{\rm dec} = 2^{14}$ in the single-qubit problem.

3. Equilibrium sampling stage

Eventually, in the LMC equilibrium sampling stage we collect r sets of protocols \mathcal{E}_a , $a=1,2,\ldots,r$ from r independent LMC runs.

LMC allows to estimate the number of connected components in the optimal level set. To this end, we consider the Euclidean distance between two protocols defined by

$$d(s_1, s_2) = \sqrt{\frac{1}{T} \int_0^T dt (s_1(t) - s_2(t))^2}.$$

The distance $d(\mathcal{E}_a, \mathcal{E}_b)$ between sets $\mathcal{E}_a, \mathcal{E}_b$ is defined as the minimum distance found between any two of their protocols:

$$d(\mathcal{E}_a, \mathcal{E}_b) = \min_{\mathbf{s} \in \mathcal{E}_a \ \mathbf{s}' \in \mathcal{E}_b} d(\mathbf{s}, \mathbf{s}'). \tag{D6}$$

The presence of multiple disconnected components can be detected from the (asymptotic) distribution of distance between pairs of LMC runs. If only one connected component is present, we expect to observe a singlepeaked distribution of distances with a peak location that shifts to zero as a larger number of protocols are considered within each set. Otherwise, when multiple disconnected components are present, the distribution of distances is expected to possess multiple peaks while its average value converges to a non-zero value as more protocols are considered. Here, we assume a single LMC run to sample from a single connected component via (approximately) homotopic transformations, for sufficiently large β (cf. Eq. (26)). For the single qubit system, we show how the mean value $\langle d(\mathcal{E}_a, \mathcal{E}_b) \rangle_{a,b}$ scales as the number of protocol samples is increased in Figs. 21. Across the $T_{\rm QSL}$ transition, the minimum distance curves show a similar behavior. For $T>T_{\rm QSL}$, distances are independent from β and decrease with the same slope as in $T < T_{QSL}$, thus suggesting the presence of a single connected component in the optimal level set. The situation in the two-qubit problem is richer and it is discussed in Ref. [62]. In general, we expect different quantum control problems to have different numbers of disconnected components.

On a different note, in Fig. 22 we report the average protocols obtained from LMC equilibrium sampling at different Monte Carlo inverse-temperature β in the single-qubit problem. The average shapes of the optimal protocols collected from LMC match the average optimal protocols obtained with SD (cf. Fig. 15) in the exact infidelity landscape. Notice the protocol fluctuations, represented by the colored area in the plot, affected by β only for $T{=}2.50{<}T_{\rm QSL}$.

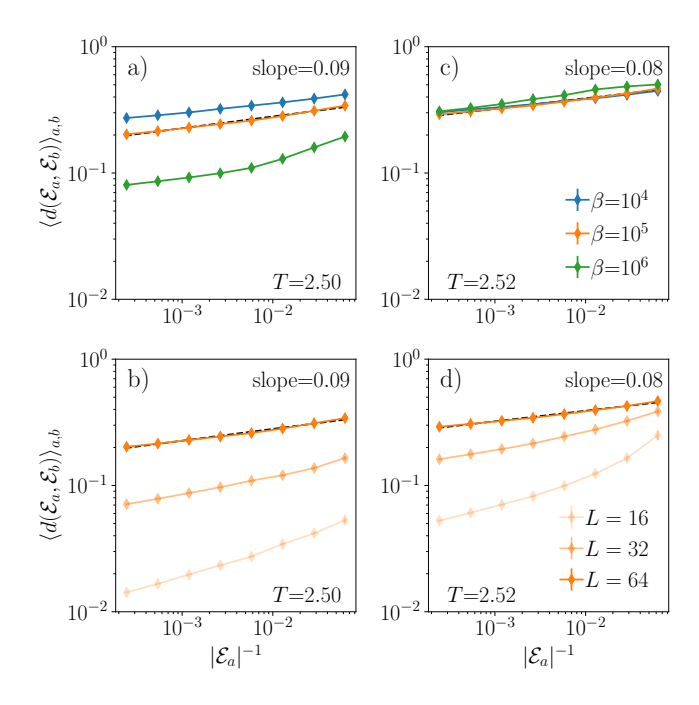


FIG. 21. Single qubit problem, LMC equilibrium sampling stage. The average distance between pairs of LMC runs (out of a total of 20) is shown as a function of $|\mathcal{E}_a|^{-1} = |\mathcal{E}_b|^{-1}$, namely the inverse number of protocols contained in each run. The same slope at the two sides of the $T_{\rm QSL} \simeq 2.51$ transition (compare panels (a) with (c) and (b) with (d)) suggests the presence of a single connected component in the optimal level set for $T \simeq T_{\rm QSL}$.

Appendix E: Optimal level set parametrization

In this section, we test the analytical parametrization proposed in Sec. VI for the optimal level set of the single-qubit problem, for $T \ge T_{\rm QSL}$. The parameterization is based on the quadratic expansion of the infidelity centered around the protocol $s_{\Delta_0(T)}$, defined in Eq. 23 and optimal for $T \le T_{\rm QSL}$. To this end, we explicitly evaluate the infidelity for a continuous family of protocol deformations of the form

$$s_n(x_n) = s_{\Delta_0(T)} + \delta s_n(x_n)$$

$$\delta s_n(x_n) = x_n f^{(n)}$$
(E1)

where $n \in \mathbb{N}$ labels orthogonal eigenfunctions and $x_n \in \mathbb{R}$ controls the magnitude of the deformation; $f^{(n)}(t)$ are the eigenfunctions of the Hessian operator in the infidelity expansion centered in $s_{\Delta_0(T)}$ (cf. Fig. 16).

In the analytical parametrization of the optimal level set truncated at quadratic order, along each direction n associated with a negative Hessian eigenvalue $\lambda_n < 0$, the infidelity eventually crosses the zero-infidelity hyperplane. Since fourth-order terms are neglected, we use these intersection points to estimate the locations of global minima in the exact infidelity landscape.

We test the extent to which this approximation holds

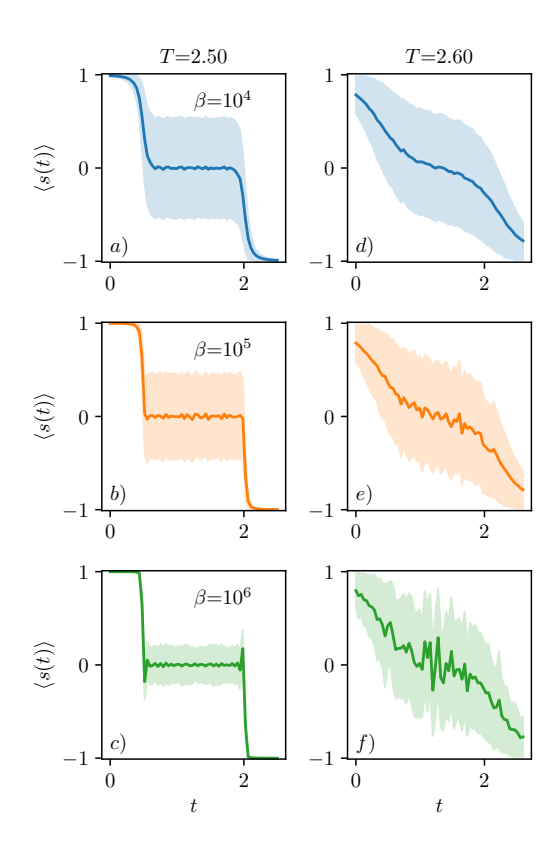


FIG. 22. Single qubit problem. Average protocol resulting from a single LMC run during the equilibrium sampling stage. The colored area shows fluctuations generated by the LMC dynamics in the optimal level set. Notice that the size of fluctuations depends on β only for $T < T_{\rm QSL} \simeq 2.51$ (panels (a), (b) and (c)). It is interesting to compare this result with the average protocols in SD, in Fig. 15.

by computing how the exact infidelity behaves under the deformations in (E1). At fixed x_n , we numerically solve the Schrödinger equation associated with the quantum control problem. In Fig. 23, we show the infidelity as a function of x_n for small and large values of the integer n, for fixed T=2.52. At fixed n, the infidelity curve exhibits in general two minima $I(x_n^{\pm})$, located in the two halfplanes $x_n^- < 0, x_n^+ > 0$. We notice that not every minimum is numerically indistinguishable from zero: for example, for n=3,5 the infidelity at the minima is $\leq 10^{-8}$ whereas for n=7, 9 it reaches a value $\sim 10^{-5}$. In fact, for odd n infidelity evaluated at the minima locations increases as ngrows. That is, for odd n's deformations s_n are not able to reach zero infidelity, except for n=3, 5. On the other hand, for even n, infidelity evaluated at the minima locations remains small ($\lesssim 10^{-8}$) as n grows. Thus, we observe an important limitation of the infidelity quadratic approximation: some predicted optimal protocols in the approximated landscape (at quadratic order) have nonvanishing infidelity in the exact landscape.

As we saw in App. C, parity of n is related to the parity of the $f^{(n)}$ eigenfunction: odd (even) n corre-

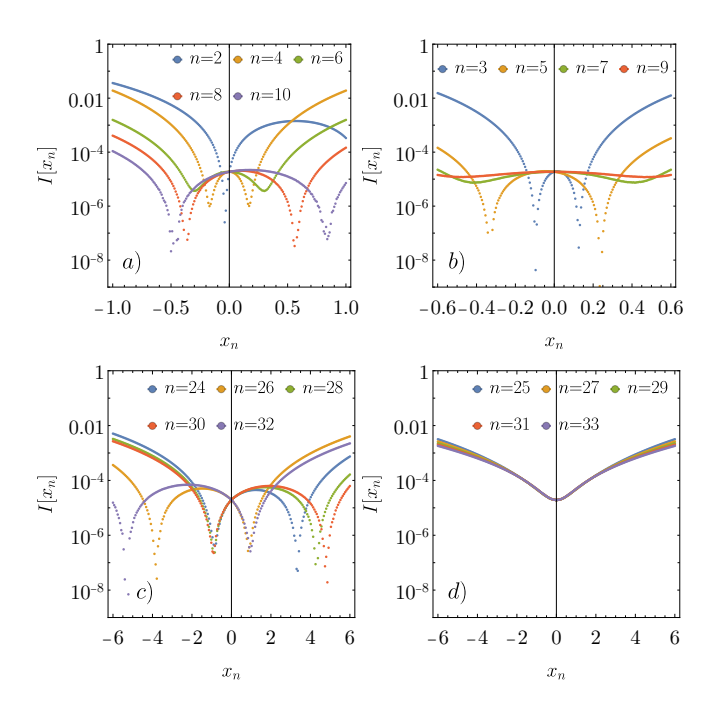


FIG. 23. Single-qubit problem. Infidelity evaluated for different families of protocols $s_n(x_n), n \in \mathbb{N}$ in Eq. (E1), parametrized by the real variable x_n , at fixed T = 2.52. According to the infidelity expansion truncated at quadratic-order, along each direction n > 2 the infidelity should intersect the $I_T[s] = 0$ hyperplane at two values $x_n^+ > 0$ and $x_n^- < 0$. From the plot we observe that this is not always the case in the exact infidelity landscape: for example, for n = 6, 7, 9, $I(x_n^{\pm}) \gtrsim I(0)$ (panel (b)) and for odd $n \gg 1$, $x_n^{\pm} = 0$ (panel (d)). We conclude that, in some cases, the infidelity expansion truncated at quadratic-order may fail to correctly approximate (even at a qualitative level) the exact infidelity landscape; if so, higher-order terms are important for quantitative comparison.

sponds to an even-parity (odd-parity) eigenfunction with respect to the transformation $f(t)\mapsto -f(T-t)$. Hence, for small n, protocols obtained by deforming $s_{\Delta_0}(t)$ along even-parity $f^{(n)}$ are (within numerical precision) optimal and violate the symmetry of the quantum control problem (cf. Sec. II). Therefore, for $T>T_{\rm QSL}$ the quantum control symmetry (respected for $T<T_{\rm QSL}$) is broken in the optimal level set. Interestingly, deformations along eigenfunctions with even-parity (i.e. violating the quantum control problem's symmetry) are exactly the ones strongly affected by higher-order corrections in the infidelity expansion.

Let us also comment on the infidelity curve along the n=2 direction, which is highly non-symmetric with respect to axis $x_2=0$ (see Fig. 23). To understand this, remember that n=2 is associated with one of the two positive eigenvalues visible in the Hessian spectrum (the other being n=1, not shown in the four plots). Hence, the minimum visible in $x_2 \simeq -0.05$ is due to the linear-order term in the infidelity expansion.

As a second comparison between the quadratic approximation and the exact infidelity, in Fig. 24 we compare

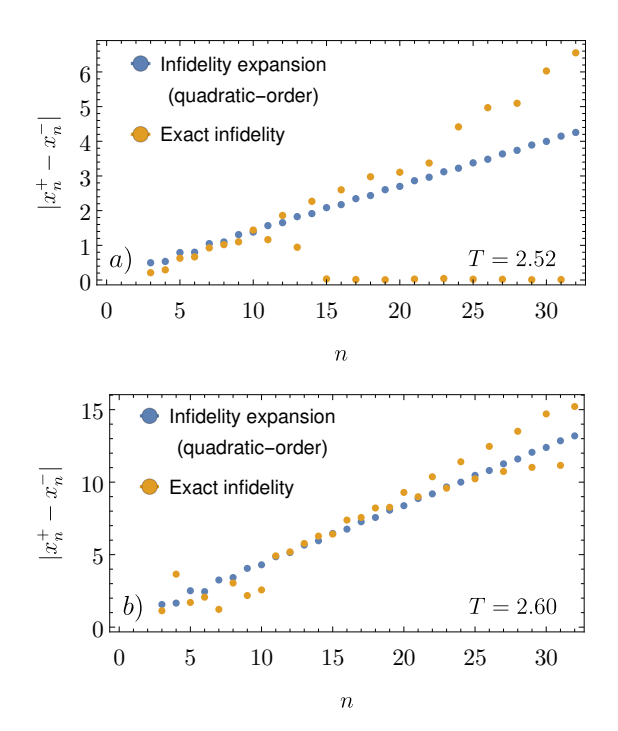


FIG. 24. Single-qubit problem, optimal level set parametrization around $T_{QSL} \simeq 2.51$. The plot shows the separation $|x_n^+ - x_n^-|$ between the two minima x_n^+, x_n^- in the infidelity curve $I[x_n]$ (cf. Eq. 33) along each direction n>2. Due to the Hessian eigenvalues, negative for n>2, minima are in general present pairwise (cf. Fig. 23). Here, we compare the separation estimated by the infidelity expansion (truncated at quadratic-order; orange points) with the separation resulting from the exact landscape (obtained from numerical integration of the Schrödinger equation; blue points). At T=2.52, we observe good quantitative agreement between the exact and approximated infidelity for $n \lesssim 12$; for $n \gtrsim 12$, the agreement is good at a qualitative level for even n only. Comparing T=2.52, 2.60 (in panels (a) and (b), respectively), we observe that for large n there is a better agreement between the exact infidelity and the quadratic-order expansion results. We relate this behavior to the quantum control symmetry $s(t) \leftrightarrow -s(T-t)$, constraining optimal protocols for $T \leq T_{QSL}$.

the location of minima x_n^{\pm} in the exact infidelity landscape with the prediction obtained from the quadraticorder expansion of the infidelity, for T=2.52 and T=2.60. For $n \lesssim 12$, there is a good quantitative agreement between the exact (blue points) and approximated locations (orange points). As n increases, higher-order corrections in the infidelity expansion become important and the two sets of points deviate from each other. In the exact landscape, the location of odd n minima eventually moves to zero, for $n \ge 15$: infidelity does not decrease along these directions and higher-order terms in the infidelity expansion are important for a qualitative comparison with the exact infidelity landscape. Conversely, the quadratic-order expansion of the infidelity underestimates the location of even n minima; in this case, higherorder corrections mildly change the locations of the minima: the quadratic-order expansion and the exact landscape produce the same qualitative result. As a final remark, we notice that, as $T \rightarrow T_{QSL}$, $|x_n^+|, |x_n^-| \rightarrow 0$ for all odd n (corresponding to even-parity eigenfunctions). This is consistent with the quantum control symmetry $f(t) \mapsto -f(T-t)$ respected by the isolated optimal protocol for $T \leq T_{OSL}$. We deduce that the relatively large contribution of higher-order corrections to the optimal level set parametrization is a direct consequence of the symmetry of the quantum control problem we consider.

Appendix F: Steepest-descent method

In this appendix we show that a saddle-point of the complex function $\Omega(z)$ (cf. Eq. (45)) valid for the steepest-descent method can be always found on the imaginary axis, Re(z)=0, inside the interval $\operatorname{Im}(z) \in (-\lambda_{+}^{-1}, -\lambda_{-}^{-1}) = I$. Remember in Sec. VI we named λ_{+}, λ_{-} the positive and negative eigenvalues (respectively) with the largest absolute value among the spectrum $\{\lambda_n\}$.

Let us separate the real and imaginary parts $z=x+iy, x, y\in\mathbb{R}$ and notice that $\operatorname{Im}\Omega(z)$ vanishes identically on the imaginary axis, x=0; the function $\Omega(z)$ restricted to the imaginary axis is the real function

$$\Omega(y) = \kappa \left(-Iy + \frac{1}{2} \sum_{n} \frac{\Delta x_n^2(k_n)}{1 + \lambda_n y} \right).$$
 (F1)

In particular, we obtain the asymptotic behavior

$$\Omega(y) \sim \frac{\kappa}{2} \frac{\Delta x_n^2}{1 + \lambda_- y} \to +\infty \qquad \lambda_- y \to (-1)^+ \qquad (F2)$$

$$\Omega(y) \sim \frac{\kappa}{2} \frac{\Delta x_n^2}{1 + \lambda_+ y} \to +\infty \qquad \lambda_+ y \to (-1)^+, \qquad (F3)$$

$$\Omega(y) \sim \frac{\kappa}{2} \frac{\Delta x_n^2}{1 + \lambda_+ y} \to +\infty \qquad \lambda_+ y \to (-1)^+, \quad \text{(F3)}$$

the other terms in $\Omega(y)$ being subdominant in the limits considered. Since $\Omega(y)$ is continuous for $y \in I$ (all singular points of $\Omega(y)$ lie outside this interval), there exists $y_* \in I$ such that y_* is a stationary-point (minimum) of the real function $\Omega(y)$. As $\Omega(z)$ is holomorphic in a neighborhood of $z_*=iy_*$, z_* is a saddle-point of the complex function $\Omega(z)$.

We can prove that y_* is the unique saddle-point of $\Omega(z)$ restricted to $x=0, y\in I$. To this end, one can explicitly check that $d_y^2\Omega(y)>0$ for $y{\in}I$ which shows that the real function $\Omega(y)$ is convex for $y \in I$.

Finally, from the holomorphicity of $\Omega(z)$ we deduce that $\operatorname{Im} \Omega(z)$ is constant around the point y_* along the tangent direction $z(x)=x+iy_*$ and that $d_x^2\Omega(z_*)<0$ [72]. Therefore, the integration path in Eq. (31) may be deformed to cross the saddle-point $z=iy_*$ in the tangent direction z(x), for which (i) the imaginary part is constant and (ii) the second derivative of the real part is negative. This proves that $z=iy_*$ is a valid point for the steepest-descent method [72].

Appendix G: Computing q(T)

In this appendix we compute the critical scaling of q(T) as $T \rightarrow T_{\mathrm{QSL}}^+$, predicted by the partition function in Eq. (31). We adopt the notation $\partial/\partial k_n \equiv \partial_{k_n} \equiv \partial_n$. From $\langle x_n^2 \rangle - \langle x_n \rangle^2 = \partial_n^2 \log G[k] \big|_{k=0}$ we obtain

$$\langle x_n^2 \rangle - \langle x_n \rangle^2 = \frac{r_0(u_n)}{\kappa L} + \frac{\kappa L}{2} (\partial_n y_*)^2 \sum_m \lambda_m r_0''(u_m) + \kappa L(\partial_n^2 y_*) \left[-I + \frac{1}{2} \sum_m \lambda_m r_0'(u_m) \right]$$
(G1)

where we use the shorthand notation $u_n = \lambda_n y_*$ and $r'_0(x), r''_0(x)$ denote the first and second derivative, respectively, of the function $r_0(x)$ (cf. Eq. (51)). Derivative of the saddle-point location y_* with respect to k_n variables are obtained from the saddle-point condition in Eq. (49) via the implicit function theorem. It is convenient to rewrite the saddle-point condition as

$$I = \frac{1}{2} \sum_{n} \lambda_{n} \Delta x_{n} (k_{n})^{2} X_{n}$$
$$X_{n} = \frac{1 + 2u_{n} + u_{n}^{2}}{(1 + u_{n}^{2})^{2}},$$

where $\Delta x_n(k_n)$ is defined in Eq. (46). Then, we compute the first partial derivatives

$$(\partial_n y_*) = -\frac{G_n(y_*)}{F(y_*)} \tag{G2}$$

where

$$G_n(y_*) = \sum_m X_m \lambda_m \partial_n \Delta x_m(0)$$
$$F(y_*) = \sum_m \lambda_m \Delta x_m(0) \frac{(\partial_n X_m)}{(\partial_n y_*)}$$

and

$$(\partial_n \Delta x_m)(k_m) = 2\left(-\frac{\Delta x_n(k_n)}{\kappa L}\right) \delta_{nm}$$

$$\frac{(\partial_n X_m)}{(\partial_n y_*)} = \lambda_m (2r_1(u_n) - 4r_2(u_n))$$

$$r_1(x) = 1 + x$$

$$r_2(x) = \frac{x}{(1+x^2)^3}.$$

Similarly, for the second partial derivatives we obtain

$$(\partial_n^2 y_*) = -\frac{(\partial_n y_*)^2 A(y_*) + (\partial_n y_*) B_n(y_*) + C_n(y_*)}{D(y_*)}$$
(G3)

where

$$A(y_*) = \sum_{m} \lambda_m \Delta x_m(0) \frac{(\partial_n^2 X_m^{(1)})}{(\partial_n y_*)^2}$$

$$B_n(y_*) = 2 \sum_{m} \lambda_m \partial_n \Delta x_m(0) \frac{(\partial_n X_m)}{(\partial_n y_*)}$$

$$C_n(y_*) = \sum_{m} \lambda_m \partial_n^2 \Delta x_m(0) X_m$$

$$D(y_*) = \sum_{m} \lambda_m \Delta x_m(0) \frac{(\partial_n^2 X_m^{(2)})}{(\partial_n^2 y_*)}$$

and

$$(\partial_n^2 \Delta x_m)(k_m) = \frac{2}{(\kappa L)^2} \delta_{nm}$$

$$\frac{(\partial_n^2 X_m^{(1)})}{(\partial_n y_*)^2} = \lambda_m^2 (2 - 4r_3(u_n) + 24r_4(u_n))$$

$$\frac{(\partial_n^2 X_m^{(2)})}{(\partial_n^2 y_*)} = 2\lambda_m (r_1(u_n) - 2r_2(u_n))$$

$$r_3(x) = \frac{1}{(1+x^2)^3}$$

$$r_4(x) = \frac{x^2}{(1+x^2)^4}.$$

In the limit $n\to\infty$ and for T fixed, the dominant term in the right-hand side of Eq. (G1) is only the first one, provided that $u_n\to 0$. To see this, notice that $r_0(u_n)\to 1$ as $n\to\infty$ whereas the second and third terms depend respectively on $(\partial_n y_*)^2 \sim (\lambda_n \Delta x_n(0)/L)^2$ and $(\partial_n^2 y_*) \sim \lambda_n/L^2$, and they vanish in the same limit; also, recall that $\sum_n \Delta x_n(0)^2 < \infty$ by construction.

and $(\partial_n^2 y_*) \sim \lambda_n/L^2$, and they vanish in the same limit; also, recall that $\sum_n \Delta x_n(0)^2 < \infty$ by construction. We interpret this result in the following way. The quantity $\langle x_n^2 \rangle - \langle x_n \rangle^2$ is obtained via $\partial_n^2 \log G[k] \big|_{k=0}$ and $\log G[k]$ depends on k_n explicitly through $\Delta x_n(k_n)$ and implicitly through y_* . From our calculation, we deduce that the change in the saddle-point location y_* due to a change of k_n , has a subdominant effect on $\langle x_n^2 \rangle - \langle x_n \rangle^2$, as $n \to \infty$, with respect to the change in $\Delta x_n(k_n)$.

Finally, let us comment on the assumption $u_n = \lambda_n y_* \to 0$, as $n \to \infty$, for T fixed. In our case, this condition is satisfied since (i) $-\lambda_+^{-1} < y_* < -\lambda_-^{-1}$ (cf. App. F), (ii) $\lambda_n \to 0$ as $n \to \infty$ (cf. footnote of Eq. (21)).

Appendix H: Computing $q_{BB}(T)$

In this appendix we compute the critical scaling of $q_{\rm BB}(T)$, as $T \rightarrow T_{\rm QSL}^+$, predicted by the partition function in Eq. (52). From Eq. (55) we have

$$q_{\mathrm{BB}}(T) = q_{\mathrm{BB},0}(T) - \sum_{n} (2\langle x_n \rangle + \langle x_n \rangle^2)$$
 (H1)

where $q_{\mathrm{BB},0}(T)=1-\sum_n x_{0n}^2$ represents the contribution given by the protocol $s_{\Delta_0(T)}$, optimal for $T=T_{\mathrm{QSL}}$. We

see that the critical scaling only depends on the first moments $\langle x_n \rangle$. In particular, from $\langle x_n \rangle = \partial_n \log G_{\rm BB}[k] \big|_{k=0}$ (cf. Eq. (57)) we obtain

$$\langle x_n \rangle = -x_{1n} - \Delta x_n(0)r_0(u_n) + N(\partial_n y_*) \left(-I + \frac{1}{2} \sum_m \lambda_m \Delta x_m^2(0)r_0'(u_m) \right)$$
(H2)

where $(\partial_n y_*)$ is given by Eq. (G2). We use the shorthand notation $u_n = \lambda_n y_*$ and $r'_0(x)$ denote the first derivative of the function $r_0(x)$ (cf. Eq. (51)).

In order to extract the critical scaling of $q_{\rm BB}(T)$ for $T \rightarrow T_{\rm QSL}^+$, we study how the quantities appearing in Eq. (H2) scales as a function of $\Delta T = T - T_{\rm QSL}$. In general, assuming analyticity in $\Delta T = 0$ we expect

$$x_{0n} \sim 1$$
 $I \sim \Delta T^2$ $b_{n \leq n_+} \sim \Delta T$ $b_{n > n_+} \sim \Delta T^2$ $\lambda_{n \leq n_+} \sim 1$ $\lambda_{n > n_+} \sim \Delta T$

so that

$$x_{1n} = \frac{b_n}{\lambda_n} \sim \Delta T.$$

Here, for the sake of generality, we assumed n_+ non-vanishing eigenvalues at the quantum speed limit CLPT. In Sec. VIC we explicitly consider the single-qubit case where n_+ =2 and the scaling behaviors in ΔT can be expressly verified.

From $\lambda_- \sim \Delta T$ as $\Delta T \rightarrow 0$ we have $y_* \sim \Delta T^{-1}$ in the same limit. Moreover, from the constraint $y_* < \lambda_-$ (cf. Sec. F) we have also

$$u_n = y_* \lambda_n \begin{cases} \sim \Delta T^{-1} & n \le n_+ \\ \lesssim 1 & n > n_+ \end{cases}$$

and, as a consequence,

$$r_0(u_n) \sim \begin{cases} \Delta T & n \le n_+ \\ 1 & n > n_+ \end{cases}, \quad r'_0(u_n) \sim \begin{cases} \Delta T^2 & n \le n_+ \\ 1 & n > n_+ \end{cases}.$$

Finally, substituting these results into (H2) we obtain

$$\langle x_{n \le n_+} \rangle \sim -x_{1n} - \Delta x_n(0) r_0(u_n) +$$

$$(N\partial_n y_*) \frac{1}{2} \sum_{m > n_+} \lambda_m \Delta x_m^2(0) r_0'(u_m)$$

$$\langle x_{n > n_+} \rangle \sim -x_{0n}$$

where $(N\partial_n y_*)\sim \lambda_n$, and eventually

$$\langle x_n \rangle \sim \begin{cases} \Delta T & n \le n_+ \\ \text{const} & n > n_+ \end{cases}$$
 (H3)

Notice that $\langle x_n \rangle$ does not vanish as $\Delta T \rightarrow 0$ for $n > n_+$. On the other hand, for $T \rightarrow T_{\mathrm{QSL}}^-$, the center of the infidelity exansion is assumed to be an isolated optimal protocol, so that $\langle x_n \rangle = 0$, in this limit. Hence, according to the partition function in Eq. (52) with infidelity expansion truncated at quadratic-order, $\langle x_n \rangle$ has a jump-discontinuity at $T = T_{\mathrm{QSL}}$.

From $\langle x_n \rangle$ we obtain the critical scaling

$$q_{\rm BB}(T) - q_{\rm BB,0}(T) \sim {\rm const} + \Delta T$$

where the constant term is given by

$$\sum_{n>n_{\perp}} \left(2 \left\langle x_n \right\rangle + \left\langle x_n \right\rangle^2\right) = \text{const}$$

whereas the linear term in ΔT by

$$\sum_{n \le n_+} (2 \langle x_n \rangle + \langle x_n \rangle^2) \sim \Delta T.$$

As discussed in Sec. VIC, the constant term is a consequence of the quadratic-order truncation in the infidelity expansion and vanishes (together with the jump-discontinuity in $\langle x_n \rangle$ at $T=T_{\rm QSL}$) once higher-order (in particular quartic-order) terms are considered.

^[1] D. D'Alessandro, Introduction to Quantum Control and Dynamics (2nd ed.) (Chapman and Hall/CRC, 2021).

^[2] H. A. Rabitz, M. M. Hsieh, and C. M. Rosenthal, Science 303, 1998 (2004).

^[3] U. Boscain, M. Sigalotti, and D. Sugny, PRX Quantum 2, 030203 (2021).

^[4] C. P. Koch et al., EPJ Quantum Technology 9, 19 (2022).

^[5] S. J. Glaser et al., The European Physical Journal D 69, 1 (2015).

^[6] A. Acín et al., New Journal of Physics 20, 080201 (2018).

^[7] A. Ungar, P. Cappellaro, A. Cooper, and W. K. C. Sun, PRX Quantum 5, 010321 (2024).

^[8] Z. Li, X. Ye, X. Kong, T. Xie, Z. Yang, P. Zhao, Y. Wang,

F. Shi, and J. Du, Phys. Rev. Appl. 21, 054011 (2024).

^[9] G. Wang, Y.-X. Liu, J. M. Schloss, S. T. Alsid, D. A. Braje, and P. Cappellaro, Phys. Rev. X 12, 021061 (2022).

^[10] P. Rembold, N. Oshnik, M. M. Müller, S. Montangero, T. Calarco, and E. Neu, AVS Quantum Science 2, 024701 (2020).

^[11] C. L. Degen, F. Reinhard, and P. Cappellaro, Rev. Mod. Phys. 89, 035002 (2017).

^[12] J. E. Gough and V. P. Belavkin, Quantum information processing 12, 1397 (2013).

^[13] J. M. Gertler, B. Baker, J. Li, S. Shirol, J. Koch, and C. Wang, Nature 590, 243 (2021).

- [14] S. Zhou and L. Jiang, Phys. Rev. Res. 2, 013235 (2020).
- [15] K. Khodjasteh and L. Viola, Phys. Rev. A 80, 032314 (2009).
- [16] C. Ahn, A. C. Doherty, and A. J. Landahl, Phys. Rev. A 65, 042301 (2002).
- [17] C. Altafini and F. Ticozzi, IEEE Transactions on Automatic Control 57, 1898 (2012).
- [18] C. Brif, R. Chakrabarti, and H. Rabitz, New Journal of Physics 12, 075008 (2010).
- [19] N. Khaneja, T. Reiss, C. Kehlet, T. Schulte-Herbrüggen, and S. J. Glaser, Journal of Magnetic Resonance 172, 296 (2005).
- [20] D. M. Reich, M. Ndong, and C. P. Koch, The Journal of Chemical Physics 136, 104103 (2012).
- [21] T. Caneva, T. Calarco, and S. Montangero, Phys. Rev. A 84, 022326 (2011).
- [22] P. Doria, T. Calarco, and S. Montangero, Phys. Rev. Lett. 106, 190501 (2011).
- [23] T. Mahesh, P. Batra, and M. H. Ram, Journal of the Indian Institute of Science 103, 591 (2023).
- [24] S. Machnes, U. Sander, S. J. Glaser, P. de Fouquières, A. Gruslys, S. Schirmer, and T. Schulte-Herbrüggen, Phys. Rev. A 84, 022305 (2011).
- [25] Y. Zhang and J. Dziarmaga, (2024), arXiv:2401.09158 [quant-ph].
- [26] Y. Yang, Z. Zhang, X. Xu, B.-N. Lu, and Y. Li, Phys. Rev. A 108, 032403 (2023).
- [27] R. Chakrabarti and H. Rabitz, International Reviews in Physical Chemistry 26, 671–735 (2007).
- [28] X. Ge, R.-B. Wu, and H. Rabitz, Annual Reviews in Control 54, 314 (2022).
- [29] X. Ge, R. Wu, and H. Rabitz, Complex System Modeling and Simulation 1, 77 (2021).
- [30] A. G. R. Day, M. Bukov, P. Weinberg, P. Mehta, and D. Sels, Phys. Rev. Lett. 122, 020601 (2019).
- [31] S. van Frank, M. Bonneau, J. Schmiedmayer, S. Hild, C. Gross, M. Cheneau, I. Bloch, T. Pichler, A. Negretti, T. Calarco, et al., Scientific reports 6, 34187 (2016).
- [32] M. G. Bason, M. Viteau, N. Malossi, P. Huillery, E. Arimondo, D. Ciampini, R. Fazio, V. Giovannetti, R. Mannella, and O. Morsch, Nature Physics 8, 147 (2012).
- [33] M. Dalgaard, F. Motzoi, and J. Sherson, Phys. Rev. A 105, 012402 (2022).
- [34] G. Matos, S. Johri, and Z. Papić, PRX Quantum 2, 010309 (2021).
- [35] T. Caneva, A. Silva, R. Fazio, S. Lloyd, T. Calarco, and S. Montangero, Phys. Rev. A 89, 042322 (2014).
- [36] S. Hernández-Gómez et al., (2023), arXiv:2112.14998 [quant-ph].
- [37] A. P. Solon and J. M. Horowitz, Phys. Rev. Lett. 120, 180605 (2018).
- [38] G. Folena, A. Manacorda, and F. Zamponi, Physica A: Statistical Mechanics and its Applications 631, 128152 (2023).
- [39] H. Nishimori, Statistical Physics of Spin Glasses and Information Processing: An Introduction (Oxford University Press, 2001).
- [40] M. Bukov, A. G. R. Day, D. Sels, P. Weinberg, A. Polkovnikov, and P. Mehta, Phys. Rev. X 8, 031086 (2018).
- [41] M. Bukov, A. G. R. Day, P. Weinberg, A. Polkovnikov, P. Mehta, and D. Sels, Phys. Rev. A 97, 052114 (2018).
- [42] D. Hu, P. Ronhovde, and Z. Nussinov, Phys. Rev. E 86, 066106 (2012).

- [43] S. C. Morampudi, B. Hsu, S. L. Sondhi, R. Moessner, and C. R. Laumann, Phys. Rev. A 96, 042303 (2017).
- [44] M. Mézard, M. Palassini, and O. Rivoire, Phys. Rev. Lett. 95, 200202 (2005).
- [45] R. Monasson and R. Zecchina, Phys. Rev. E 56, 1357 (1997).
- [46] M. Mézard, G. Parisi, and R. Zecchina, Science 297, 812 (2002).
- [47] M. Mezard, G. Parisi, and M. Virasoro, Spin Glass Theory and Beyond (WORLD SCIENTIFIC, 1986).
- [48] M. Bukov, D. Sels, and A. Polkovnikov, Phys. Rev. X 9, 011034 (2019).
- [49] H. Schättler and U. Ledzewicz, Geometric Optimal Control (Springer New York, NY, 2012).
- [50] L. T. Brady, C. L. Baldwin, A. Bapat, Y. Kharkov, and A. V. Gorshkov, Phys. Rev. Lett. 126, 070505 (2021).
- [51] G. C. Hegerfeldt, Phys. Rev. Lett. 111, 260501 (2013).
- [52] M. Bukov, L. D'Alessio, and A. Polkovnikov, Advances in Physics 64, 139 (2015).
- [53] W. Magnus, Communications on Pure and Applied Mathematics 7, 649 (1954).
- [54] S. Blanes, F. Casas, J. Oteo, and J. Ros, Physics Reports 470, 151 (2009).
- [55] S. Blanes, F. Casas, J. A. Oteo, and J. Ros, European Journal of Physics 31, 907 (2010).
- [56] Here, we use the shorthand notation $s_t = s(t)$ and $m'_t = m'_*(t)$.
- [57] For a detailed discussion of the computational costs associated with the Magnus approximation of the evolution operator see [54, 55].
- [58] Observe that, by construction, $J_{tt'}$ is the real and symmetric kernel of a Hilbert-Schmidt integral operator; i.e. it satisfies the following properties: (i) $J_{tt'} \in \mathbb{R}$, (ii) $J_{tt'} = J_{t't}$, (iii) $\int_0^T \mathrm{d}^2 t \, |J_{tt'}|^2 < \infty$. Then, if we search for eigenfunctions $\{f_t^{(n)}\}$ in the functional space $L^2([0,T])$, the associated eigenvalues $\{\lambda_n\}$ exist well-defined, are real, have a finite range and an accumulation point at zero. In this case, we may estimate the eigenvalues $\{\lambda_n\}$ by first discretizing the time domain [0,T] in L steps and, subsequently, consider the limit $L \to \infty$.
- [59] The choice of $s(t)\equiv 0$ as a starting protocol is arbitrary but convenient. For other choices $s\neq 0$, finding the optimal protocol requires more attention.
- [60] This argument should not be considered as rigorous. In our case, it is sufficient to guess the structure of the optimal protocol for $T>T_c$. In general, a more quantitative analysis is required to obtain the optimal protocol structure past a given CLPT (for example, [36]).
- [61] G. O. Roberts and J. S. Rosenthal, Journal of the Royal Statistical Society Series B: Statistical Methodology 60, 255 (2002).
- [62] N. Beato, P. Patil, and M. Bukov, in preparation (2024).
- [63] Notice that here β is independent of the parameter appearing in the LMC algorithm in Sec. V.
- [64] We neglect overall prefactors in the partition and the generating functionals as they do not contribute to expectation values.
- [65] S. Donaldson, *Riemann Surfaces* (Oxford University Press, 2011).
- [66] We neglect contributions from the integrand's denominator as they do not contribute in the $L\rightarrow\infty$ limit to the expectation values $\langle x_n \rangle$, $\langle x_n^2 \rangle$.
- [67] C. Tsallis, Journal of statistical physics **52**, 479 (1988).

- [68] E. Farhi, J. Goldstone, and S. Gutmann, (2014), arXiv:1411.4028 [quant-ph].
- [69] S. H. Sack, R. A. Medina, R. Kueng, and M. Serbyn, Phys. Rev. A 107, 062404 (2023).
- [70] R. A. Medina and M. Serbyn, (2024), arXiv:2405.10125 [quant-ph].
- [71] A. Lerose, M. Sonner, and D. A. Abanin, Phys. Rev. X 11, 021040 (2021).
- [72] J. D. Murray, Asymptotic analysis, Vol. 48 (Springer Science & Business Media, 2012).